Opportunistic RIS-Aided WiFi Imaging in Smart ElectroMagnetic Environments

BY

CARLO TORTORIELLO
B.S., Politecnico di Torino, Turin, Italy, 2022

THESIS

Submitted as partial fulfillment of the requirements
for the degree of Master of Science in Electrical and Computer Engineering
in the Graduate College of the
University of Illinois Chicago, 2024

Chicago, Illinois

Defense Committee:

Danilo Erricolo, Chair and Advisor
Giacomo Oliveri, Università degli Studi di Trento
Vecchi Giuseppe, Politecnico di Torino

A mia Mamma.

A chi c'è sempre stato.

A nonna Emilia.

ACKNOWLEDGMENTS

Words could never express my heartfelt gratitude to Professor Danilo Erricolo for his unwavering academic support and invaluable guidance on a personal level. His remarkable initiative and professionalism have had a profound impact on my journey. Professor Erricolo's mentorship has been truly inspiring. He helped me discover my passion for Electromagnetics within the field of Electrical Engineering.

I am deeply grateful to the entire committee for their dedication and commitment to my work. In particular, I would like to extend a special thanks to Professor Giacomo Oliveri and to the ELEDIA research group for the unique support and assistance to this work, leading to a paper submission. I would also like to thank the Electrical and Computer Engineering(ECE) Department at UIC and the Dipartimento di Elettronica e Telecomunicazioni (DET) at Politecnico di Torino for their bureaucratic support and financial assistance throughout my degree program.

A note of gratitude and profound respect goes to Tommaso Balercia, Principal Engineer at NVIDIA and personal mentor during my internship as a Software Engineer in the summer of 2024. I acknowledge and respect him as much as an academic advisor. At the same time, I am deeply grateful for the opportunities and lessons he provided me at a human level.

CT

ACKNOWLEDGMENTS (continued)

Contribution of Authors

Chapters 2 expands on the creation of the Channel State Information matrix and the overall model adopted and described in the early work published at the National Radio Science Meeting 2024, held in Boulder, Colorado (1).

Chapters 4 and 5 delve deeper into a significant portion of the research presented in the aforementioned conference paper, which was supervised by professors Danilo Erricolo and Giacomo Oliveri, who also contributed to the editing of the manuscript.

Chapters 7 and 6 investigate and explain the relevant outcomes of the work leveraging the metrics and the approach already adopted throughout the early part of the research.

TABLE OF CONTENTS

TABLE OF CONTENTS (continued)

CHAPTER **PAGE**

LIST OF TABLES

LIST OF FIGURES

LIST OF FIGURES (continued)

FIGURE **PAGE**

FIGURE **PAGE**

LIST OF ABBREVIATIONS

ART	Algebraic Reconstruction Technique
LOS	Line-Of-Sight
RIS	Reflective Intelligent Surfaces
ROI	Region Of Interest
RX	Receiving Antenna
SAR	Synthetic Aperture Data
SEME	Smart ElectroMagnetic Environment
TSVD	Truncated Singular Values Decomposition
TV	Total Variation
TX	Transmitting Antenna
UIC	University of Illinois at Chicago
OFDM	Orthogonal Frequency Division Multiplexing
LIDAR	Laser Imaging, Detection, and Ranging
MIMO	Multiple Input Multiple Output
CG	Conjugate Gradient

SUMMARY

Imaging and object detection at Radio Frequency refers to a set of techniques that aims to reconstruct extended or point-shaped objects from a set of complex measurements performed at radio frequency. The system to be investigated is based on the use of Reflective Intelligent Surfaces(RIS), which actively interacts with the environment to improve RF imaging resolution. Each panel is made of many programmable cells. The RIS exhibits the breaking-through capability of coherently combining the electric field directly incident on a target with the reflected one by introducing a proper phase shift. The target is imaged by reconstructing its reflectivity profile based on the projections measured. The region of interest (ROI), which contains the albedo, is divided into pixels, and the system collects as many measurements as the number of discrete elements.

The effortless integration of RIS-aided systems into current WiFi-based electromagnetic environments makes this research worthwhile. The ubiquity and flexibility of the WiFi protocol make the integration of these systems much more accessible and far-reaching.

Unlike radar or Synthetic Aperture Radar (SAR), which generally employ wide-band pulses, RF imaging at the WiFi level uses an 802.11 protocol to leverage spectrum partitioning. The total available bandwidth is arranged into 40-MHz channels to illuminate the scene. The target reconstruction relies on both bandwidth and measurement diversity given by spatial and frequency proper choices.

According to simple WiFi network protocol, two Access Points(APs) regulate the centralized communication over the 2.4GHz or 5GHz frequency domains. The AP, acting as the receiver, collects scattered electromagnetic field samples, which are processed to obtain images of the complex reflectivity profile of the surface under investigation.

The use of RIS in image reconstruction at mmWave allows the estimate of the location and shape of the target, carrying out the main benefit of simplifying the hardware for the system.

In this context, further investigation into the advancements in the *inversion* process, which transforms the multitude of measurements into a reconstructed image, is highly valuable. Simulated results are presented to assess the performance of various inversion algorithms, considering not only computational efficiency and reconstruction capabilities but also noise rejection and robustness of the results.

CHAPTER 1

INTRODUCTION

Imaging refers to the reconstruction of the reflectivity profile of an object or a scene using a set of techniques based on electromagnetic wave measurements. There are numerous areas that can benefit from such a powerful and effective resource, including security, military, and medical fields. Imaging is used in these different disciplines to indicate the visual reconstruction of a physical quantity considered of interest[2; 3; 4].

For example, most US airports use advanced tomographic scanners at checkpoints to improve metallic object detection and security checks. Bio-imaging is the medical attachment of this electromagnetism branch and refers to performing accurate, non-invasive human-body scanning to enhance diagnostic capabilities. It is often desirable to know what is inside an object without physically accessing it. The imaging technique choice follows a series of practical considerations that consider specific fields of application, safety, and security patterns.

First, the availability of a medium to carry the signals sets a starting condition: RF imaging, relying on medium for wave propagation, always allows the use of Electromagnetic(EM) waves working at a WiFi level. Second, the choice of wavelength for systems is critical. The energy of an electromagnetic field depends on both the amplitude and frequency of the propagating wave. Therefore, each application imposes specific constraints on the power and frequency of the wave. For instance, high-frequency waves are potentially dangerous for the human body, which is a typical application-specific constraint in the medical field. The proper frequency choice also affects the resolution capabilities of the system. It is well-known that optical frequency techniques are ideally more suited for imaging purposes. First of all, there are many effective ray-based techniques(Geometric Optics, GDT, Uniform Theory of Diffraction) for the study of High-frequency electromagnetic fields to describe complex propagation phenomena. Second, optical techniques can achieve a far better resolution than RF-based ones thanks to high-quality lenses and, more importantly, lower wavelengths spanning from nm to μm scale.

A famous example is LiDAR technology, which consists of a radar that sends out and receives light pulses. The optical frequency narrows the beam(i.e., increases resolutions), and its combination with the measured time-of-flight allows for accurate target imaging or detection.

However, optical imagers feature two main drawbacks. First, the main downside is their poor tolerance in low signal-to-noise ratio. The imaging resolution in adverse weather or environmental conditions severely suffers from obstructed object configurations (Non-Line-Of-Sight). Second, the computational effort generally increases with complexity

At the same time, RF imaging offers several advantages for low-cost and low-SNR imaging capabilities. One key benefit is its ability to "see" through obstacles and operate in conditions where optical systems struggle due to limited penetration capabilities[5; 6]. This includes scenarios like darkness, obstructions like paper or clothing, and low signal-to-noise ratio environments. Millimeter-wave imaging through opaque objects also presents broad potential. It finds applications in areas ranging from security and hazardous environments to quality control of packaged goods. Another significant advantage is the improved capabilities of antenna arrays. When multiple MIMO antennas are arranged in a closely packed array structure, the radiated beam can be precisely directed during transmission and effectively detected during reception. This setup enables robust and highly directive RF communication. The number of radiating elements, their mutual distances, and design choices determine the array pattern and improve the directivity, providing finer spatial coverage. The widespread use of WiFi technology offers a cost-effective means to integrate imaging and sensing at RF. The ubiquity of these technologies makes them a powerful tool for effective and manageable integration of imaging techniques. Most off-the-shelf WiFi devices today are equipped with MIMO antennas, enhancing angular detection and "pencil" beam-forming capabilities[7]. Despite these advancements, the appeal of lightweight hardware for WiFi-based systems remains strong and continues to play a crucial role in the design of many systems. The WiFi technology is based on IEEE 802.11 communication protocol and adopts an Orthogonal Frequency-Division Multiplexing spectrum partitioning. This technique operates on a set of narrow-band channels typically centered around either 2.4 GHz or 5 GHz and provides a robust and scalable resource.

In conventional single-channel modulation schemes, data bits are typically transmitted serially. In OFDM, multiple bits can be transmitted serially but simultaneously in separate sub-channels, improving noise and jamming immunity. This can be graphically seen as outlined in Figure 1. As a result, each "sub-stream" can operate at a lower data rate compared to a single stream with a similar bandwidth. This characteristic enhances the resilience of the system to interference and enables more effective utilization of data bandwidth.

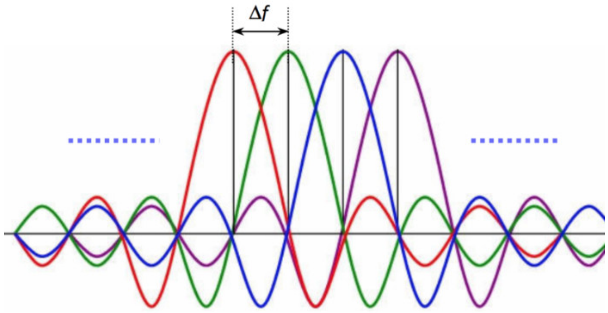

Figure 1: OFDM spectrum partitioning illustrative example

The OFDM technique specifically addresses multi-path and fading effects. The early WiFi devices had poor hardware resources that strictly limited the development of such effective communication protocols. Nowadays, implementing a scalable technology that considers both economics and sustainability is still a desirable feature.

In this regard, Smart ElectroMagnetic Environments have recently grown exponentially. SEMEs are meant to enhance wireless communication capabilities regarding spectral and power efficiency while reducing hardware complexity. Passive Electromagnetic skins (EMS), intelligent Metasurfaces, and meta-materials research are just a small part of the whole set of resources to be integrated into such environments. Academic research paid much attention to this page and has heavily moved efforts toward Reflective Intelligent Surfaces(RIS) to improve RF data transmission for real systems applications.

RIS are man-made surfaces deployed in smart environments to boost the power measured at the receiver side by constructively or destructively superimposing the field coming from the transmitter. This system can achieve fine-grained passive beam-forming for directional signal enhancement, breaking through the fundamental limitation of the single antenna RF-imaging performance. The basic hardware exhibits poor beam-forming capabilities due to lower directivity. RIS can constructively combine the electric field directly impinging on a pointed pixel of the target with the reflected components to compensate for this lack of fine-grained scanning capabilities. The ideal working principle would, at the same time, increase directivity toward a specific pixel of the object while suppressing the undesired components related to other pixels. These tools provide an additional degree of freedom to break through the fundamental limitation of RF-based imaging performance and pave the way to realize a smart and programmable imaging infrastructure.

However, the relatively lower RF frequencies usually place three main holds on imaging problems. First, the system features a higher wavelength due to the RF wave nature. On the one hand, the higher wavelength directly impacts the achievable spatial resolution; on the other hand, the antenna equivalent aperture would be heavily reduced. In antenna theory, the effective aperture of an antenna indicates the practical amount of physical area interacting with the incoming electromagnetic waves. At lower frequencies, this *effective aperture* becomes a smaller percentage of the physical aperture, the physical antenna size along the field propagation. The effective aperture of the antenna inversely depends on the frequency

$$A \propto \frac{1}{f^2} \tag{1.1}$$

The lower the frequency, the lower the effective aperture, and the poorer the scanning resolution of our RF imaging system. Similar to a camera, the larger the aperture, the more energy is collected. Second, the receiver measures a combination of the reflected and scattered waves from the target and its complex environment, potentially leading to multi-path effects and inter-element strong correlation. The research on RIS-aided WiFi imaging can improve the power and spectral efficiency of the whole system, increasing the reconstruction quality while keeping hardware cost and noise injection at a minimum. As typically happens in the engineering world, the simple hardware layer comes at the cost of greater complexity from the numerical and software sides. However, regardless of the specific WiFi system, the imaging process usually follows three fundamental steps.

First, it is important to set the quantity that the model should retrieve: What is a physical quantity of interest? Considering prior knowledge of the application, the expected response, and the system size, this initial question can be addressed to start the reconstruction process.

Second question: *How do we relate the measurements with the unknown? Can we use a linear model?* The imaging systems are mainly divided into model-based and data-based. Data-based techniques are increasingly calling for attention in the world of AI and Neural Networks, which are used to reconstruct images with supervised learning techniques. However, this work focuses on electromagnetism principles to create a consistent model to link the unknown of interest to the measurable quantity. The model represents a simplified version of reality, built on assumptions and considerations made during its derivation. In deriving the forward model, this consideration can be expressed through various mathematical approximations to more effectively address practical issues. The cutting-edge feature of this work is given by the model definition that considers RIS surfaces to evaluate how different algorithms applied to the model-based system can perform.

Third question: *How can we retrieve that informative quantity from our set of collected data?* The answer to the last question involves the data processing resulting from this model. This general area of mathematical physics is called *inversion* of the problem. The problem just described is mathematically *badly-conditioned* and intrinsically *ill-posed*. Few unexpected variations to the input can heavily destabilize the search for a valid solution. Drawing on the accurate description in [8], this work aims to evaluate the efficacy of direct and indirect methods operating on the newly introduced forward model for RF imaging based on Reflective Intelligent Surfaces. Before delving into this, a complete description of RF imaging is given, followed by the evaluation of iterative techniques adopted to overcome some of the limitations given by direct methods.

The work presented here builds upon an early work published in the National Radio Science Meeting 2024 in Boulder(Colorado), which has already been discussed[1]. The outline of the work is arranged in a modular way.

Chapter 1 will introduce the RIS, outlining advantages, modern applications in academic research, and limitations. A general introduction to the problem will also be provided to fix intrinsic challenges related to the topic. Chapter 2 will describe in detail all assumptions and reasons for the choices leading to the linear forward model. Chapter 3 will finally introduce the generic inversion problem and how to address its main criticalities.

Chapter 4 introduces, for the first time, the use of Truncated Singular Value Decomposition (TSVD) as a direct inversion technique, providing both the mathematical justification for this approach and the reasons for its adoption.

Chapter 5 presents the foundational concepts of iterative imaging inversion techniques, focusing on the Algebraic Reconstruction Technique and the Sparse Majorization-Minimization approaches. It discusses the main advantages and disadvantages of each method to motivate choices, outcomes, and performance limitations. Chapter 6 describes the main system descriptors that severely affect the system performance. The section is also aiming at cross-validating model assumptions coming from Chapter 2.

The last Chapter 7 analyzes the pros and cons of each technique in detail, highlighting their strengths and weaknesses from a practical perspective.

Chapter 8 outlines future work, focusing on improving the current raw model using insights from previous techniques in the EM scanning field.

CHAPTER 2

RIS-AIDED RADIO FREQUENCY IMAGING

This chapter presents the forward model related to the RIS-aided imaging system and the foundational concepts that underpin this thesis. While none of the topics covered here are novel, their introduction is essential for a clearer comprehension of subsequent discussions and to establish the notation used throughout the thesis.

2.1 Reference scenario

The system configuration simplifies a real scenario, sticking with convenient geometry and propagation assumptions [8]. As depicted in Figure 2, two single antenna Access Points(APs) are located on a plane parallel to the xy-plane. The 2D target and RIS panel are placed parallel to this plane as well. The WiFi system is based on the IEEE 802.11 protocol. The RF communication systems are always affected by multipath negative impacts. The multipath effect occurs when signals travel multiple paths from the transmitter to the receiver due to reflection and diffraction, dispersion, or scattering. These multiple paths cause the signal to arrive at the receiver at different times and slightly different frequencies, resulting in distortion and interference. The multipath effect can lead to fading, where signal strength fluctuates rapidly, impacting the quality and reliability of communication links. Signal processing techniques like equalization and diversity reception are used to mitigate the effects of multipath propagation. Since a larger bandwidth can worsen the multi-path effect, the WiFi solution mitigates this by partitioning the available spectrum into a set of narrow, orthogonal frequency channels using Orthogonal Frequency-Division Multiplexing (OFDM). This ensures more robust communication. Additionally, the 40MHz channel benefits from being less subject to wavelength dispersion and attenuation factors.

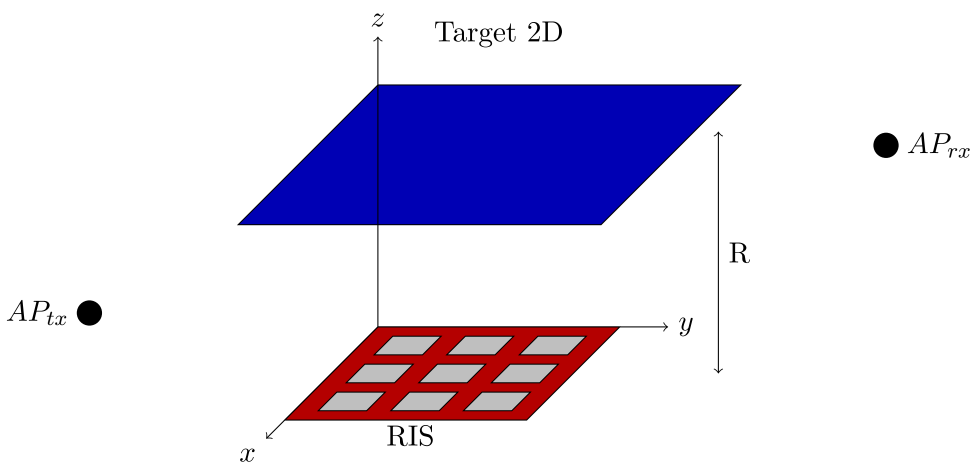

Figure 2: Problem's geometry: a single antenna AP transmits and illuminates the environments, while a second AP collects the scattered signals

As a starting configuration, a single channel of 40MHz bandwidth is uniformly sampled 30 times in the frequency domain. The choice of the number of samples and the spanned bandwidth will be further investigated to better evaluate potential imaging improvements in Chapter 6.

RF imaging can significantly benefit from the use of many narrow-band channels for two reasons. First, employing monochromatic signals at different frequencies allows for using very simple antennas, such as short dipoles. This aligns with the goal of achieving a low-hardware implementation for RF imaging systems. Second, many sub-carriers lend depth to the reconstructed image. The greater achievable diversity across the set of measurements enriches the available information about the reflective profile. The use of multiple frequencies can be intuitively seen as working at a single frequency with many physically different geometries to span over all possible phase correction configurations. This would enhance conditioning for the inversion problem and the transport matrix would be very directive toward the point of interest.

The main distinction between geometries comes from the limitations on the spatial frequency domain examined by the RIS panel rather than from changes to the model itself. The antenna location does not change the underlying forward model, but it does impact the quality of the images produced. Influencing spatial sampling alters the information to be retrieved. The transmitting and receiving Access Points are displaced orthogonally to both the RIS panel and the thin target of interest. As mentioned, this assumption is critical to keeping the scalar field assumption. The target object is highlighted in blue in Figure 2 .

The profile target is modeled as an M×M matrix of discrete scattering points densely distributed across the region of interest(ROI). The reflectivity continuous space function is discretized with a spatial sampling step equal to $\Delta = 2$ cm according to the expected wavelength of the RF field, and the total number of pixels is set to M = 50 elements. The imaged object is arranged in a column vector of M^2 elements through a lexicographic ordering of the 2D profile.

2.2 Imaging resolution at RF

For RF imaging, the advantage of penetrating obstacles along the Line-Of-Sight(LOS) has two main drawbacks. First, as aforementioned, mmWaves leads to an effective aperture smaller than the physical antenna aperture L_a, worsening the imaging spatial resolution. For example, the effective aperture of a short dipole varies with frequency as

$$A \propto \frac{\lambda^2}{4\pi} = \frac{c^2}{4\pi f^2} \tag{2.1}$$

The effective aperture is significantly affected by the spread and broadening of the beam width. In other words, when the physical size of an antenna approaches the wavelength, diffraction phenomena occur, leading to poor spatial resolution. From a different perspective, the antenna aperture would need to increase accordingly to keep a good spatial resolution at lower frequencies with unchanged infrastructure and physical geometry. This cannot be compensated merely by increasing the number of antennas, especially given the primary goal of reducing hardware complexity.

The second issue concerns the 40 MHz narrow-band channels used in WiFi. This problem can be better understood through radar systems, where resolution is related to two main aspects. First, range resolution refers to the ability to distinguish between different objects within the same Line-Of-Sight (LOS). The depth is probed using a frequency-changing pulse width, with the resolution limited by the following equation:

$$\Delta R \leq \frac{c\tau}{2} \tag{2.2}$$

A wider bandwidth is required to increase the range of investigation, and similarly, a narrower pulse width can enhance resolution. Unfortunately, in WiFi systems, the pulse width cannot be adjusted freely due to protocol spectrum partitioning. In RIS-aided WiFi systems, imaging does not involve pulse chirping over a wide spectrum. Instead, the narrow-band frequency channel is sampled by time-harmonic waves to ensure variety in measurements through spatial and phase diversity. Second , the frequency choice impact the Cross-range resolution $\Delta\phi_r$, also known as azmuth resolution.

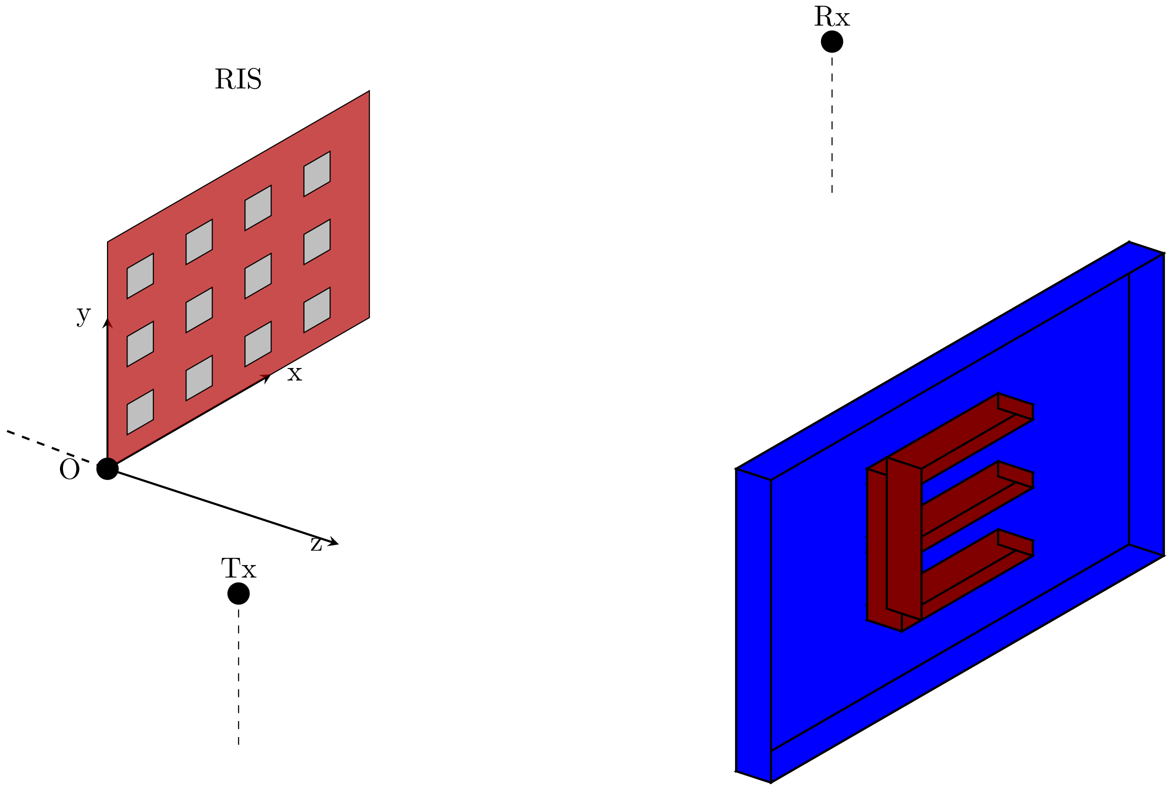

Figure 3: 3D view of problem's geometry for Wi-Fi imaging system with two *short dipoles* APs illuminating the EM environment made of RIS(red panel) and target(Blue panel)

Cross-range resolution is defined as the minimum distance between two adjacent scattering centers, orthogonal to the Line-Of-Sight (LOS) of the radar, that can be resolved as separate entities in the radar image or data. It characterizes the ability of the system to resolve fine details and structures perpendicular to the direction of motion or range dimension. Cross-range resolution is expressed as:

$$\delta_x = \delta_y = \theta \cdot R \approx \frac{\lambda_c}{L} R \tag{2.3}$$

where θ represents the beam width, which is reasonably assumed to be the ratio of the incident field wavelength to the antenna aperture size. R denotes the average slant range separating the antenna from the target. This resolution depends on the q_{th} RIS reflector and the m_{th} scatterer. The R is taken as the average distance between the two panels to stick with the theoretically expected results. The scanning resolution of the target is affected by the amplitude and phase of a scattered wave and the way the spatial frequency domain is encompassed. The key point in specific RIS-aided systems imaging is the spatial distribution of the smart and programmable reflectors deployed in many mirrors to the target. For this reason, the use of narrow-band channels from the WiFi standard carries out the practical issue of non-resolvable paths between direct and reflected paths

$$d_{\text{reflected}} - d_{\text{direct}} < \frac{c}{B} \tag{2.4}$$

In this scenario, the instrumental importance of motion for SAR systems is replaced by the RIS ability of the tuning phase to ensure variety in the measurements set.

2.3 RIS-aided advanced imaging

The system with the RIS panel operates like a MIMO system (red panel in Figure 3), allowing it to target specific scattering points within the Region of Interest. The ROI is characterized by a space reflectivity function $f(x, y)$, which can be simplified the ratio of reflected field to incident field

$$f(x,y) = \iint \frac{|\mathbf{E}_{ref}(x,y)|}{|\mathbf{E}_{inc}(x,y)|} dxdy \tag{2.5}$$

For the discrete expression, the ROI is sectioned in pixels. Each i_{th} pixel discrete reflectivity is defined over a small rectangular area

$$v_i = \int_x^{x+dx} \int_y^{y+dy} \frac{|\mathbf{E}_{ref}(x,y)|}{|\mathbf{E}_{inc}(x,y)|} dxdy \tag{2.6}$$

The v_i, representing the centroid of the 2D square, is ultimately encoded in binary digital form by comparing the normalized integral with a threshold. A real scenario resembling this condition of the sharp contrast between high and low reflectivity regions may be a thin metallic object. If the antenna is very directive, the cone turns into a 2D rectangle function optimally '*scanning*' the i_{th} pixel. According to the model, the RIS functions as a Uniform Rectangular Planar Array (URA) with uniform sampling in both directions. The aperture expands as the size of the planar array increases. Since the size directly depends on the number of elements in the array, the RIS enhances the overall aperture as the number of elements grows.

$$L_{URA} = \mathrm{d} \cdot \mathrm{N}_{side} \tag{2.7}$$

As highlighted by Equation 2.3, on the one hand, the lower wavelength limits the resolution. On the other hand, the higher the number of cells, the more effective the RIS in steering the beam toward a scatterer. The number of cells is set according to the required or desired resolution.

Reflective Intelligent Surfaces are panels made of discrete cells or ”tiles” that can change the phase of the impinging field to boost power at the receiver side[9]. In practice, the RIS phase tuning is performed by adapting the biasing voltages through a smart controller, which usually dominates the energy consumption at a RIS[10].

These tools are very promising in a wide set of applications. RIS has various outstanding features, and their integration into RF-communication systems can enormously boost spectral efficiency and performance.

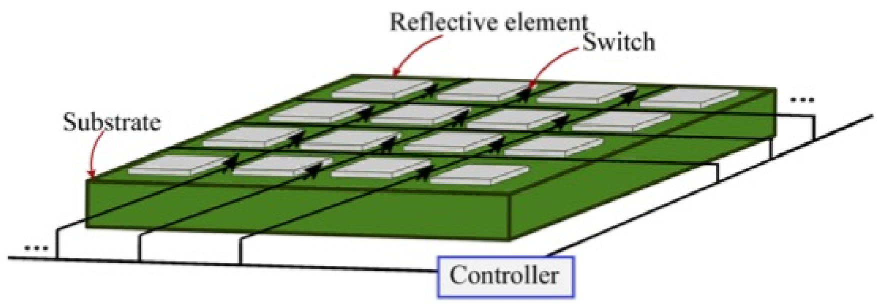

Figure 4: Reflective Intelligent Surface illustrative view

First, RIS act as smart programmable panels made of passive reflectors. They can improve performance, increasing the number of elements while requiring low hardware and energy costs.

Second, their use benefits energy efficiency as they do not require relevant active power. As mentioned earlier, the RIS reflectors are ideally passive and therefore do not alter the amplitude of the incoming signals.

Third, the passive nature of such surfaces carries out a negligible noise injection inside the propagation system. Lastly, the use of RIS in RF communication has proven to be effective in enhancing wireless high-capacity communications [11]. An accurate RIS design could potentially enable In-Band Full-Duplex (FD) communication at the free-space level. This would allow data to be transmitted and received simultaneously over the same frequency channel, significantly increasing communication efficiency.

RISs are made of a set of PIN diodes to be smartly polarized through an FPGA or digital controller with each cell phase tuned with a proper DC bias voltage. The most convenient option calls for simple, elementary cells able to perform 1-bit phase correction, both for fabrication and energy efficiency reasons. The extra phase shift applied by each cell primarily modifies the propagation phase of the impinging wave without directly affecting the steering angle. However, the highly directive final beam comes from combining all small contributions from cell phase shifts. Smart programming achieves an equivalent modification of the Snell law.

This new relation clearly conforms to the principle of energy conservation. Energy is not created but is more effectively directed toward the target. The key advantage is that the power required for control and management is much lower compared to what is needed for an array to achieve similar performance. The EM energy is steered towards specific target points at the low cost of FPGA voltage programming of RIS elements. The usual trade-off in 2D RIS-aided imaging is established, with higher reconstruction quality achieved at a significantly lower hardware cost but with increased data processing complexity. From antenna theory, Half-Power Beam-Width is defined as

$$\theta_a = \frac{\lambda_c}{L_{RIS}} \tag{2.8}$$

where L_{RIS} is the aperture size, defined as $L = \mathrm{d} \cdot \mathrm{N}_{\mathrm{side}}$ according to URA theory[12]. This general expression ideally assumes an isotropic source. Realistically, the dipole is short enough to be negligible with respect to the usual mutual spacing in antennas in terms of physical aperture. This expression resembles SAR resolution in imaging mode, where a large aperture array is synthesized by moving a single antenna. The resulting sharper resolution comes at no hardware cost. The payoff rather consists of increased data processing complexity. Solving the (Equation 2.3) for N_{side} number of cells per RIS side

$$N_{side} = \frac{\lambda_c}{d \cdot \theta_{\mathrm{des}}} \cdot R \approx \frac{2}{\theta_{\mathrm{des}}} \cdot R \tag{2.9}$$

where the $d = \frac{\lambda_{max}}{2}$ complies with the largest bound to condition the problem without aliasing effects. The outcome is consistent with the intuitive idea. The more cells deployed, the higher the resolution of the imaging result. This remark is expanded in dedicated Chapter 6. More quantitatively, the system resolution improves as

$$\delta_{y,tx} \approx \theta_a R = \frac{\lambda_c}{L_{TX}} R \longrightarrow \delta_{y,RIS} \approx \frac{\lambda_c}{L_{RIS}} R = Q \cdot \delta_{y,tx} \tag{2.10}$$

The RIS can be a game-changer in simplifying the AP hardware requirements, increasing the overall efficiency of the system while keeping the same or even better imaging effectiveness.

2.4 RIS smart phase control

The ability to compensate for the phase shift between the direct and reflected paths is the breakthrough feature of RIS. To illustrate this, consider a single sample from the 40 MHz channel centered at $f_s = 5.825$ GHz, focusing on a single scatterer, such as a point. From the general expression of the transmitted electrical field, the phase shift over the **direct path** from the transmitter to the single point back to the receiver is

$$\phi^s_{\text{direct},1} = \mathbf{k} \cdot \mathbf{r}_{\text{direct}} = \frac{2\pi}{\lambda_s}(d_{tx,1} + d_{1,rx}) \tag{2.11}$$

The phase term related to the *reflected path* from the transmitter to the target pixel passing through the q_{th} RIS atom is

$$\phi^{s}_{\text{ref},1} = \mathbf{k} \cdot \mathbf{r}_{\text{ref}} = \frac{2\pi}{\lambda_s}(d_{tx,q} + d_{q,1} + d_{1,rx}) \tag{2.12}$$

The ideal RIS behavior corrects the phase to make the direct and reflected path coherently sum at the receiver end. The single q_{th} element phase correction is defined as

$$\theta^{s}_{q,1} = \phi^{s}_{\text{direct},1} - \phi^{s}_{\text{ref},1} \tag{2.13}$$

Let $\Theta_m \in \mathbb{C}^{Q\times 1}$ denote the vector of all phase corrections applied by the RIS cells for the selected point m. Each single point m belonging to the target is associated with a Θ_m vector configuration. The number of projection measurements is set equal to the M number of target points to determine the imaging problem.

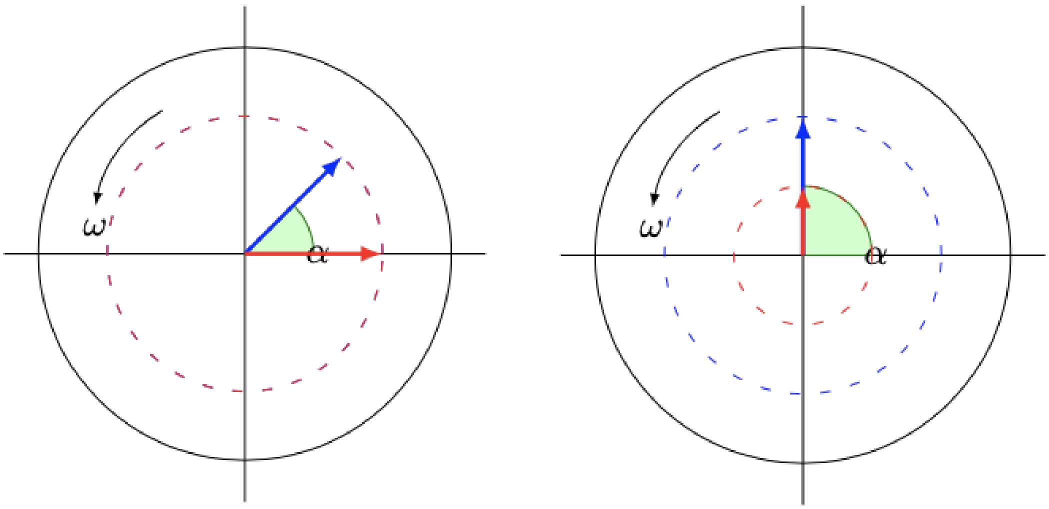

(a) Phase Effect (b) Amplitude Effect

Figure 5: Effect of free space scalar field propagation from transmitting to receiving AP

According to the URA model, the inter-element distance applies the half-wavelength principle so that $d = \frac{\lambda}{2}$. The RIS q_{th} cell is labeled grid-like with a double indexing (m_x, n_y). Assuming the RIS grid across the xy-plane, the optimal single-element phase correction becomes

$$\begin{aligned}\theta_{q,m}^{opt} &= \frac{2\pi}{\lambda}(d_{\text{tx},m} - d_{\text{tx},q} - d_{q,m}) \\ &= md \cdot \sin(\theta_{\text{tx}})\cos(\phi_{\text{tx}}) + nd \cdot \sin(\theta_{\text{tx}})\sin(\phi_{\text{tx}}) \\ &\quad + md \cdot \sin(\theta_m)\cos(\phi_m) + nd \cdot \sin(\theta_m)\sin(\phi_m) \end{aligned} \tag{2.14}$$

The double positive sign is related to the physics convention adopted for the spherical wave propagation. The RF-imaging main limit of decrease in resolution due to mmWave is now compensated by RIS improving physical aperture . The specific scenario introduces the additional non-idealities related to the finite, discrete number of achievable phase levels from each element and the number of cells.

The phase compensation is exact as long as each individual cell can handle continuous phase shifts with infinite precision and regulation. However, the most reasonable fabrication choice is based on simple "tiles" of the RIS achieving a $C = 2^b$ finite and discrete number of phase corrections according to b number of bits. RIS typically allows for only two-phases cells (0 or π). The phase correction is discretized, leading to a "quantization" error contribution to be considered. The absence of phase granularity is addressed during the data processing stage to ensure a more accurate interpretation of the results.

2.5 Scalar Electric Field

Throughout the description of the imaging system, the emphasis on lightweight hardware has been consistently highlighted. Given the relative simplicity of the electromagnetic model, it is crucial to clarify the underlying assumptions of this work. One key assumption is the scalar representation for the electric field.

The system is equipped with two single infinitesimal dipole antennas. The target is placed in the far field relative to the source, which enhances the reliability of the array-like modeling of the RIS. Short dipoles are advantageous as they produce a single polarized electric field. Specifically, in spherical coordinates, the electric field is expressed as:

$$\mathbf{E} = \begin{bmatrix} E_r \\ E_\theta \\ E_\phi \end{bmatrix} = \mathbf{E} = \begin{bmatrix} 0 \\ E_\theta \\ 0 \end{bmatrix} \tag{2.15}$$

Given the strongly omnidirectional pattern and the isolation of the element from other active sources (multi-element effect), the azimuth variation can be neglected. At the same time, the magnitude of the electric field is assumed to be approximately constant across both the target and RIS, thanks to the far field assumption. The wave propagating through free space has an electric field of the shape

$$E_\theta(r,\theta,\phi) = \left(\frac{1}{4\pi R_m}\right)\left(\frac{j\eta k I_0 L_{tx}}{2}\right) e^{j\frac{2\pi R_m}{\lambda}} = \zeta e^{j\frac{2\pi R_m}{\lambda}} \tag{2.16}$$

where I_0 is the current uniform across the source, η is free space impedance, k is the wave number, and L is the physical size of the transmitter. Lastly, the total distance covered by the wave is$R_m = d_{tx \to m} + d_{m \to rx}$ i. The convention for expressing the traveling spherical wave follows the standard used in physics. In this context, a positive argument in the exponential function denotes an outgoing wave. This important consideration implies a second feature: the scattered wave does not experience depolarization.

It is known that the depolarization effects can be ignored only if the wavelength is much smaller than the correlation size of the inhomogeneities in the object [13; 14]. The correlation size is fundamental in determining the nature of the scattered fields and directly impacts the resolution and accuracy of tomographic imaging. It also influences the complexity of the inverse problem, affecting the design and performance of the adopted reconstruction algorithms.

In general tomography, the correlation size of inhomogeneities refers to the spatial scale over which the properties of the medium change, i.e., permittivity or conductivity. When the correlation size L_{corr} is much smaller than the wavelength of the probing wave $L_{\text{corr}} = \lambda$ the inhomogeneities act as diffuse scatterers, causing complex multiple-scattering effects. This scenario is typically associated with the Rayleigh scattering regime. On the other hand, if the correlation size is comparable to or larger than the wavelength, the scattering becomes more structured and predictable. This is a common assumption for perfect electrical conductors(PEC) according to many scattering theoretical techniques(Physical Optics, Geometrical Optics,...). However, it is crucial to emphasize that the phase shifter does not introduce depolarization of the field. Any such change would apply a dyadic scattering tensor(affine transformation) to the electric field, altering the vectorial shape of the field and, generally, resulting in a loss of power at the receiver side. and lack of completeness for the current model.

2.6 Channel State Information and transport matrix

The Channel State Information matrix describes the wave propagation accounting for source properties, frequency dependency, and combination of sub-carrier contributions.

For the point on the target $m(x_m, y_m)$ the received signal $p(m)$ comes out of a coherent summation of direct and reflected paths across the RIS and the target

$$p(m) = \sum_{q=1}^{Q} \iint \alpha_q \cdot f(x, y) \cdot \beta(x, y, q) dxdy \tag{2.17}$$

The term α represents the attenuation factor from the RIS cell, which is unitary under the assumption of perfect reflectors. The function $f(x, y)$ denotes the 2D continuous reflective distribution function over the x-y plane. In other words, the reflectivity for the single m_{th} pixel is projected on a measure influenced by environmental features and surrounding points. The term $\beta(x, y, q)$ accounts for the signal falloff for each path, depending on the $\mathbf{Q}$ vector and the m_{th} phase configuration.

The complex term for signal falloff β is related to the object location both in magnitude and phase parts. First, at the receiver side, the amplitude of the wave scattered wave covering an overall distance $d_m = d_{tx,m} + d_{m,rx}$ from the source scales as

$$|\beta(x, y)| \propto \frac{1}{4\pi r} \tag{2.18}$$

Second, the wave experiences a time delay leading to a phase modification to the traveling wave $e^{j\frac{2\pi}{\lambda_s}d_m}$. Each point requires a different set of phases due to different distances and/or wavelengths. The direct path contribution only considers the electrical component of the transmitted electromagnetic field with a phase attribute depending on the target pixel. From the discussion in the previous paragraph, the direct path contribution for the m_{th} point is written as

$$\mathbf{n_d}(m) = \zeta e^{j\frac{2\pi R_m}{\lambda}} \tag{2.19}$$

The reflected path contribution from the transmitter to the m_{th} point through the q_{th} cell without considering the phase correction is

$$\mathbf{G}(q, m) = \zeta e^{j\frac{2\pi R_{q,m}}{\lambda}} \tag{2.20}$$

where $R = d_{tx\rightarrow q} + d_{q\rightarrow m} + d_{m\rightarrow rx}$ is the total distance covered by the wave. As mentioned, the RIS plays a crucial role in optimally shifting the phase of the reflected field to ensure that the two paths sum coherently at the receiver end. The complex scalar measure at the receiver is the result of combining all possible contributions:

$$p(m') = n_d(m') + \sum_{q=1}^{Q} e^{j\theta_{q,m'}} G_{q,m'} = n_d(m') + \mathbf{\Theta}^H(m') G_{q,m'} \tag{2.21}$$

where $\mathbf{\Theta}(m') = \{e^{j\theta_1}, e^{j\theta_2}, \ldots, e^{j\theta_Q}\}^H \in \mathbb{C}^{Q\times 1}$ is the vector of phase corrections applied by each RIS element. The single element for the CSImatrix is determined by

$$\mathbf{H}(1,1) = n_d(m') + G_{1,1}e^{+j\theta_1} + G_{2,1}e^{+j\theta_2} + \ldots + G_{M,1}e^{+j\theta_Q} \tag{2.22}$$

It is important to note that the vector configuration $\mathbf{\Theta}(m')$ is uniquely determined by the point of the target m' and by the measurement index. The single measurement is obtained from a convolution between the m_{th} row and the albedo itself in the shape of

$$\text{p(m')}{=}\mathbf{h_m} \circledast \mathbf{y} \tag{2.23}$$

where $\mathbf{h_m} = \left[h^*_{m,1}, ..., h^*_{m,M}\right]^H \in \mathbb{C}^{M,1}$ is the m_{th} row of the channel matrix. This will lead to a matrix expression of such problem given by

$$\mathbf{P} = \mathbf{H} \cdot \mathbf{y} \tag{2.24}$$

where the $\mathbf{y}$ refers to the albedo vector reflecting the transmitted field towards the receiver and the $\mathbf{H} \in \mathbb{C}^{M \times M}$ is the transport matrix, embedding all useful information about wave propagation. The Channel State Information simplifies the signal propagation description for the discrete model. At the same time, this approach makes straightforward the stacking of the CSI matrix $\mathbf{H}(q, m, s)$ at different sub-carriers to enrich information related to different frequency configurations.

A set of many sub-carriers extracted from a 40 MHz channel at 5.825 GHz improves reconstruction resolution. The advantages of this sampling method and the saturation in the frequency variety are discussed in Chapter 6. Each single sub-carrier corresponds to an optimization or inversion problem

$$\mathbf{P_s} = \mathbf{H}_s(\mathbf{\Theta}(\mathbf{M}), s) \cdot \mathbf{y} \tag{2.25}$$

On the one hand, the relatively narrow bandwidth of WiFi channels poses a challenge, making the variety of fields non-resolvable and preventing the paths from being considered separately. However, the system employs two types of strategies to enhance the differentiation of distinct points. First, the multitude of sub-carriers ensures variety in the set of available data. It is not only about having a wider span of data, but it also cares about the diverse set of information combined together.

The diverse measurements obtained from the discrete samples of the imaged target ensure that a solution from the inversion algorithm exists, although it may not be unique. This operation equivalently spans the width of the image reconstruction solution.

Second, the operating frequency offers a variety of degrees, enhancing the detection of contrasts and leading to sharper results.

Therefore overall transport matrix has to account for such an effect

$$\mathbf{H}(\boldsymbol{\Theta}(\mathbf{M})) = \sum_{s=1}^{S} \mathbf{H}_s(\boldsymbol{\Theta}(\mathbf{M})), s) \tag{2.26}$$

This matrix contains all the information needed once the geometry and propagation conditions are fixed. The improved imaging performance comes with a reduced computational complexity. Characterizing the Channel State Information (CSI) $\mathbf{H}$ matrix is a one-time operation. Any target can be imaged with that same indicated resolution.

2.7 Forward model for noisy environment

To the best of the author's knowledge, there is only a single work available in the literature that specifically addresses the application of RIS to imaging and target detection[8]. Although analyzing accurately the effect of phase discrete correction carrying out a quantization on the overall system performance, the discussion is still limited to ideal electromagnetic environment.

It would be indubitably interesting to look into different methods, such as the TSVD described in Appendix B, to evaluate imaging and detection performance when the propagation happens in a strongly corrupted and noisy environment. For sake of simplicity, the noise artificially injected into the system is modeled as Gaussian

$$V \backsim G(0, \sigma_v^2) \tag{2.27}$$

The shape of zero-mean Additive White Gaussian Noise(AWGN) with σ_v^2 variance overlaps with the albedo function, embedding all detrimental factors affecting the idealized model. The final model for the single carrier case is described as

$$\mathbf{P} = \mathbf{H}\mathbf{y} + \mathbf{V} \tag{2.28}$$

where the vector $\mathbf{V}$ represents the AWGN superimposed to the convolution model for the albedo information retrieved through the channel information. The white noise is overlapped to the useful signal buut is assumed to be orthogonal to the convolution of the channel with the input. Conversely, the spatial correlation of noise among scatterers is typically non-zero because the paths through adjacent points on the target are quite similar, making it unreasonable to assume otherwise.

CHAPTER 3

IMAGING INVERSION PROBLEM

The imaging process is built by addressing three fundamental questions. First: *what is the quantity of interest to be reconstructed?*. The quantity to be reconstructed through the model is the planar reflectivity function of the target. In general this is a continuous function of the space for an object. The reflectivity basically represents the magnitude of the ratio between the transmitted and the received field. In the specific context, the profile is discretized, and each pixel is examined in the center. In each point, the reflectivity function takes a real value. The target of interest is sampled in many pixels of pixels with a step $\Delta = 2$ *cm*.

0	0	0	0	0	0	0	0
0	0	0	0	0	0	0	0
0	0	1	1	1	1	0	0
0	0	1	0	0	0	0	0
0	0	1	1	1	0	0	0
0	0	1	0	0	0	0	0
0	0	1	1	1	1	0	0
0	0	0	0	0	0	0	0
0	0	0	0	0	0	0	0

Figure 6: *Problem Formulation* - Discretization of the reflectivity function $a(x, y)$ for a metallic E-shaped object.

The albedo vector $\mathbf{y} \in \mathbb{C}^{M\times 1}$ is then the discrete version of the reflectivity profile of the 2D region where each element corresponds to a pixel, coded into a binary configuration according to the likelihood of the existence of the target for the specific location. The schematic idea is outlined in Figure 6. The generic unknown albedo element takes the shape

$$y_i = \begin{cases} 0 & \text{if the object is not in in that pixel} \\ 1 & \text{if the object exists in that position} \end{cases} \tag{3.1}$$

Second question: *what is model used to study the object and its surrounding environment?* The imaging system is given by a couple of access points (APs) with poor directivity and scarce beam-tuning capability. The APs are equipped with simple dipoles, whose spherical propagation is described using Green function. The electric field related to propagating waves is given by

$$\mathbf{E}(\mathbf{r}) = \left(\zeta e^{-j\frac{2\pi}{\lambda}\mathbf{r}\cdot\hat{r}}\right)\hat{p} \tag{3.2}$$

where $\mathbf{r} = \mathrm{R}\cdot\hat{r}$ indicates the radial vector pointying in a given direction from the source. I_0 is the constant magnitude of the current uniformly feeding the radiator, $\mathbf{k} = k_x\hat{i}+k_y\hat{j}+k_z\hat{z}$ is the wave vector indicating the power propagation direction. The polarization unit vector $\hat{p}$ indicates the direction along which the electric field changes over the time. The performance of RF imaging or detection can improve acting on single, double polarizations or circular polarization, as proven in the past [15], [16], [17]. However, the more numeric and conceptual basis of this work will not focus on polarization effects on the imaging resolution.

The final question is: *what is the most suitable inversion algorithm to address the inversion problem?* The physical model takes to the definition of a CSI square transport matrix $\mathbf{H} \in \mathbb{C}^{M \times M}$. The transport matrix embeds all helpful information about the channel and the signal propagation to link the unknown binary vector to, the right-hand vector for the inversion problem, given by the set of measurements. The binary albedo input $\mathbf{y} \in \mathbb{C}^{M \times 1}$ represents the unknown target to be imaged. In reconstruction problems, the transport matrix can be referred to as the *convolution kernel* of the inversion problem. The size of vector of measurements $P \in \mathbb{C}^{M \times 1}$ is set equal to the M number of points forming the object of interest. The resulting linear system is formulated as

$$\mathbf{H}\ \mathbf{y} = \mathbf{P} \tag{3.3}$$

The goal is to solve the inversion problem to retrieve the original unknown image. The optimal solution is determined according some minimum square error (MSE) or least-squares criterion

$$\hat{\mathbf{y}} = \min_{y} \|\mathbf{H}\ \mathbf{y} - \mathbf{P}\|_2^2 \tag{3.4}$$

An important distinction from typical estimation cases should be highlighted. Instead of using an estimate of the channel based on input and noisy output, the channel embeds a set of regressors, represented by the $\mathbf{\Theta_m}$ vectors. The albedo is the unknown variable to be determined using a priori information, CSI, and measured data $\mathbf{P}$. In ideal, well-posed problems, the matrix $\mathbf{H}$ is non-singular and invertible. The optimization problem is strictly convex, ensuring a unique optimum solution. The inverse matrix can then be used to solve the problem.

$$\mathbf{y}_{opt} = \mathbf{H}^{-1}\mathbf{P} \tag{3.5}$$

While this scenario has a clear statement and a robust solution to small changes in the input, ill-posed problems may exhibit sensitivity to changes in initial conditions or input data.

The low condition number of the $\mathbf{H}$ matrix is a common challenge in inversion problems. Small deviations in the input can greatly amplify measurement errors, primarily due to the difficulty of obtaining an independent set of measurements. In square matrices, the notion of ill-conditioning arises when eigenvalues approach zero, much like how rank deficiency occurs when eigenvalues equal zero. Small singular values indicate potential ill-conditioning. In other words, certain rows of the transport matrix are close to being linearly dependent.

As typically happens, the a-priori knowledge about the target, the system, and the propagation conditions can help us to adopt the best inversion strategy. The transport matrix shows some helpful features of the search for valid inversion approaches. The matrix $\mathbf{H}$ is strongly sparse. Most of its non-diagonal elements are expected to be nearly zero. The sparsity can be extremely helpful during the inversion process as it implicitly rules out some solutions. The matrix **H** is also square, with the number of measurements (rows) matching the number of target points to avoid the system being under-determined. This choice addresses the issue of being under-determined but does not immediately improve the conditioning.

(a) Least squares(standard LS) (b) L-2 regularization

Figure 7: Regularization 3D comparison

Lastly, the asymmetric nature of the transport matrix significantly limits the range of algorithms that can be investigated. This can be illustrated through a trivial analysis. The element $\mathbf{H}_{1,2}$ results from the linear combination of the reflected field from the second scatterer $m = 2$, weighted by the $\mathbf{\Theta}_1$ RIS phase correction configuration.

Since the RIS approach aims to maximize the terms along the diagonal, the off-diagonal elements, such as $\mathbf{H}_{1,2}$, are progressively penalized. Conversely, $\mathbf{H}_{2,1}$ is the result of the linear combination of reflected fields determined by the second phase configuration vector Θ_2, which acts on the first pixel. The inversion problem is then ill-posed and the solution is typically to be found through some *minium-norm* criteria within the space of admissible options. The choice to prioritize a lower-norm physical solution is based on both physical and intuitive reasons. Physical systems tend minimize their energy configuration. For example, a ball placed on the edge of an incline will naturally roll down to the lowest point, converting its potential energy into kinetic energy. Similarly, the inversion problem aims to find the solution minimizing the 'dispersion' of the reconstructed image compared to the reference ground. Intuitively, the minimum norm solution is concentrated around the expected profile, potentially resulting in a clearer and sharper, reconstruction. In problems involving sparse, low-rank matrices the inversion makes use of such properties and a priori information. A common solution to the ill-conditioning of the problem is to use regularization process. This is a common scalarization method adding a penalty factor, according to the unknown estimate value, to solve bi-criterion strongly ill-posed problems.

These methods attempt to mitigate the effects of small singular values by attenuating them or completely eliminating them from the computation of the pseudo-inverse[18].

3.1 Regularization in inversion problems

In the imaging field, the inversion problem is generally ill-conditioned, leading to several considerations. The transport matrix features a wide sparsity pattern and a quite low rank, which means the valid, minimum-norm solution has to be found in a much smaller sub-space of the original space of solutions for the linear model

$$\mathbf{P} = \mathbf{H}\mathbf{y} + \mathbf{V} \tag{3.6}$$

where:

- $\mathbf{P}$ is the observed signal (vector),
- $\mathbf{y}$ is the original signal (albedo vector),
- $\mathbf{H}$ is the CSI matrix at single frequency
- $\mathbf{V}$ is the noise (Additive White Gaussian Noise, Stochastic process).

The sparsity of the $\mathbf{H}$ matrix also calls for methods highlighting a few relevant eigenvalues. In such a context, the regularization of the inversion problem plays a crucial role. The regularization function is applied as a penalty to the standard formulation of the *noiseless* imaging problem

$$J(\mathbf{y}) = \|\mathbf{H}\hat{\mathbf{y}} - \mathbf{P}\|_2 \tag{3.7}$$

The type of function employed, the a-priori knowledge about the solution, and the regularization intensity can impact the conditioning and the quality of the solution. The regularization is performed either directly or iteratively on the solution according to the adopted approach.

The full dissertation about the unknown albedo reconstruction is not fully provided, and many theoretical underlying aspects are left to a more detailed investigation of the topic[19; 20; 21]. However, the brief derivation of the solution and the need for regularization are provided below. First, the albedo is represented as a vector following the lexicographic ordering for the matrix to vector reshaping. The *convolutional channel* is given by a channel matrix multiplied by the albedo to provide noisy measurements, with noise coming both from model limitations and artificially injected AWGN.

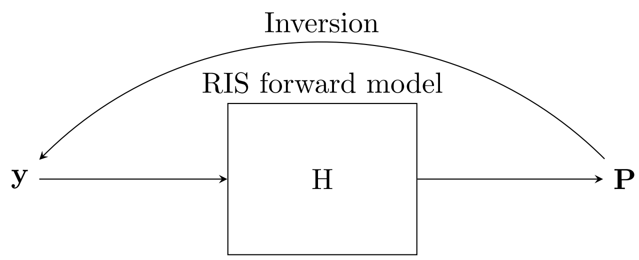

Figure 8: Block scheme of imaging system

The CSI depends on the specific coordinate of the point in the region of interest. This coordinate contributes to the RIS vector phase configuration. From the (Equation 3.7), the derivation of the solution explains the limit for the inversion problem. The estimated output signal $\hat{\mathbf{P}}$ is given by:

$$\hat{\mathbf{P}} = \mathbf{H}\hat{\mathbf{y}} \tag{3.8}$$

Where $\mathbf{H}$ is the filter matrix with the MSE:

$$J(\mathbf{y}) = E\left[\|\mathbf{P} - \hat{\mathbf{P}}\|^2\right] = E\left[(\mathbf{P} - \hat{\mathbf{P}})^H(\mathbf{P} - \hat{\mathbf{P}})\right] = E\left[(\mathbf{P} - \mathbf{H}\hat{\mathbf{y}})^H(\mathbf{P} - \mathbf{H}\hat{\mathbf{y}})\right] \tag{3.9}$$

After some lengthy derivation and assuming does not depend on propagation conditions

$$\frac{\partial J(\mathbf{y})}{\partial \mathbf{y}^{\mathbf{H}}} = -E[\mathbf{H}^H \cdot \mathbf{H}]\mathbf{y} - E[\mathbf{H}^H \cdot P] = 0 \Rightarrow E[\mathbf{H}^H \cdot \mathbf{H}]\mathbf{y} = E[\mathbf{H}^H \cdot P]] \tag{3.10}$$

The low rank of the transport matrix H also implies a singular $H \cdot H^H$. It is now clear that the CSI matrix has a strong correlation among rows for adjacent target elements, justifying low rank and non uniqueness of the solution. The bi-criterion solution can be re-written in a regularized shape to let the solution stick with some preferred condition

$$\hat{\mathbf{y}} = \|\mathbf{H}\hat{\mathbf{y}} - \mathbf{P}\|_2 + \gamma\|\hat{\mathbf{y}}\| \tag{3.11}$$

with$\|\cdot\|$ norm applied to the solution and weighted by γ >0 regularization parameter tuning the desired degree of penalty forced on the solution.

The two main regularization penalty functions are L_1-Lasso and L_2-Tikhonov regularization. Both of them are based on norms penalty factors added to the cost function (Equation 3.7). The Tikhonov regularization is particularly suited for Mean-Square-Error analysis to express a penalty affecting estimators consistently smooth. Figure 9 displays the graphical intuitive comparison of the two methods.

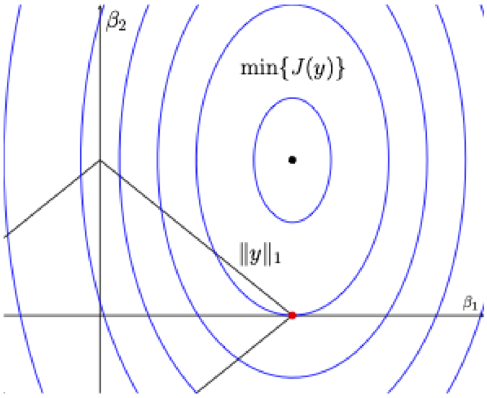

(a) L_1 Lasso

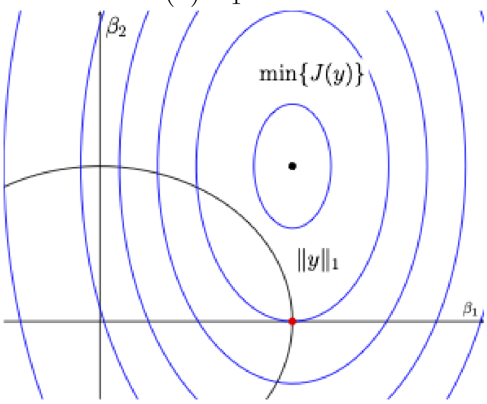

(b) L_2 Tikhonov regularization

Figure 9: Lasso and Tikhonov constraint regions get different coefficient locations on the diamond and circle for the same loss function.

In the simplified R^2 space solution, the set of infinite valid solutions due to the illconditioned problem is described by the contour elliptic curves. Each ellipse identifies a set of equivalent solutions, providing the same cost function value. The plots in Figure 9 are a top view of a 3D visualization of the function The regularization term by a penalty factor commonly increases the bias of the algorithm from the *'exact'* solution, i.e., the intersected solution is further away from the optimum. The graphical view gives a different perspective to visualize the original problem (Equation 3.7) when subject to an L_p constraint.

The minimization of L_1 regularization function typically leads to a solution where many coefficients lie on the axes (i.e., are exactly zero), intersecting with the corners of the diamond, enhancing the sparsity pattern. On the one hand, this approach prevents the system from being strongly sensitive to the outliers in the measurements, i.e., unexpected spiking values are quite smoothed to reduce their effect on the final solution. For this reason, this kind of regularization is also referred to as *robust* estimation. On the other hand, the L_1 norm function doesn't suppress the small residuals as much. When a straight L_1 regularization is employed, the optimal solution is forced to intersect the L_1-norm unit 'ball', or a *diamond* in the coefficient space. The corners of this diamond occur when one or more coefficients are zero. The new objective function is

$$\hat{\mathbf{y}} = \min_{y} \|H\mathbf{y} - \mathbf{P}\|_2^2 + \gamma \|\hat{\mathbf{y}}\|_1^2 \tag{3.12}$$

The benefit is that it provides a convex function that leads to a valid solution according to some prior information or intuition about the solution shape. Besides, this method is not suitable for iterative techniques. This comes from the non-differentiable property of the L_1 norm at the cusps due to the solution approaching the second derivative singularity of the norm, which occurs exactly within the space subset of interest.

L_1-norm regularization is strongly based on a heuristic approach, especially when dealing with huge matrices. A second example is the regularization Tikhonov, based on Euclidean or L_2 norm. This method introduces a more 'circular' penalty function, encouraging solutions with smaller coefficients overall. This means no coefficients are exactly set to zero. This method has a huge benefit in terms of first derivative continuity and the modified cost function becomes

$$J(\mathbf{y}) = \frac{1}{2}\|\mathbf{H}\hat{\mathbf{y}} - \mathbf{P}\|_2 + \frac{\gamma}{2}\|\mathbf{y}\|_2 \tag{3.13}$$

The differentiable property of such a penalty function makes it convex in a strict sense, and the objective smoothness allows for an iterative search for the solution of interest.

CHAPTER 4

TRUNCATED SINGULAR VALUE DECOMPOSITION

(Previously published as part of Tortoriello, C., Erricolo, D., and Oliveri, G.: Wave Manipulating RIS for Enhanced Tomographic Imaging: Concept and Recent Advances. In 2024 United States National Committee of URSI National Radio Science Meeting (USNC-URSI NRSM), pages 236–237, 2024)

RF-imaging problems are inherently ill-posed, leading to an infinite number of potential solutions. However, solutions that minimize energy are generally less affected by noise, which arises from the CSI structure and the overlapping patterns of the data. Common channel conditions tend to affect multiple points on the scatterer similarly. Consequently, nearby points often have similar phase configurations for the RIS panel, causing some rows of the matrix $\mathbf{H}$ to approach linear dependence. A poorly conditioned system shows a pronounced null space, indicating a strong correlation among the columns of $\mathbf{H}$, making it less likely for them to be linearly independent. The discussion from Chapter 3 highlighted the need for regularization to address ill-posed problems.

The application of regularization techniques helps to mitigate and isolate the effects of inconsistent or irregular singular values. Every time a small error occurs in the measurements vector $\mathbf{P}$, the solution would be dominated by small singular values. Inversion techniques involve either direct methods or iterative ones. On the one hand, iterative methods are characterized by a lower complexity as they leverage the low rank and sparse nature of the problem to ease the resources demand from the whole imaging process. A decrease in complexity does not necessarily indicate poor convergence. In fact, various strategies can be employed to enhance performance, though they may slightly slow down the convergence process. On the one hand, *direct* methods search for a solution to the problem in a monolithic step. These techniques are direct as they return the final solution directly out of the computation. These techniques can usually achieve sharp and effective results at the cost of high computational complexity. A popular direct method is Truncated Singular Value Decomposition (TSVD), which provides regularization similar to Tikhonov regularization. The difference is that TSVD attains filtering in a more discrete and sharp way rather than applying a smoothing effect. According to the SVD direct approach, a given H matrix can be decomposed as

$$\mathbf{H} = \mathrm{U}\Sigma\mathrm{V}^{(H)} \tag{4.1}$$

where $\mathbf{U} \in \mathbb{C}^{M\times M}$and $\mathbf{V} \in \mathbb{C}^{M\times M}$ are the matrices spanning respectively the row and the column space of $\mathbf{H}$. They also represent the whole set of left and right singular vectors, tightly connected to the eigenvalues decomposition of $(\mathbf{H}^H \cdot \mathbf{H})$ and $(\mathbf{H} \cdot \mathbf{H}^H)$ matrices. All singular values are displaced along the diagonal of the Σ, sorted in descending order. This matrix is closely related to the eigenvalues of the matrix and can basically embed lower-rank information.

For a well-posed problem, the H matrix would exhibit a full rank, with a positive definite spectrum of eigenvalues and a couple of U and V matrices being orthogonal. The image reconstruction linear system to be solved is outlined as

$$\mathbf{H}\mathbf{y} = \mathbf{P} \tag{4.2}$$

In common with many inversion problems, this issue is ill-posed and may have infinitely many solutions. The goal is to find the minimum-norm or 'minimum energy' solution. It can be proved [19] that this solution is given by the Moore-Penrose pseudo-inverse of the **H** matrix, defined as

$$\mathbf{H}^{\dagger} = \mathbf{H}^{H}(\mathbf{H}^{H} \cdot \mathbf{H})^{-1} \tag{4.3}$$

leading to the minimum norm solution

$$\mathbf{y}_{\mathrm{opt}} = \mathbf{H}^{\dagger}\mathbf{P} \tag{4.4}$$

The stability of the obtained solution can be assessed using the *condition number* of the matrix **H**. Let M represent the maximum stretch of the vector **y** after applying the affine transformation matrix given by CSI matrix M $= \max \frac{\|\mathbf{Hy}\|_2}{\|\mathbf{y}\|_2}$ Similarly, let m denote the minimum stretch m $= \min \frac{\|\mathbf{Hy}\|_2}{\|\mathbf{y}\|_2}$ The condition number $k(\mathbf{H})$ is given by:

$$k(\mathbf{H}) = \frac{M}{m} \tag{4.5}$$

This quantity evaluates how variations in the observed vector, such as measurement errors, affect the final result. For a generic, rectangular matrix, the condition number can also be expressed as:

$$k(\mathbf{H}) = \|\mathbf{H}^{\dagger}\| \cdot \|\mathbf{H}\| \tag{4.6}$$

If $k(\mathbf{H})$ is *small*, the linear system is well-conditioned, and the solution becomes more robust. Small perturbations of the output data result in damped variations of the final solution. The higher the condition number, the poorer the image quality. For a poorly-conditioned system, a high condition number indicates that the channel matrix is merely a numerically inadequate approximation of one that should satisfy the relationship $\mathbf{H}^{\dagger} \cdot \mathbf{H} = \mathbf{I}$, where $\mathbf{I}$ is the identity matrix.

Therefore, a higher conditioning number can lead to instability problems. From a different perspective, the conditioning number can be written through H matrix eigenvalues as

$$k(\mathbf{H}) = \frac{\lambda_{max}(\mathbf{H})}{\lambda_{min}(\mathbf{H})} \tag{4.7}$$

Some singular values have to be retained as a stabilization measure. The ill-conditioning of the problem is addressed by truncating the number of 'useful' singular values. A k truncation value is chosen such that $\sigma_j = 0 \quad \forall j > k$. This provides guidance on how many singular values should be preserved to manage the condition number effectively. The regularized pseudo-inverse can be determined by reversing the SVD decomposition relation[22]

$$\tilde{\mathbf{H}}^{\dagger} = \mathrm{V}_k \Sigma_k^{-1} \mathrm{U}_k^H \tag{4.8}$$

The final matrix has the same size as before because the truncation of both $\mathbf{U}^H$ and $\mathbf{V}$matrices provides the same size matrix where only the non-redundant information is actually analyzed.

The most general solution using the Discrete Picard Condition(See Appendix A) and the *Singular Value Expansion* (SVE) leads to

$$\mathbf{y}_k = \sum_{j=0}^{k} \frac{\mathbf{u}_j^H \mathbf{P}}{\sigma_j} \mathbf{v}_j \tag{4.9}$$

The truncation works fine for the sharp regularization, retaining the useful singular values while cutting off the small, unstable ones[23; 24]. The multiple-carrier image resolution also depends on the k truncation parameter choice, acting as a regularization parameter[25]. If the summation in (Equation 4.9) includes more contributions from singular values, the solution norm $\|\mathbf{y}\|_2$ will immediately start to diverge, as σ_j progressively approaches zero. The higher the truncation parameter, the more singular values are comprised in the solution, and the more divergent the Euclidean norm of the solution would be from the expected one. A proper k choice is required for the heuristic and mathematical foundation of the problem .

4.1 Truncation parameter choice

There are three main ways to determine the optimal truncation parameter. The first is based on the Discrepancy Principle which prescribes the truncation index k to be the largest one ensuring

$$\|\mathbf{H}\hat{\mathbf{y}} - \mathbf{P}\|_2 \leq \eta \cdot \epsilon \tag{4.10}$$

where $\eta > 1$ and ϵ is the maximum admitted discrepancy of measurements from a real case scenario. This approach relies on a-priori information about the desired residual but the accuracy of our algorithm is not immediately set as it depends on the specific target and the environmental conditions.

The second way relies on statistical characterization of the parameter according to Cross-validation methods. The huge advantage of this class of methods is the potential capability of determining k from a-priori propagation and channel information(physical geometry, number of bits for RIS correction, etc.). The optimization problem to determine the optimal truncation parameter adds complexity to the main problem. The most successful algorithm is the Generalized cross-validation (GCV), setting the transport matrix only relying on offline electromagnetic environment information [26]. The third heuristic method is the so-called *L-curve* approach[27]. A heuristic solution is a method for solving a problem that may not guarantee an optimal result but focuses on finding a reasonably good solution efficiently. It is designed to be practical and fast, often prioritizing speed and simplicity over achieving the perfect solution. The choice for the truncation parameter is empirically based on visual inspection of the plot.

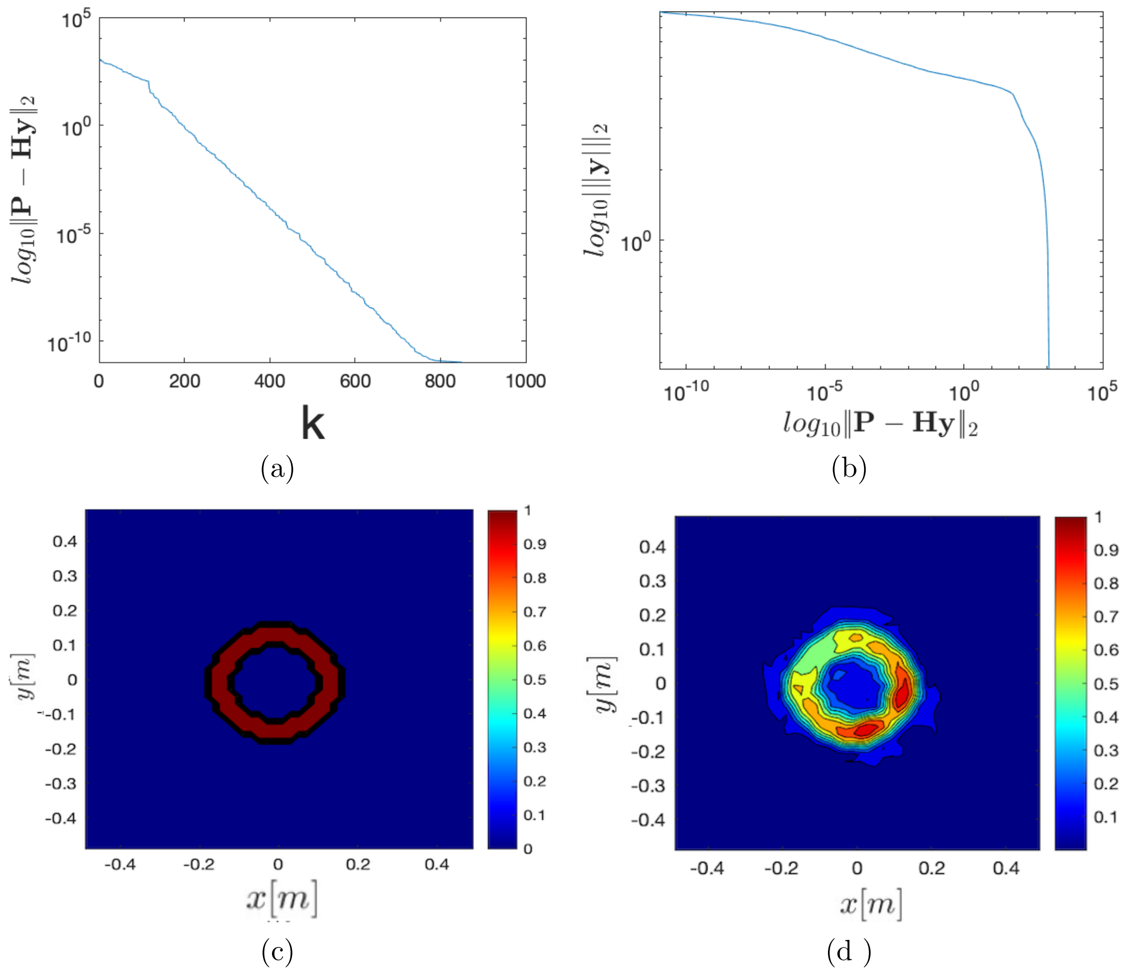

Figure 10: L-curve for the RIS-aided inversion problem(a-v). Each point on both curves is mapped to a unique value of k and a corresponding regularized albedo(d). Numerical validation: *TSVD*, SNR=50 [dB], Q=13×13, f_c = 5.825 GHz, 4 distinct scatterers) - Retrieved albedo when S=30 across single-channel.

Each truncation number k is associated with two plots. First, the Euclidean norm of the solution $\|\mathbf{y}\|_2$ is plotted against the logarithmic scaled residuals, as shown in Figure 10(b). Second, the residual norm $\|\mathbf{P} - \hat{\mathbf{P}}\|_2$ is plotted as the number of retained singular values increases. When plotting the first versus the second in a logarithmic frame, Figure 10(b), the resulting curve resembles a capital "L". The heuristic approach picks the truncation parameter corresponding to the inflection point. The k can also be spotted by plotting the logarithmic view of the residual norm as the truncation parameter increases. Hence, the algorithm is stopped whenever the solution reaches a reasonably convergent norm residual.

The inflection point can be readily and distinctly discerned in specific scenarios, yielding favorable outcomes. However, in some cases the knee choice might be challenging, particularly when solutions are influenced by the initial SVD components. This is one of the possible reasons why the TSVD in noisy environments and for poorly scattering profiles shows poor performance.

The L-curve approach exhibits outstanding results, which unfortunately comes at a very computationally heavy cost. The method chooses the truncation value after computing and storing all possible contributions to detect the curvature change to reconstruct the solution. The complexity related to the selection of the number of singular values to be retained is stacked on the already heavy SVD decomposition.

4.2 Regularization role

The regularization in imaging inversion problems has many extents and uses. The target occupies a small part of the region of interest in typical imaging or tomographic inversion challenges. This condition leads to pronounced sparsity for the forward matrix. In the L-curve method, the selection of the truncation parameter highly depends on the specific target and the rough visual intuition from the heuristic approach.

The super-resolution achieved by the TSVD is assessed by testing the algorithm with a simple four-scatterer target. According to the discussed geometry, the resolution from the RIS-aided RF imaging system abides by the cross-resolution definition. The number of cells per side Q=10 and the average slant range distance R$\approx$ 1 lead to an expected resolution of $\delta_x < 22cm$. The spatial sampling(i.e., inter-element spacing) for RIS cells relies on the Nyquist theorem extended to the spatial domain. In Figure 11, the simple '4-point' target produces an L-curve calling for a quite short k, as a direct result of the very sparse reflectivity function $f(x, y)$ for the region of interest.

The very high resolution is once again enhanced by the number of sub-carriers stacked to strengthen the **H** matrix amount of information. The lower the number of unitary pixels within the frame, the lower the rank of the subspace containing the inversion solution. This condition would require a tight truncation parameter. This means most information is lumped in a lower dimension of the solutions space.

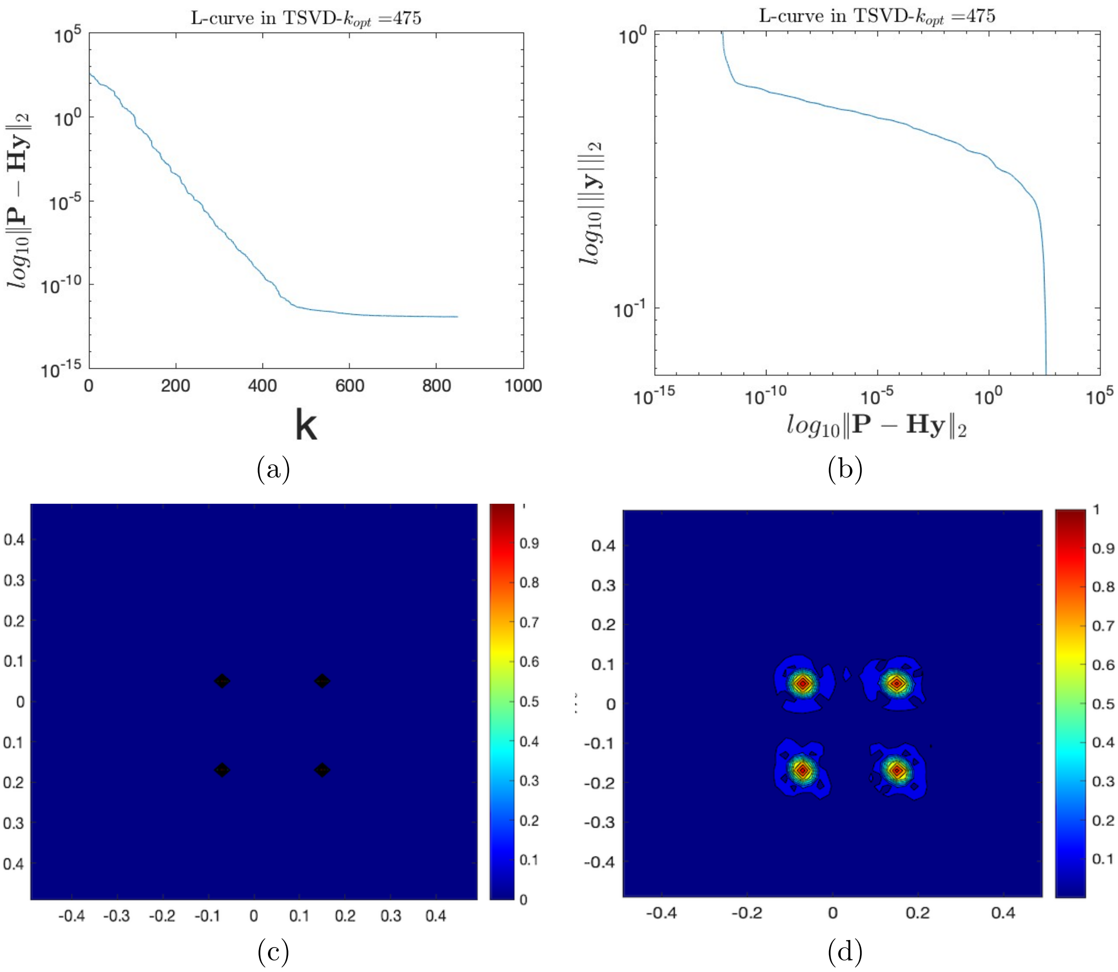

(a) (b) (c) (d)

Figure 11: Numerical Validation - ($TSVD$, SNR=50 [dB], Q=13×13, f_c = 5.825 GHz, 4 distinct scatterers) - Retrieved albedo when S=30 across single-channel.

An increase in the number of elements per RIS side enhances imaging by providing a more focused scan of the electrical field towards the ROI. This additional information strengthens the transport matrix and expands the solution space, leading to a higher regularization truncation number.

In direct methods, the solution is computed all at once, and the regularization has an instrumental effect on imaging quality. For the TSVD direct method, the regularization acts as a low-pass filter for low-frequency components of the image , especially when just a few among the first values are useful to determine the solution. The regularization term speeds up the convergence for those low-frequency components and increases the immunity to high-frequency noise.

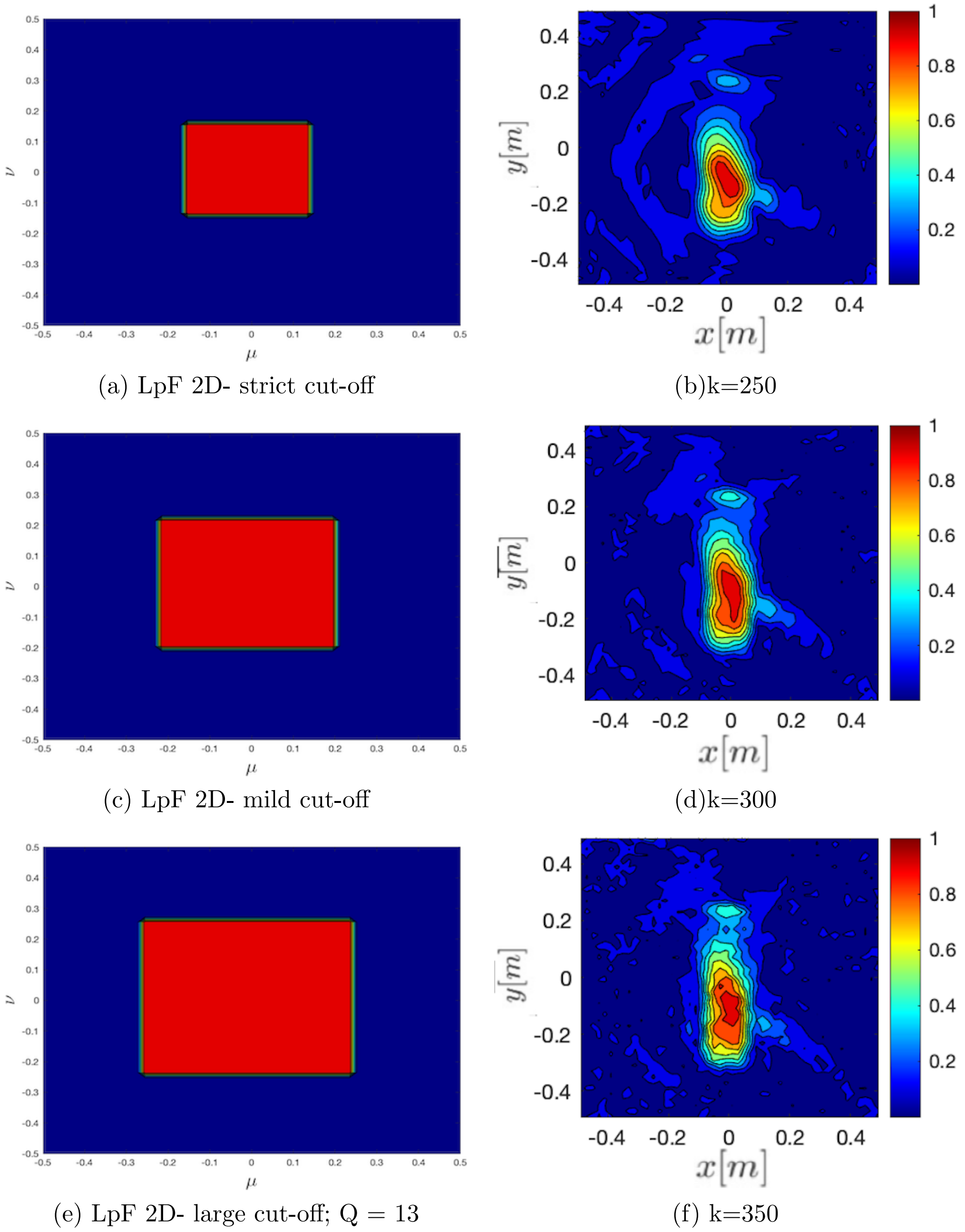

(a) LpF 2D- strict cut-off

(b)k=250

(c) LpF 2D- mild cut-off

(d)k=300

(e) LpF 2D- large cut-off; Q = 13

(f) k=350

Figure 12: Low-Pass spatial filtering effect of regularizing functions. Numerical Validation - (*TSVD*, SNR=50 [dB], Q=10×10, f_c = 5.825 GHz, S=1, 4 distinct scatterers) - Low-Pass spatial filtering effect of regularizing functions

In the frequency domain, a strict low-pass filter would improve the SNR while stretching the signal over time. In other words, the higher SNR would come at the cost of reduced bandwidth for the signal of interest. The regularization affects imaging quality in a similar manner.

As shown in figure Figure 12, higher k-truncation means milder filtering of the reconstructed solution. On one hand, the reconstructed image benefits from sharper edges since the low-pass effect is milder on higher-frequency components, visually associated with boundary steps. On the other hand, the solution collects more high-frequency noise, which in turn introduces many artifacts, deteriorating the image. A lower truncation acting as a strict low-pass filter rules out high-frequency noisy components to bring out useful information from the ROI. This strict filtering carries out the counter-effect of a blurry image out of the reconstruction and increases the tendency to overestimate local, lower-frequency artifacts.

The optimum lies in the middle of the two evils, and it depends upon the object, the propagation condition, and the desired resolution. Although being a direct method that inherently carries out high computational expenses, the imaging capabilities are of significant quality. The RIS-aided system is able to recreate the target images in a very detailed way with a good noise separation according to the heuristic choice of the truncation parameter. The main disadvantage of direct methods is the huge computational cost and storage demand. Each SVD decomposition involves three complex square matrices to be computed and stored concurrently. The complexity requirement for the sole TSVD algorithm is O(N^3). The step is then followed by an automatic truncation parameter selection leveraging the second derivative of the norm of the solution norm curve as plotted versus the residual in logarithmic scaling. Given the high complexity of the model as well as the huge memory usage of the TSVD direct method, iterative approaches deserve to be deeply investigated.

CHAPTER 5

ITERATIVE INVERSION ALGORITHMS

(Previously published as part of Tortoriello, C., Erricolo, D., and Oliveri, G.: Wave Manipulating RIS for Enhanced Tomographic Imaging: Concept and Recent Advances. In 2024 United States National Committee of URSI National Radio Science Meeting (USNC-URSI NRSM), pages 236–237, 2024)

When recovering a profile from a compressed multi-dimensional function (reflectivity profile), small measurement errors can be significantly amplified due to the condition number of the channel matrix. Regularization is a standard solution to address this issue. Additionally, leveraging prior knowledge about the target and environmental noise can improve algorithm convergence. In RIS-aided WiFi imaging, the transport matrix tends to be sparse. Reflections and direct fields from scattering centers far from the target tend to combine destructively. This effect is particularly evident in point detection applications, where profile sparseness further compresses the information carried by the matrix.

Direct methods are computationally expensive as they require the full matrix storage. Conversely, iterative techniques offer an appealing efficient alternative. These methods begin with an initial guess and progressively refine the solution through a series of local optimizations, gradually converging toward an optimum[28]. Each iteration builds on the previous step, guiding the search toward a better solution. In regard to ill-posed problems, the iterative algorithm aims to find a "satisfactory" solution by making minimally correlated updates to the current solution, ensuring each step introduces new information. In the most general Conjugate Gradient (CG) case, this concept is known as the "orthogonality principle".

From a mathematical perspective, the algorithm pushes the cost function $J(\mathbf{y_k})$ at step k in the direction opposite to the gradient, moving away from regions of maximum variation within the space of admissible solutions. This ensures that the value of the cost function does not increase with each iteration, ideally guiding the algorithm toward a local minimum. Iterative approaches offer two additional advantages. First, they allow the enforcement of a "hardbound" at each step based on the physics of the problem. This integration has been proven effective in Computed Tomography imaging, as demonstrated in previous works [27].

In our model, where the object occupies a small part of the targeted region and the discrete reflectivity function is binary, leveraging this domain can improve convergence. Second, iterative methods can include a "stop rule," serving as both a regularization term and a complexity cap. While inversion algorithms generally guarantee convergence with a sufficient number of measurements, computational costs can be reduced by terminating the process at a sub-optimal point that satisfies the desired reconstruction quality. Although the Conjugate Gradient method has proven effective in many CT problems [29; 30; 31], its convergence is not guaranteed if the orthogonality principle is compromised, making the exploration of alternative solutions worthwhile.

5.1 Algebraic Reconstruction Technique

The Algebraic Reconstruction Technique (ART) was pioneered by Polish mathematician Stefan Kaczmarz in 1937 as a solution for linear systems of equations. Despite its early development, its utilization remained limited due to the lack of powerful computing resources until the 1970s. However, ART was rediscovered and gained significance with the advancement of technology, particularly in the field of X-ray tomography[32]. Recently, the Algebraic Reconstruction Technique (ART) [33] has demonstrated effectiveness in Computed Tomography (CT) imaging, since it does not explicitly rely on the orthogonality of updates from the solution [27] as the Conjugate Gradient or similar approaches do.

This imaging problem is an intriguing deconvolution challenge. The multidimensional function of interest (reflectivity function) is convoluted with a transport matrix(CSI). The result is projected on a lower dimensional space(1D vector of measures). Each equation, corresponding to a phase configuration, defines a hyperplane within this space. The iterative approach projects the initial guess onto the first hyperplane, and successive projections(not necessarily orthogonal) take the algorithm incrementally closer to a valid solution. The convergence of the algorithm can be accelerated by imposing a *hard bound* on the solution, guiding the direction of the iterative updates. However, if the updates are not carefully chosen, they may introduce inadequate information and correlation, leading to poor convergence and reduced imaging quality.

For example, constraining a complex solution to the actual domain can cause the solution to align with iterative updates, requiring a re-orthogonalization process, which is often impractical for large-scale problems. Additionally, since each hyperplane represents a distinct ray integral, adjacent ray integrals will likely be nearly parallel. The ART method operates on the principle of computing the pseudo-inverse in a double-iterative manner. At first, starting from an initial guess, the algorithm performs a scan throughout the rows of the $\mathbf{H}$ matrix [34]

$$\mathbf{H}_i^{\dagger} = \mathbf{H}_i^{H}(\mathbf{H_i} \cdot \mathbf{H_i^H})^{-1} = \mathbf{H}_i^{H}(\|\mathbf{H_i}\|_2^2)^{-1} = \frac{\mathbf{H}_i^{H}}{\|\mathbf{H_i}\|_2^2} \tag{5.1}$$

This inner cycle is aimed to produce an image with a step-by-step update. Each row $\mathbf{H}_i$ is associated with a complex scalar measure $\mathbf{p}_i$. The i_{th} internal iteration defines the updated solution as

$$\mathbf{y}_{i+1} = \mathbf{y}_i + \mu \cdot \frac{\mathbf{H}_{i+1}}{\|\mathbf{H}_{i+1}\|_2^2} \cdot (\mathbf{p_{i+1}} - \langle(\mathbf{H}_{i+1})^T, \mathbf{y}_i\rangle) \tag{5.2}$$

The core principle is to ensure that each action minimally depends on the previous steps within the sequence of iterative updates. The ART algorithms have a simple, intuitive basis. Each projected density is mapped back into the higher-dimensional space from which it originated, with iterative adjustments to align each estimated projection with the corresponding measured projection.

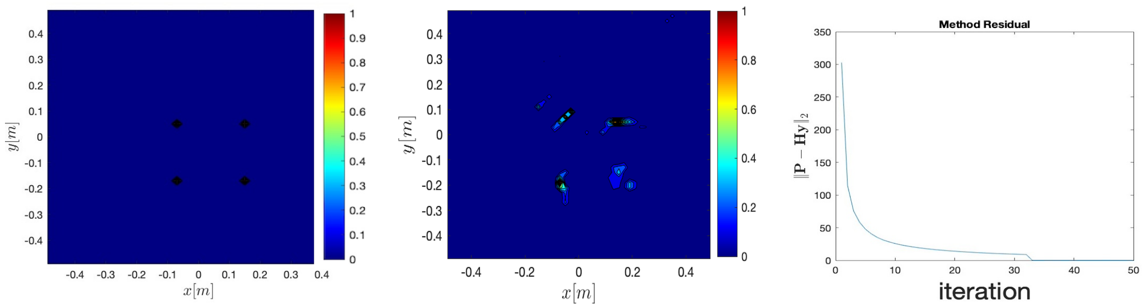

(a) Ground Truth (b) Unconstrained ART (c) Convergence

Figure 13: Numerical Validation - (*Unconstrained ART*, SNR=50 [dB], Q=10, S= 51 extended over 3 channels $f_c = 5.825$ GHz, b=1, I-shaped profile)

In practice, RIS configurations for adjacent scatterers are often highly correlated, largely due to the discrete phase shift capabilities(parallel hyperplane). The goal is to keep successive updates as orthogonal as possible to the subspace spanned by the vectors previously used. Previous research has investigated reordering equations to minimize the correlation between successive steps, a strategy that has been tested and validated under specific conditions [35]. A simpler approach, initially proposed in [36], is to strategically select the order in which the hyperplanes are considered.

On a theoretical basis, this approach favours orthogonality between successive updates, as the algorithm applies the most effective uncorrelation scheme between rows. However, the results have not demonstrated a substantial improvement in this regard. Theoretically, two loops can be distinguished. The inner loop processes the majority of the rows. To enhance computational efficiency, this inner loop can be terminated based on a heuristic threshold. In other words, applying a stop rule to the inner loop further improves convergence. The outer loop uses the inner loop updated image $\mathbf{y_{new}}$ as the starting point for another pass through the following cycle. After each full inner cycle, the ART evaluates the norm of the residual between the noisy measurements and the current solution:

$$\mathbf{r_m} = \|\mathbf{P} - \mathbf{H} \cdot \mathbf{y_{new}}\|_2. \tag{5.3}$$

This residual is used to check whether the solution has reached a stable state. When the updated residual falls below a set percentage of the previous iteration (within a defined tolerance), the algorithm considers the solution acceptable.This approach, based on the discrepancy principle, aims to limit the number of iterations and prevent the system from cycling and stagnating around a point due to the ovality of the solution. Compared to the standard pseudo-inverse method, ART offers two key advantages. First, ART allows for a regularized solution. Second, each inner iteration requires significantly less computational effort, despite both methods aiming for the same practical outcome.

5.1.1 Regularization Role

The Regularization plays a crucial role in inversion problems. The type, the shape and the way the problem is regularized can impact speed of convergence, stability and imaging performance. ART incorporates regularization through two mechanisms. First, the μ relaxation parameter serves as a fine-tuner for regularization. Second, the integration of a stop rule can improve performance based on a-priori knowledge of the physical properties of the system.

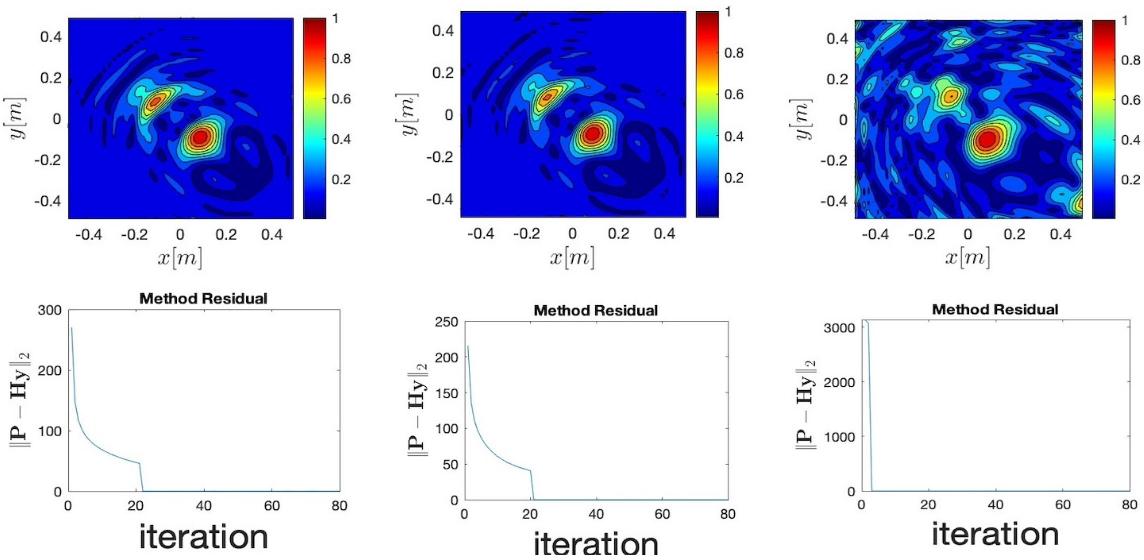

(a) $\mu = 0.4$ (b) $\mu = 1$ (c) $\mu = 2$

Figure 14: Numerical Validation - (*Unconstrained; uninitialized ART*, SNR=50 [dB], Q=13, S= 51 extended over 3 channels $f_c = 5.825$ GHz, b=1, O-shaped target)

The μ is the counterpart of the truncation parameter from the TSVD examined in Chapter 4. This weighting term for the update is adimensional thanks to the normalization of the update term. The parameter variation range has been discussed in previous works [37]. However, due to the dependence of the algorithm on specific conditions and the underlying physics of the application, only a general range of 0 to 2 can be provided. Figure 14 shows the comparison among different μ selected for the reconstruction. Similarly to the truncation coefficient from TSVD, the relaxation parameter can tune the degree of regularization according to the desired convergence speed and quality for the solution. The O-shaped metallic target is imaged with the 51 frequency samples spread over a 3 channels 40-MHz each to improve the spatial variety needed(See 2). The μ= 0.4 shows how the smaller regularization limits the spatial frequency components and leaves the floor to low frequency ones.

The other extreme of the regularization μ= 2 aims at including higher frequencies within the reconstruction. Again, this would improve the edge detection in the case of a good problem conditioning. For the nature of the reconstruction problem this value also incorporates high-frequency noise that overwhelms the target reconstruction. Additionally, the iterative algorithm slightly slows down due to the effect of milder step in projections of hyperplanes. The second effect carried out by the stop rule can be intuitively already seen from the previous discussion. A set of projections of a partial solution bounce back and forth around a point. On one hand the algorithm approaches the most reliable solution. On the other hand the computational expense increases andf additional noise is progresasively injected into the solution

5.1.2 Effect of initialization

As shown in Figure 13 the plain version of the ART algorithm exhibits a poor imaging resolution. We can use some workarounds to get the best out of ART. First, the initial step in iterative image reconstruction methods involves a crucial decision: *how to initialize the process.* Kaufman[38] has contended that opting for a uniform image is the most rational starting point.

This choice is since any features present in the initial image will persist for a significant duration throughout subsequent iterations, thereby influencing the overall trajectory of the algorithm.

An appropriate value for this guess image can be set by estimating the average activity within the image data and assigning it to initial solution components[35]. According to how the system is designed, the lexicographic measures vector likely represents a blurry and shaded version of the target. The starting point is then selected as

$$\mathbf{y}_0 = \frac{|\mathbf{P}|}{\max(|\mathbf{P}|)} \tag{5.4}$$

which is also referred to as the mean density of the object

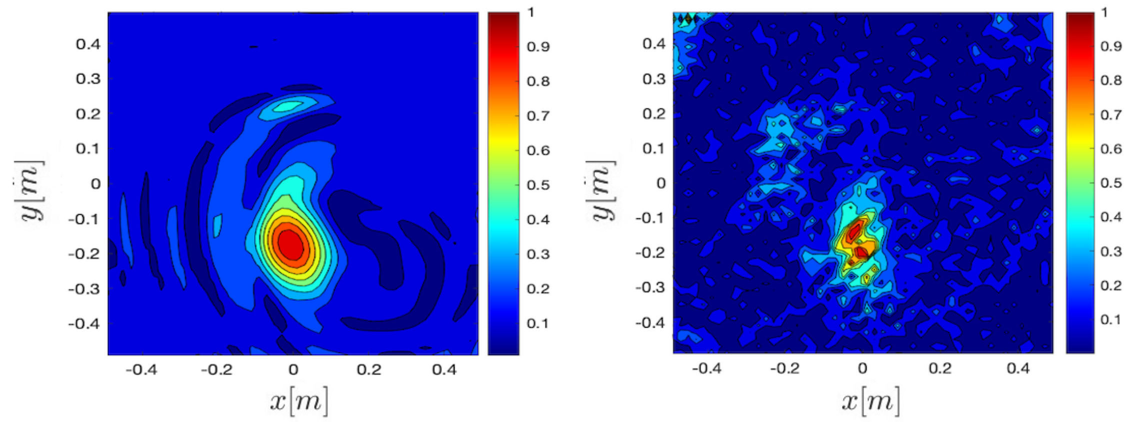

(a) Uninitialized ART

(b) Initial guess effect

Figure 15: RIS-aided detection system, initial guess effect. Numerical Validation - (*Initialized, Unconstrained ART*, SNR=50 [dB], Q=13 f_c = 5.825 GHz, b=1, I-shaped profile)

The Figure 15 shows the significant improvement carried out by a change in the initial guess for the iterative searching method. The shaded and deformed figure turns into a lumped and slightly sharper one.

5.1.3 Effect of physical bound on Noiseless Imaging

The second advantage of iterative approaches involves applying bounds to the solution based on permissible and reasonable values. These bounds can be applied in two ways, starting from the albedo constrained to the real range [0,1]. Unfortunately, any direct algorithm works on optimization through a complex bundle $\mathbf{P} = \mathbf{H} \cdot \mathbf{y}_k$ that makes the complex CSI part and purely real one of the albedo non-resolvable.

In the ART iterative approach, both inner and outer cycle scanning provide a complex partial solution that can be forced as real and constrained according to the physiscs of the problem. The Figure 16 compares two simple hardbound constraints applied to the solution. In Figure 16(a), the magnitude of the partial solution is normalized by the maximum

$$\mathbf{y_k} = \frac{|\mathbf{y_k}|}{\max |\mathbf{y_k}|} \tag{5.5}$$

In Figure 16(b), the bound constraints the more significant *real* part of the solution, saturating values out of [0,1] range, in particular, whenever $\mathbf{y}_i > 1$ the value is constrained to 1.

The reconstruction quality is much higher in this second case as the effective conditions of the physical system are more accurate, leading the iterations through the solution faster and more effectively.

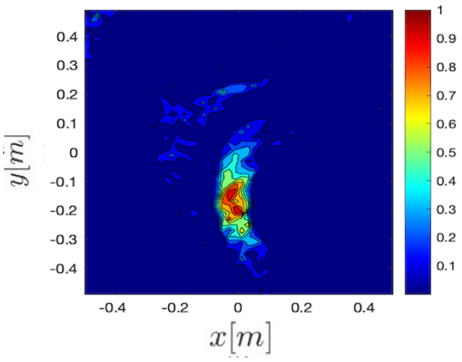

(a) Simple bound

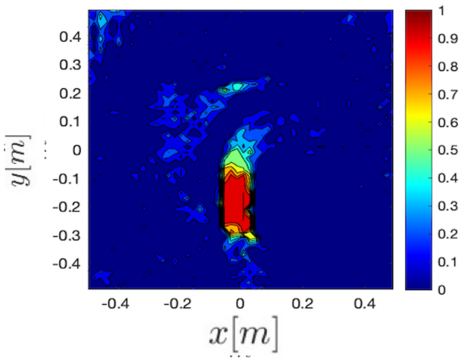

(b) Physics-based bound

Figure 16: Comparison of different physical bounds to the solution: magnitude of the solution(a) versus the physics-based bound with the real part constrained in real domain of interest [0,1](b).

The ART imaging modified with meaningful initial guess combined with a proper physical bound limit can effectively reconstruct a fair portion of the whole target continuously. Nevertheless, this iterative method is not able to recover targets with a complex reflectivity profile.

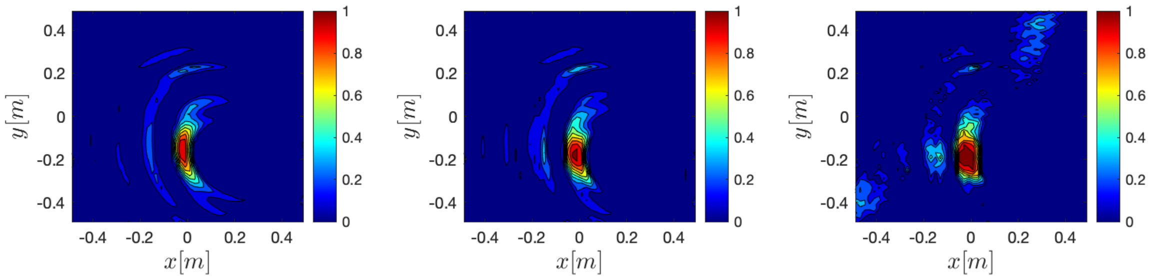

(a) I-profile; Q = 10 (b) I-profile; Q = 13 (c) I-profile; Q = 17

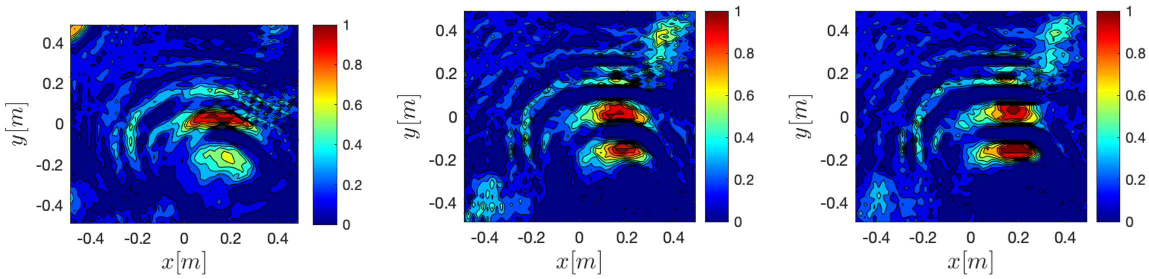

(a) E-profile; Q = 10 (b) E-profile; Q = 13 (c) E-profile; Q = 17

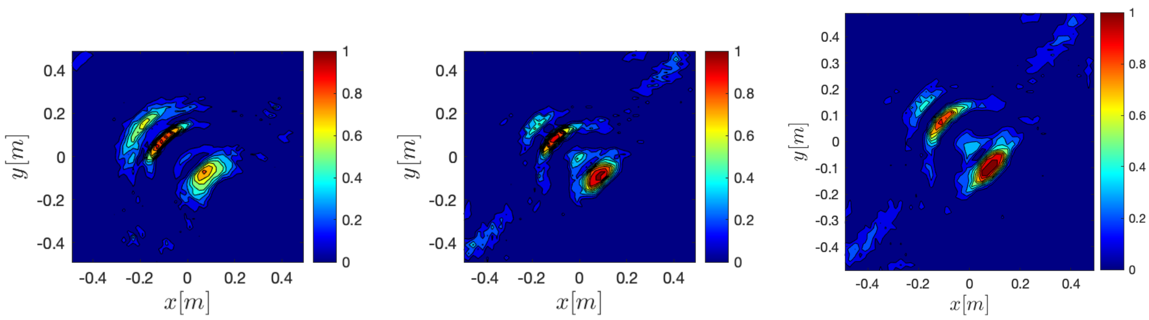

(a) O-profile; Q = 10 (b) O-profile; Q = 13 (c) O-profile; Q = 17

Figure 17: Numerical validation of *ART*, SNR=50 [dB], Q=variable, $f_c = 5.825$ GHz, 4 distinct scatterers) - Retrieved albedo when S=50 in wide spectrum configuration.

5.1.4 ART convergence

A few comments on the ART convergence are needed here. This final paragraph of the chapter is meant to justify why the current implementation is not satisfying, calling for a different method. ART reconstructions often suffer from salt and pepper noise, caused by inconsistencies introduced by the approximations typically used for W_{ik} [2]. This results in computed ray-sums that are poor approximations of the measured ray-sums. The problem is compounded by the fact that each equation corresponding to a ray in a projection alters some pixels that were just modified by the preceding equation in the same projection. Although relaxation parameters in ART can mitigate some of this noise, the improvements in reconstruction quality usually come at the cost of slower convergence and are not significantly impacting our analysis.

A potential cause for the lack of convergence could be the expansion of the reflectivity function. Alternative algebraic reconstruction techniques, such as Simultaneous Algebraic Reconstruction Technique (SART) and Simultaneous Iterative Reconstruction Technique (SIRT), use an expansion function basis of higher order than the square pixelization employed here. In particular, a bilinear basis function might provide a more pyramidal shape for the reflectivity function, potentially improving imaging effectiveness. In ART methods, knowing the ray paths connecting transmitter and receiver positions is crucial. However, predicting these ray paths becomes challenging when refraction and diffraction effects are significant compared to the average background. Applying algebraic techniques under such conditions often yields unreliable results.

Conversely, when refraction and diffraction effects are minimal (less than 2-3% of the average background value), it may be feasible to combine algebraic methods with digital ray tracing techniques. Investigating new iterative approaches could provide a better and deeper understanding of these challenges.

5.2 Super-resolution Algorithm for Sparse Problem with Majorization-Minimization (SMM)

As observed, the sparsity and low rank of the system lead to iterative methods to reduce computational burden while boosting performance working on the useful dimension of the space of solutions. Such a strongly ill-posed problem can benefit from regularization in terms of stability and imaging quality. Recent studies have proposed various penalty functions tailored to different priors, including Lp, total variation (TV), and low rank (LK) [39]. In the context of sparse super-resolution problems, the L_p norm with $0 \leq p \leq 1$ is commonly employed as a penalty function as specified in 5. The L_1 regularization is convenient because provides a convex expression where small and big residuals are equally important. Unfortunately, it is not differentiable, and it is significantly harder to find a solution in an iterative fashion. The workaround to smooth the L_1-norm cusp is to use a quadratic function to approximate the original objective via a Maximization-Minimization approach[40]. At each step, this new method determines a polynomial upper bound for the cost function solution. The *majorizer* is set according to three conditions. At first, the majorizer is obviously set greater or equal to the objective for each step

$$G(\mathbf{y}|\mathbf{y}^k) \geq J(\mathbf{y}) \tag{5.6}$$

Second, the polynomial upper function and the original cost function have to be equal to each other in $\mathbf{y^k}$. The majorizer is chosen so that [40]

$$G(\mathbf{y^k}|\mathbf{y^k}) = J(\mathbf{y^k}) \tag{5.7}$$

Third, the partial iterative solution is obtained as

$$\mathbf{y}^{k+1} = \min_{\mathbf{y}} \left\{ G(\mathbf{y}|\mathbf{y}^k) \right\} \tag{5.8}$$

This iterative solution is ensured to be monotonically decreasing, making the algorithm converge to a solution.

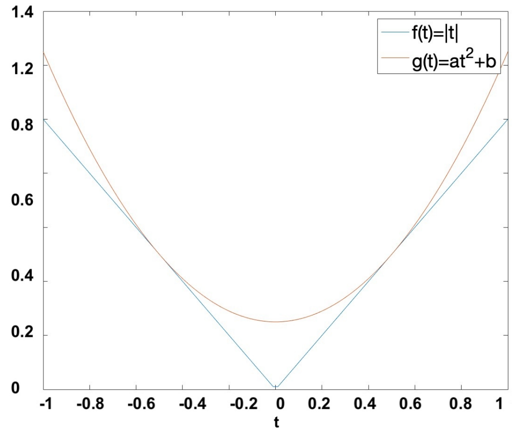

Figure 18: Quadratic Majorizer $g(t)$ of a linear function $f(t)$

The part is crucial to select the specific upper bound function concerning $J(\mathbf{y})$. A quadratic function is the best option because of the L_1-norm extending the 1D concept of absolute value $f(t) = |t|$. Such function can be chosen as

$$g(t) = \frac{1}{2\|t^k\|}t^2 + \frac{1}{2}\|t^k\| \geq |t| \tag{5.9}$$

Replacing t with the k_{th} sum of reflection coefficients of the scatterers, one can get[41]

$$\sum_n \left[\frac{1}{2|\mathbf{y}^k(n)|}v^2(n) + \frac{1}{2}|\mathbf{y}^k(n)|\right] \geq \sum_n \mathbf{y}(n) \tag{5.10}$$

The final quadratic function replacing the L_1 norm is

$$\xi(\mathbf{y}^k) = \frac{1}{2}\mathbf{y}^T \Lambda_k \mathbf{y} + \frac{1}{2}\|\mathbf{y}^k(n)\|_1 \tag{5.11}$$

where $\Lambda_k = diag(\frac{1}{|\mathbf{y}^k|})$. The new quadratic function in (Equation 5.11) contains a constant term that can be ruled out over time. The regularization term will be tuned according to a scalar parameter varying on a small scale to improve algorithm stability. This conventional MM algorithm leads to a *Lasso regularization* for cost function, resulting in

$$J(\mathbf{y}) = \frac{1}{2}\|\mathbf{H} \cdot \mathbf{y} - P\|_2^2 + \mu\|\mathbf{y}\|_1 \tag{5.12}$$

The function minimization is now easier to be solved iteratively thanks to the second-order, smoother shape. After ruling out the constant factor in Equation 5.11, the step solution is set as

$$\mathbf{y}^{k+1} = (\mathbf{H}^H \cdot \mathbf{H} + \Lambda_k)^{-1}(\mathbf{H}^H P) \tag{5.13}$$

Although our inversion problem involves a total of 2500 elements, the iterative approach can efficiently leverage the a-priori knowledge about the low-rank using the *sparse* diagonal Λ_k. The update brought by this work refers to the diagonal matrix based on the current solution. The main problem is that sparse solutions(i.e., point detection or quasi-zero elements) increase the number of low singular values for the sparse matrix Λ_k, which in turn increases the *conditioning number* and instability. A trivial approach is to add more regularization and initialize the diagonal matrix Λ_k with an identity matrix. This would come at the cost of increasing the bias from the correct solution due to a heavy regularization. A smarter workaround chooses the initial guess as different from the *null* solution, usually a gray image. Then, all the small values from the k_{th} solution are forced to saturate to 1 to ensure that the solution never approaches the singularity,.

5.3 Regularization role and noisy point detection

For the Majorization-Minimization approach the regularization effect comes into play as a game-changer. Once again the regularization gives robustness and solidity to the solution we are looking for. In iterative process, the smoothing penalty function prevents the over-fitting of the model to the data. For the specific iterative scenario, the solution is reached step-by-step making use of prior conditions to ease the convergence. By imposing hard bound from the albedo physical meaning, the learning curve would progress much faster. The albedo binary property confines the values of the discrete reflectivity profile to the (0,1) real domain for the partial solution. The regularization procedure has two main outcomes.

First, the imaging quality changes according to how strictly the L_1 norm penalty function is applied to the albedo. The μ regularization parameter rules how tightly the norm 1 $\|\cdot\|_1$ condition acts on the objective and determines the imaging performance. On the one hand, higher μ applies a tight two-dimensional *spatial* low-pass filter to the resulting image. Conversely, an easy frequency constraint lends a sharp and better-looking image with clearer edge detection as high-frequency components pass undisturbed. This comes at the cost of a system that is more sensitive to high-frequency noisy components.

Second, the regularization tunes the stability of the solution. From a different perspective, the (Equation 5.13) clearly shows that the μ applied in the form of a diagonal loading to the original *normal equation* helps the invertibility of the otherwise singular matrix $(\mathbf{H} \cdot \mathbf{H}^H)$.

A weak regularization leads to a fine and accurate solution but it carries out poor stability, which makes the solution far more sensitive to external additional noise. A firm regularization improves the stability of the solution and possibly speeds up the algorithm convergence at the cost of increasing the bias from the optimal solution.

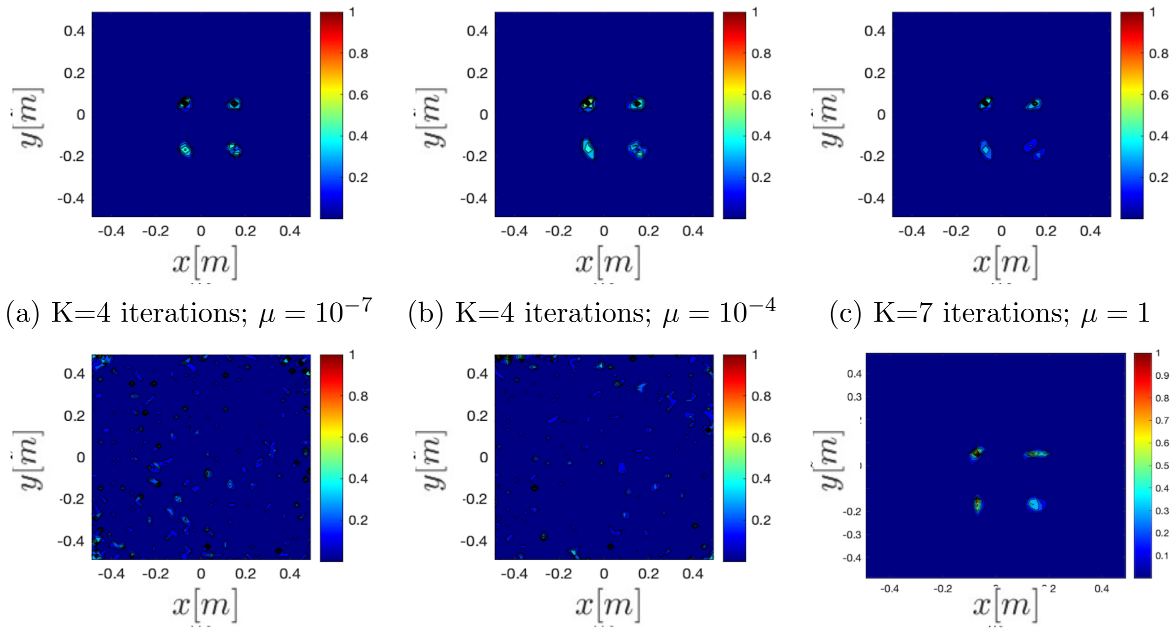

(a) K=4 iterations; $\mu = 10^{-7}$ (b) K=4 iterations; $\mu = 10^{-4}$ (c) K=7 iterations; $\mu = 1$

(d) K=4 iterations; $\mu = 10^{-7}$ (e) K=4 iterations; $\mu = 10^{-4}$ (f) K=4 iterations; $\mu = 1$

Figure 19: *SMM*, SNR=50 [dB](a-c) versus SNR=50 [dB](d-f), Q=10×10, $f_c = 5.825$ GHz, 4 distinct scatterers) - Retrieved albedo when S=30 across single-channel.

This trade-off can be verified by comparing the performance of the noiseless scenario to the noisy one from Figure 19. For the noiseless case(a-c), the parameter can be set as low as $\mu = 10^{-7}$, leading to the fastest convergence thanks to the implemented stop-rule, carrying out the best super-resolution detection. In the noiseless case, it appears that lower regularization yields better results. However, the noisy scenario set with an SNR=-10dB sharply highlights the critical point: the Sparse MM algorithm with the heaviest regularization is the only one able to achieve a great detection resolution, standing above the noise component. More importantly, a smaller μ leads the normal equation to significant instability, forcing the system to work under single-precision, unstable conditions.

5.4 Physical bound effect on Noiseless Imaging

The Sparse Majorization-Minimization approach was born to address the ill-posed problem of point-like target detection [41]. As highlighted in Chapter 5, the research for the L_1 norm penalty is particularly effective with strong sparsity patterns. Conversely, complex-shaped targets are seen more like a set of adjacent points than a continuous and integral figure. As shown in Figure 20, the reconstruction basically results in a 'point-wise' image and can display relevant images just as long as the noise from the environment is kept at a minimum.

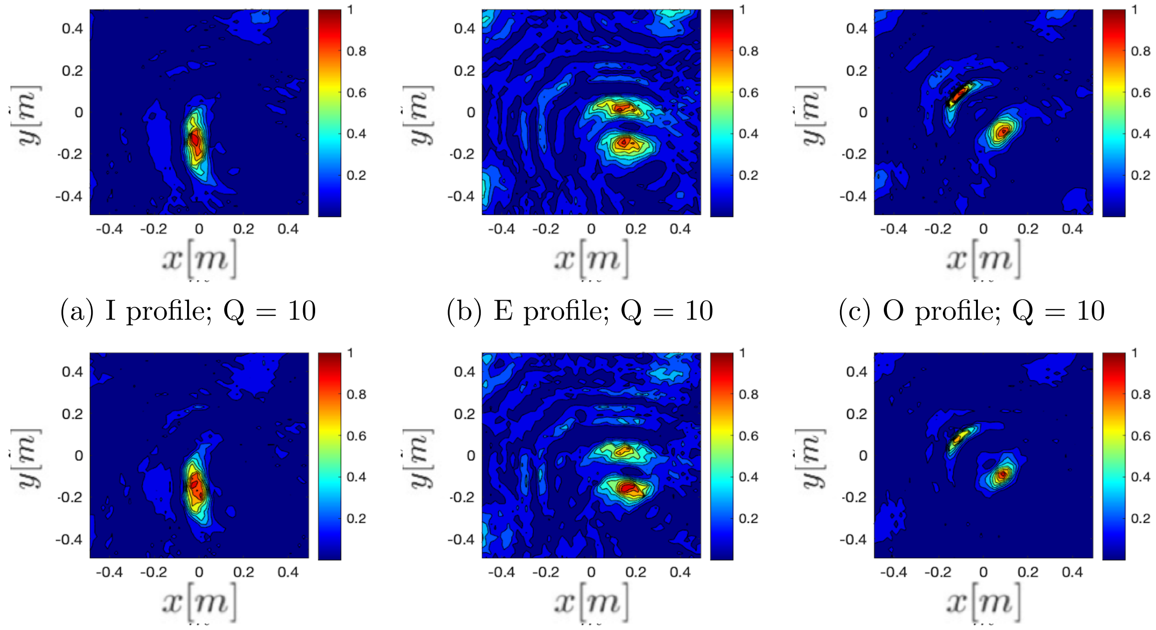

(a) I profile; Q = 10 (b) E profile; Q = 10 (c) O profile; Q = 10

(d) I profile; Q = 13 (e) E profile; Q = 13 (f) O profile; Q = 13

Figure 20: *SMM unconstrained*, SNR=50 [dB], Q=variable, $f_c = 5.825$ GHz, letters profile) - Retrieved albedo when S=30 across single-channel.K $= 15$; $\mu = 10^{-6}$.

Nevertheless, the use of physically bound for the iterative algorithm can impressively boost imaging performance in a noiseless condition, even with complex-shaped targets. For this aim, the Sparse MM has been evaluated with the same hard bound already discussed for the ART method in Chapter5. The testing environment is still kept to the simplest configuration, with the information merely coming from 30 sub-carriers stacked together. The interesting outcome is that the iterative method can now reach an outstanding reconstruction quality with very few iterations at lower hardware costs than the requirements in reference work [8]. The use of a hardbound lends sharpness to the imaging result and gives continuity to the reconstruction at the sole cost of slowing down the convergence.

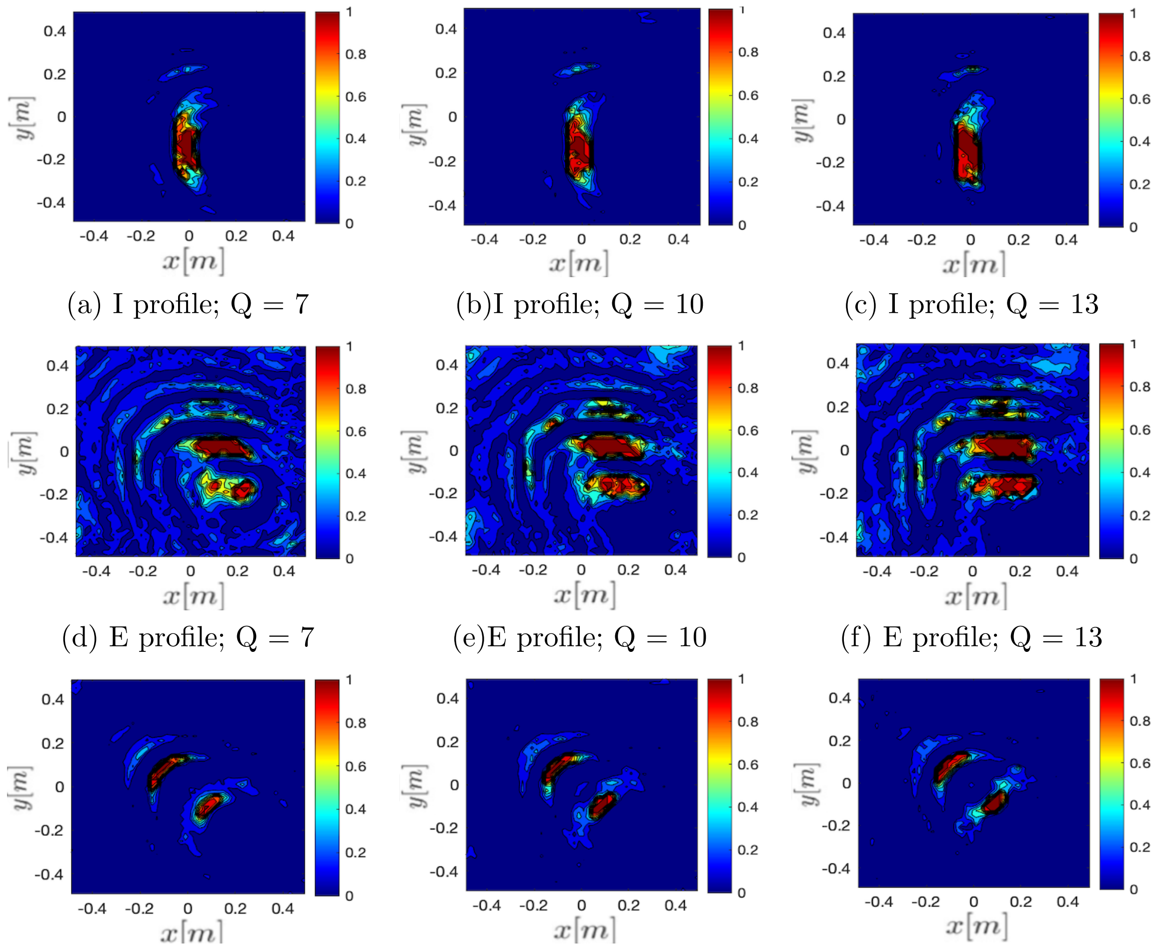

(a) I profile; Q = 7 (b)I profile; Q = 10 (c) I profile; Q = 13

(d) E profile; Q = 7 (e)E profile; Q = 10 (f) E profile; Q = 13

(g) O profile; Q = 13 (h) O profile; Q = 13 (i) O profile; Q = 13

Figure 21: *SMM constrained*, SNR=50 [dB], Q=variable, $f_c = 5.825$ GHz, letters profile) - Retrieved albedo when S=30 across single-channel.K = 15; $\mu = 10^{-6}$.

The results displayed in Figure 21 have been obtained with the same regularization factor used for Figure 20, with iterations increasing from 6 to 15. The WiFi imaging system equipped with a 13x13 RIS imaging already achieves high-resolution quality in cutting-edge algorithms[8]. For the latter case, the RMSE changes from an average of about 0.4, related to the "point-wise approximation," to an average of 0.24. The SSIM, which is a more structural-based metric, moves from a median of 0.04 to about 0.71, highlighting the substantial improvement. The significant improvement is achieved at a lower computational The system is able to achieve a super-resolution with O(K×M), where K are the few iterations required for the convergence.

CHAPTER 6

SYSTEM DESCRIPTORS

(Previously published as part of Tortoriello, C., Erricolo, D., and Oliveri, G.: Wave Manipulating RIS for Enhanced Tomographic Imaging: Concept and Recent Advances. In 2024 United States National Committee of URSI National Radio Science Meeting (USNC-URSI NRSM), pages 236–237, 2024)

This chapter expands over the theoretical discussions presented in Chapter 2 and Chapter 3. The RIS-aided system operates under a set of theoretical assumptions that combine principles from forward-looking Synthetic Aperture Radar (SAR) systems and techniques used in Computed Tomography (CT). The main descriptors of the system are presented and analyzed to ensure consistency between the obtained results and the predictions of electromagnetic theory. In particular, the focus is on how these parameters influence both the resolution and overall complexity of the imaging process. The analysis examines how the system behaves under different parameter settings. Key performance metrics such as signal-to-noise ratio (SNR) and phase shift control also come into play. Imaging quality is assessed based on three primary factors: resolution, contrast, and noise levels. Additionally, the influence of each descriptor on the computational burden of the system is investigated. Understanding how these parameters interact will allow for better optimization of the system design and performance, making it more applicable in real-world scenarios.

6.1 Evaluation metrics

The perceptual assessment of the quality of the inversion algorithm may be misleading.

From now on, both the albedo vector is denoted as $\mathbf{a} \in \mathbb{R}^{M_{target} \times 1}$ to distinguish it from Cartesian coordinates. According to the model describing the reflective properties of the imaged object, the reconstruction is directly compared against the reference value. The quality of the inversion is estimated using two convenient evaluation criteria.

First, the Root Mean Square Error (RMSE) accounts for deviation in a quadratic way, highlighting the actual inaccuracy rather than the sign of such a difference. The intuitive error evaluation would consider the absolute difference between the reference frame and the reconstructed one. However, the sign compensation in such an absolute error evaluation is a source of inaccuracy affecting the residual for quality assessment.

To avoid such a misleading effect, the standard deviation of the residual error $\epsilon = (\mathbf{a}_{\mathrm{gnd}} - \mathbf{a}_{\mathrm{rec}})$ reasonably defines how far the image is from the expected value on average. Since the error is logically expressed in the same unit as the quantity under evaluation, the square root of the variance is taken. The RMSE is defined as

$$RMSE = \sqrt{\frac{\sum_{i=1}^{M_{target}} (a_{i,gnd} - a_{i,inversion})^2}{M_{target}}} \tag{6.1}$$

The higher the RMSE, the more the output is "dispersed" about the final solution. The importance of this figure of merit comes from the analogous difference between accuracy and precision.

If we think of the ballistic skills of an archer, they are not only given by the ability to reach the center of the target(accuracy). The skills also consider how closely (on average) the shots are between each other. Similarly, the reconstruction is accurate when the results are (on average) close to the ground truth. The imaging system is precise when providing similar results with the same original reference. The precision prescribes how often the reconstruction set converges somewhat to the same result, not necessarily to the ground truth itself. It is important to stress that the reconstructed albedo will differ from the ground truth as an intrinsic property of minimum residual algorithms. Although the RMSE offers a fair and helpful tool to evaluate the reconstruction quality, it does not give a general and vivid idea of the structural similarity between the images. The two profiles are bi-dimensional matrices. The more exhaustive comparison between the two images accounts for the structural similarities[42].
The highest-fidelity comparison involves the Structural Similarity (SSIM) index measure. Unlike the majority of previously introduced techniques, SSIM evaluates the structural bi-dimensional similarity among images.

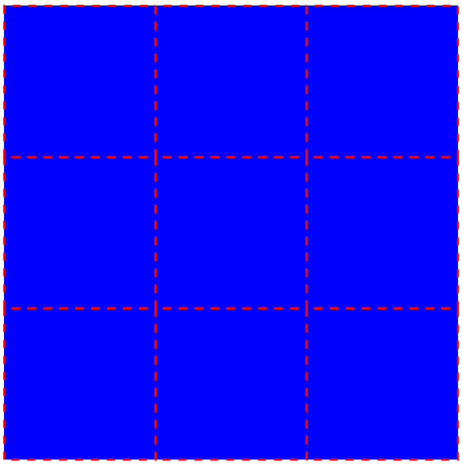

Figure 22: Example of image partitioning for assessment of SSIM index. Each square is characterized by a bi-dimensional statistics σ_x,σ_y,σ_{xy}

The similarity is evaluated, partitioning the overall domain in 2D patches to assess local similarity. This approach looks more reasonable than the point-wise error, as inter-channels and intra-channels correlation cannot always be assumed negligible, especially in intricate patterns. The similarity function is locally defined rather than globally for a few reasons.

First, images are usually likely to be spatially nonstationary, recalling the spatial frequency intuition from Chapter 4. Second, distortions are usually space-variant. A localized quality measurement is more capable of providing a spatially varying quality map of the image, which delivers more information about the quality degradation of the image. The similarity index is a function defined as

$$S(\mathbf{x}, \mathbf{y}) = f(l(\mathbf{x}, \mathbf{y}) \cdot c(\mathbf{x}, \mathbf{y}) \cdot s(\mathbf{x}, \mathbf{y})) \tag{6.2}$$

where the pair (x,y) refers to the discrete domain coordinates of the pixel in the image. For the local evaluation, the picture is partitioned in many patches of size N $\times$ N, with N = 50. The empirical average is defined as

$$\mu_x = \frac{1}{N}\sum_{i=1}^{N} x_i; \quad \mu_y = \frac{1}{N}\sum_{i=1}^{N} y_i \tag{6.3}$$

The first space function to construct the index is the *luminance* defined as the quantity assessing the amount of light/intensity sketched in the image. It is mathematically defined as

$$l(\mathbf{x},\mathbf{y}) = \frac{2\mu_x\mu_y + C_1}{\mu_x^2 + \mu_y^2 + C_1} \tag{6.4}$$

with $C_1 = (K1 \cdot D)^2$ constant to avoid instability and defined according to the dynamic range of the image(255 for 8-bit grayscale images). Whenever the means approach the zero values, the C_1 constrains the luminance to unity. The dynamic range indicates the capability of an imaging system to detect bright and shadowed areas. The wider the difference, the larger the range, and the higher the white-to-black differentiation.

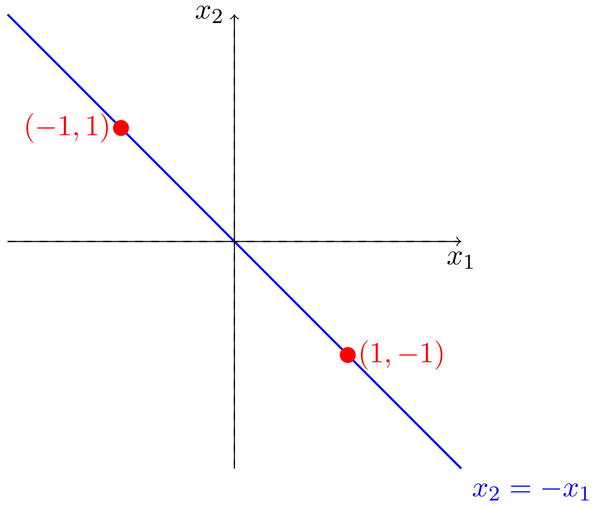

Figure 23: Hyperplane of projection to remove the bias from the data

The second quantity of interest is the *contrast*. In both directions, the image vectors are projected onto the hyperplane

$$\sum_{i=1}^{N} x_i; \tag{6.5}$$

As shown in the picture, this corresponds to removing the average from both vectors. The corresponding standard deviation for each patch is easily set

$$\sigma_x = \sqrt{\frac{1}{N-1}\sum_{i=1}^{N}(x_i-\mu_x)^2}; \quad \sigma_y = \sqrt{\frac{1}{N-1}\sum_{i=1}^{N}(y_i-\mu_y)^2} \tag{6.6}$$

Finally the contrast of the object is defined as

$$c(\mathbf{x},\mathbf{y}) = \frac{2\sigma_x\sigma_y + C_2}{\sigma_x^2 + \sigma_y^2 + C_2} \tag{6.7}$$

with $C_2 = (K2 \cdot L)^2$ constant used for same reason as in C_1. The geometrical correlation of the normalized contrast structural function $\sigma_{x,y}$ is defined as

$$\sigma_x = \sqrt{\frac{1}{N-1}\sum_{i=1}^{N}(x_i - \mu_x)(y_i - \mu_y)}; \tag{6.8}$$

It is interesting to notice that the *contrast* depends not only on the variances mismatch but also on their actual values. The final similarity function is the *structure*. This is evaluated as a normalization of the standard variations of the two compared signals

$$s(\mathbf{x},\mathbf{y}) = \frac{\sigma_{x,y} + C_3}{\sigma_x \cdot \sigma_y + C_3} \tag{6.9}$$

The three constants C_1, C_2, C_3 are regularizing parameters. These regularization constants make SSIM useless in point detection and weakly scattering problems. When the profile of the target is sparse within the ROI, the regularizing quantities take over the actual statistics of the images. The relative accuracy of the metric may decrease to a non-meaningful extent. The combination of the three indicator functions results in the metric SSIM, defined as

$$SSIM(x,y) = \frac{(2\mu_x\mu_y + C_1)(2\sigma_{x,y} + C_2)}{(\mu_x^2 + \mu_y^2 + C_1)(\sigma_x^2 + \sigma_y^2 + C_2)} \tag{6.10}$$

As aforementioned, the SSIM is applied locally rather than globally because statistical characteristics and distorting elements are typically highly non-stationary. Moreover, localized quality assessment methods can generate a quality map of the image that varies across different regions, offering detailed insights into the degradation of image quality. Since a scalar evaluation parameter is practically more suitable, the SSIM indicates the median value across patches within the image.

6.2 Number of bits per RIS-cell

The first descriptor is the number of discrete phase shifts achievable from each RIS cell. This quantity is expressed using the equivalent number of bits, such that $C = 2^b$. An ideal scenario involves an infinite number of cells, or meta-*atoms*, that can continuously change phase, achieving an exceptional spatial and angular resolution, ultimately limited by the intrinsic features of RF waves.

The discretization of the phase shift introduces a quantization error source that must be considered as a detrimental Signal-to-Noise Ratio (SNR) factor. The higher the number of bits, the more granular the phase correction and the better the achievable resolution. A binary quantization of the phase shift achievable by each cell leads to a quantization error uniformly distributed in the range $[0, 2\pi]$. The error can be defined as

$$\epsilon_\phi = \phi - \hat{\phi} \tag{6.11}$$

where $\epsilon_\phi \backsim \mathrm{U}[0, 2\pi]$ represents a uniformly distributed random variable related to the discretization of the continuous ϕ phase correction to the nearest configuration $\hat{\phi}$. Assuming uniform probability density function for this error, the power of such additional equivalent noise is given by integrating over the range of interest $[-\pi, \pi]$

$$P_\phi = \int_a^b \epsilon_{pdf} \cdot (x - \mu_x)^2 dx = \frac{(b-a)^2}{12} \tag{6.12}$$

The more bits per cell, the narrower the error domain and the lower the power of this quantization error. An infinite number of bits would lead to an $\mathbf{H}$ matrix maximizing elements along the diagonal.

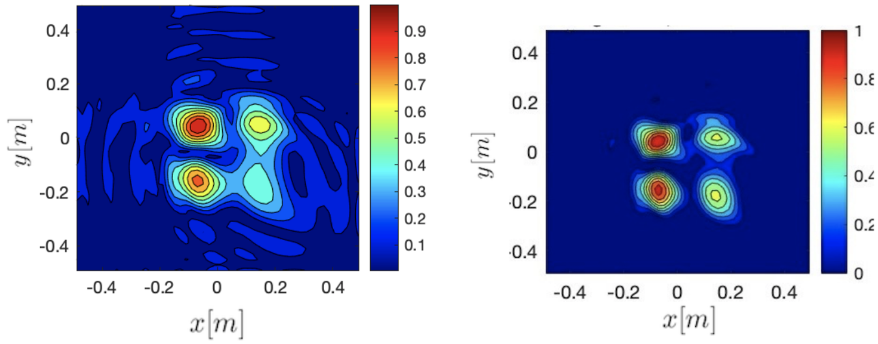

(a) b = 1

(b) b = 10

Figure 24: Numerical Validation - (*TSVD*, SNR=50 [dB], Q=10×10, $f_c = 5.825$ GHz, 4 distinct scatterers) - Retrieved albedo when $S = 1$. The quality is assessed by comparing a single-bit versus a continuous and ideal RIS phase tuning.

The vector $\Theta(m)$ is meant to intensify the electric field incident on a scatterer point of the target to boost the power measured at the receiver. Taking the magnitude of the complex $\mathbf{H}$ matrix and normalizing each row by its maximum value, the ideal scenario leads to

$$\mathbf{H}_s = \begin{bmatrix} 1 & 0.99 & 0.97 & ... \\ 0.99 & 1 & 0.99 & 0.98 \\ 0.96 & 0.97 & 1 & 0.98 \\ ... & 0.97 & 0.98 & 1 \end{bmatrix} \tag{6.13}$$

The $\mathbf{H}_s$matrix embeds CSI for a single carrier, and the convolution with the unknown albedo vector provides low field intensity as the targeted point exhibits a lower reflection capability(i.e., pixel identifying equal to 0). A poorer scattering profile of the object for a specific pixel of the ROI will result in a lower measured amplitude for the field. The most convenient fabrication approach is based on deploying many cells that are able to produce binary shifts. The discrete version of the phase correction is given as

$$\theta(m, q) = \begin{cases} 0 & \frac{-\pi}{2} < \Delta\tilde{\theta} < \frac{\pi}{2} \\ \\ \pi & \frac{\pi}{2} < \Delta\tilde{\theta} < \frac{3\pi}{2} \end{cases} \tag{6.14}$$

where m is the targeted scattering center and q is the RIS-cell operating specific phase correction.

6.3 Number of cells per RIS panel

The second important descriptor is the total number of required cells. Under the assumption of a 2D square panel, the number of cells per side is selected according to the required spatial resolution and the number of available sub-carriers. Intuitively, the higher the number of cells, the higher the elements in each $\Theta(m)$ configuration. The inversion process would benefit from the increase in the number of elements combining fields coherently to let the specific point contribution stand out among the others.

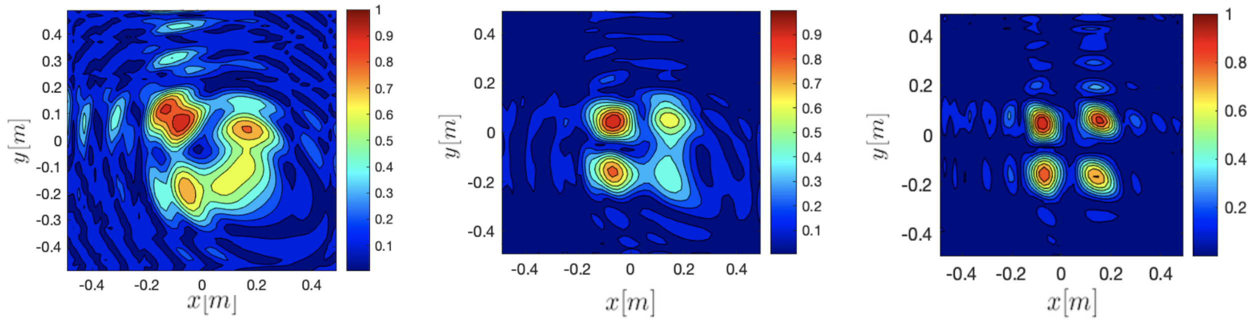

(a) Q = 7

(b) Q = 10

(c)Q = 13

Figure 25: Numerical Validation - (*TSVD*, SNR=50 [dB], Q is variable, $f_c = 5.825$ GHz, 4 distinct scatterers) - Retrieved albedo when $S = 1$. The quality is assessed by comparing three values of the side of the RIS panel.

The Reflective Smart Surface works basically as a Rectangular Array (URA). More elements bring out and highlight the diagonal elements from the transport matrix. More precisely, for $\mathbf{y}(1) = 0$, i.e., the target doesn't exist in the pixel of interest, the output would be $\mathbf{p}(1) = \mathbf{H}_1 \cdot \mathbf{y}$, where $\mathbf{H}_1$ is the first row of model matrix. The more the system can annihilate the terms coming from the remaining elements, the more granular the scattering profile reconstruction. A qualitative explanation of the phenomenon comes from the electromagnetics theory and the visual result shown in Figure 25.

From a more physical perspective, the number of cells carries out the same benefit as using a MIMO instead of a short dipole: the aperture physical size is increased, the resolution improves, and the reconstruction is more accurate. However, unlike the physical displacement of MIMO antennas, RIS does not require as much power, offers a more straightforward implementation and does not suffer from active element interaction. Moreover, smart reflectors steer the field without injecting noise or significant distortion into the wave.

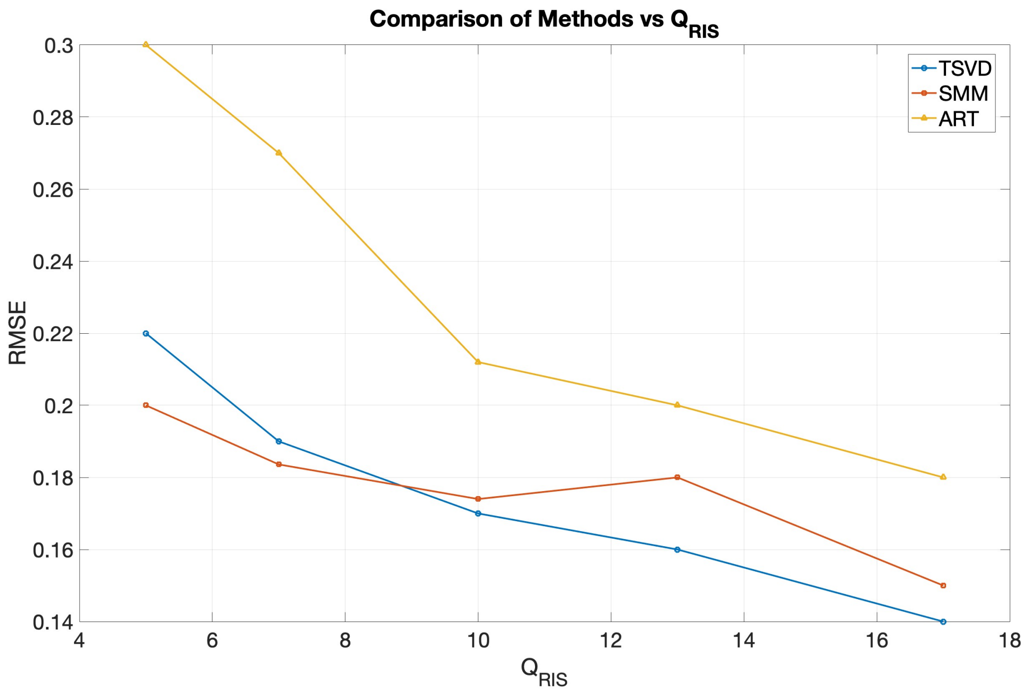

Figure 26: (SNR = 50 [dB], Q variable, S variable) - Retrieved 'O-shaped. TAll implemented methods are compared in terms of RMSE performance versus the size of the side of the RIS.

As shown in Figure 26, the three methods are tested with an O-shaped profile that can be imagined as a PEC thin object with a reflection index significantly different from the background. The RIS surface is always assumed to be a planar square array of reflecting $Q \times Q$

cells. All three methods show a sharp improvement in imaging performance in terms of RMSE as the RIS side increases, confirming the previously discussed intuition.

6.4 Number of carriers

The effectiveness of imaging depends on two more factors: the diversity and intensity of the measurements. First, the many different subcarriers that sample 40MHz channels increase the resolution and the detection of the region of interest. Unfortunately, this benefit saturates quickly above the ten samples because of the limited spatial variety as the number of samples increases.

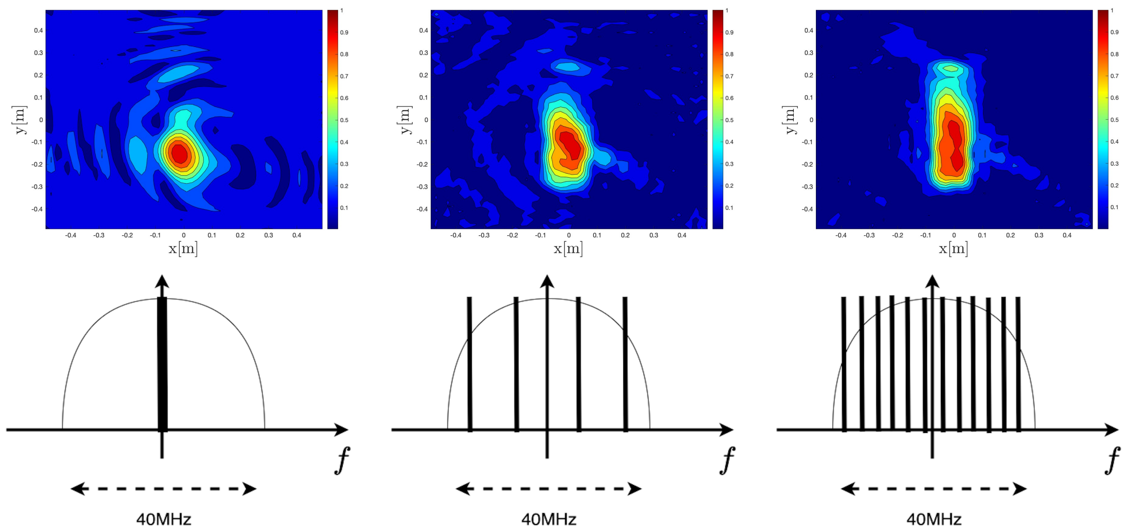

(a) S = 1 (b) S = 30 (c) S = 51

Figure 27: Numerical Validation - (*TSVD*, SNR=50 [dB], Q=10, f_c = 5.825 GHz, 4 distinct scatterers) - Retrieved albedo when S is variable. The quality is assessed by comparing increasing number of samples within same frequency channel

Second, the bandwidth covered by the WiFi system. Although the use of different channels requires slightly more time, spanning a wider frequency domain improves enormously the diversity in measures and the achievable resolution, as shown in Figure 27.

The main trade-off in our problem involves two aspects. On one hand, the use of multiple sub-carriers enhances resolution but significantly increases the volume of data to be processed. Each transport matrix computation needs to be repeated for each sub-channel. On the other hand, once the physical parameters and geometry are established (e.g., phase correction capabilities and number of cells per side), the computation of the **H** matrix becomes more efficient, reducing the actual computational load. Since the number of bits and physically available cells are determined by low-cost hardware, the CSI matrix can be computed based on channel bandwidth requirements and remains consistent across different targets.

6.5 Physical Geometry

The physical geometry of the system can impact the quality of the reconstruction for two main reasons. First, the geometry should span the spatial domain in a convenient way. The relative orientation of the objects for the same physical system, with the same descriptive parameters and ranges, can heavily affect performance. This intuitively happens as the RIS sample the spatial spectrum of the profile in a different way. The panel acts as an array of reflectors that change the phase but not immediately the spatial angle. The laws of reflection and scattering still hold. However, the phase combination of all contributions modifies the measured intensity at the receiver

$$\mathbf{p}_j = \sum_{q=1}^{Q} w_{q,j} \cdot f_i \tag{6.15}$$

The p_j is the single measure corresponding to a projection of the target reflectivity on the single-dimension antenna. The $w_{q,j}$ is the row of the overall matrix combining direct and reflected paths. In our case, the "slice" of the Fourier domain of the object is not given by a displacement of the MIMO receiver. Multiple measures rather synthesize the diversity.

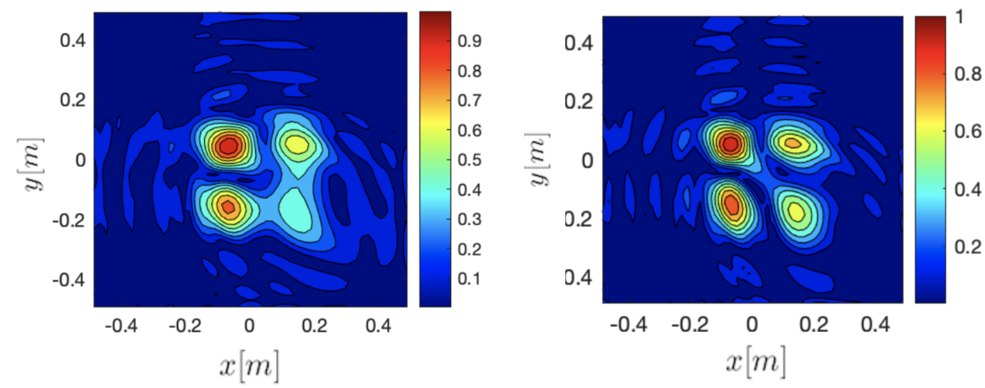

(a) R=1 (b) R=0.5

Figure 28: Numerical Validation - (*TSVD*, SNR=50 [dB], Q=10×10, f_c = 5.825 GHz, 4 distinct scatterers) - Retrieved albedo when S=1. The quality is assessed by comparing two similar geometries with a different target-to-RIS slant range

Second, the geometry must be carefully chosen to prevent distance self-compensation when moving between URA elements and target pixels. The RIS panel adjusts the phase of the incident electromagnetic field to ensure that the direct and reflected paths add coherently. Similar to how an infinite set of plane waves can represent a cylindrical wave, using a range of time-domain shifts can enhance the intensity of points on the target with a high-contrast scattering profile. From Chapter 2 the system cross-resolution is recalled to be

$$\delta_x = \frac{\lambda}{L_{RIS}} \cdot R \tag{6.16}$$

with L_{RIS} physical aperture of the equivalent URA made by the RIS[12]. As the slant distance R between the target and the panel decreases, the cross-resolution improves due to a corresponding increase in the incident field and a power boost along the diagonal of the $\mathbf{H}$ matrix. When the object inhomogeneities are large compared to wavelengths, energy propagation is characterized by refraction and multi-path effects. The system neglects diffraction as long as the object inhomogeneities are smaller than the wavelength from the lowest sub-carrier[14].

CHAPTER 7

NUMERICAL RESULTS

(Previously published as part of Tortoriello, C., Erricolo, D., and Oliveri, G.: Wave Manipulating RIS for Enhanced Tomographic Imaging: Concept and Recent Advances. In 2024 United States National Committee of URSI National Radio Science Meeting (USNC-URSI NRSM), pages 236–237, 2024)

This section aims to validate the proposed RIS-aided imaging approaches numerically and to provide a comparative analysis considering different target shapes and noise levels. The simulated scenario is setup for testing the RIS-aided WiFi imaging system, as shown in Figure 29, with two single antenna APs located at (-1, -1, 0.5) [m] (i.e., the AP_{tx}), and (1, 1, 0.5) [m] (i.e., the AP_{rx}). The RIS is made of a planar array of meta-atoms displaced on the xy-plane, the origin of which matches the origin of the primary reference frame. The RIS panel is modeled by assuming a realistic single-bit-per-atom architecture to address a "worst-case" scenario involving the cheapest possible skin architecture. To illustrate the proposed imaging process, a WiFi signal emitted by one of the access points is assumed to scan the target, exploiting an 802.11n standard emission protocol. The transmitter is assumed to operate over a spectrum of S sub-carriers uniformly sampled in two ways.

First, several S sub-carriers sample uniformly the available spectrum of a single 40MHz channel centered at 5.825 GHz, as described in Chapter 6. Second, the S sub-carriers sample uniformly the overall spectrum spread across three 40MHz channels in the 5 GHz to 6 GHz domain. The imaging of an object is strictly related to both *how* the target is physically illuminated and *what frequency* is used. From radio frequency and ultrasonic tomography [43], it is well known the tight correlation between the object (spatial) frequency components and the frequency f_0 of the incident field. In particular, the higher the frequency, the more components frequency are encompassed, and the better the imaging of the target.

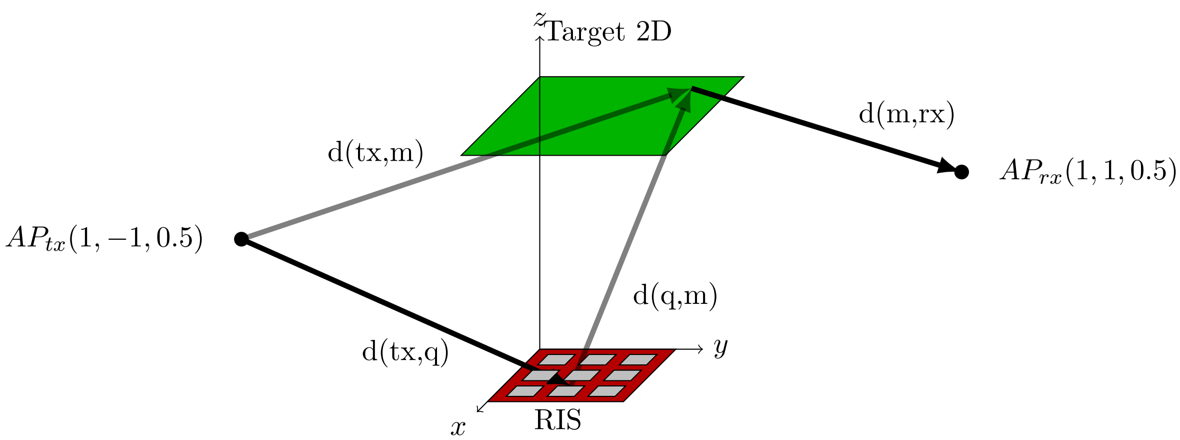

Figure 29: *Problem Formulation* - The transmitting AP (left) illuminates the scenario including both the target and the RItS, and the receiving AP (right) collects the total scattered field.

7.1 Point detection comparison with variable noise

As a first illustrative example, the ART, Sparse Majorization-Minimization, and TSVD are compared in terms of point detection capabilities. Point detection was selected for two main reasons. First, the detection of multiple points is crucial to assess the overall consistency of the simulated results with the expected physical properties. Second, the simple target allows an isolated analysis. In particular, it is possible to compare the robustness and quality of the reconstruction in a noisy environment for each technique. This approach would be more intricate with non-trivial profiles characterized by a greater radar cross-section. The rich scattering of the object profile would increase the power measured at the receiver, corrupting the spatial frequencies that form the actual image. For this reason, the test against this basic shape can better highlight the differences among algorithms in terms of effectiveness. The following studies aim to assess the features of RIS-aided imaging even when dealing with heavily corrupted data (i.e., SNR=0 dB). Such conditions are much more complex than those usually assessed in the literature [8]. This scenario more likely recreates a realistic WiFi opportunistic configuration where non-dedicated hardware is at hand.

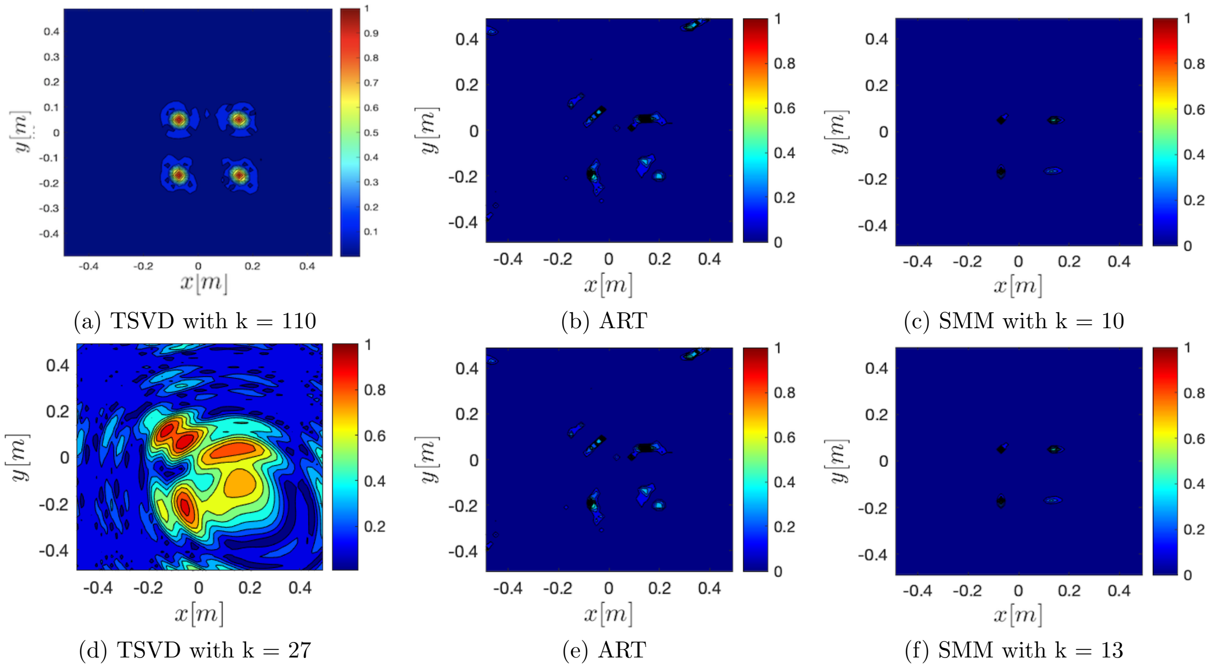

Figure 30: (SNR 0 dB; $Q = 10 \times 10$, $S = 30$, narrowband single channel, $f_c = 5.825$ GHz) - Retrieved 4-points albedo.

The "4-point" profile retrieval under such an assumption is shown in Figure 30. The comparison is assessed according to three main metrics.

First, the imaging quality is determined according to the SSIM and RMSE, as mentioned in the introduction of the chapter. Despite the uncorrelated nature of the additive noise, lower SNR significantly affects the recoverable spatial frequency spectrum from the measured profile. The presented SMM-enhanced achieves an RMSE of 0.023 with SNR equal to 6dB up to 0.09 with the maximum noise-simulated configuration(SNR = 0dB). The reported results show that the more efficient SMM technique outperforms TSVD in terms of albedo profile retrieval regardless of the noise level. On the other hand, TSVD suffers from severe distortion of results under higher noise levels. TSVD exhibits an RMSE of 0.28 with SNR equal to 6dB and reaches 0.39 as the SNR increases to 0 dB.

As noted in Chapter 4, direct methods struggle to integrate a-priori information about albedo into the reconstruction process. This limitation is a game-changing challenge in noisy environments. Conversely, the iterative methods perform exceptionally well, even under harsh conditions. In particular, the Sparse Majorization-Minimization (SMM) method achieves the best results, surpassing most current RIS-based imaging systems with an RMSE of approximately 0.022. It is also worth remarking that both iterative methods, SMM and ART, exhibit exceptional robustness even when the noise becomes comparable to the signal strength (i.e., SNR $\rightarrow$ 0 [dB]). This is expected owing to the more sparseness-promoting nature of SSM and the better physical knowledge integration compared to the TSVD regularization of the objective.

However, this technique faces challenges in maintaining a well-conditioned system. Although it performs well on average, it requires stronger regularization to handle injected noise, which increases the risk of errors. A further remark is significant when comparing implemented iterative approaches. The main downside of Sparse Majorization-Minimization is the empirical nature of regularization, which does not automatically fit the noise. In contrast, ART is computationally efficient, provides robust performance, and demonstrates stable convergence in the presence of noise. ART offers a better overall trade-off. The method consistently delivers high-quality results across various noise levels. In particular, the real-part constraint discussed in ART-dedicated Chapter 5 is a critical advantage. While the relaxation parameter μ can be adjusted for specific image features of interest, the multiple degrees of freedom through inner cycle thresholds and stopping rules enhance retrieval accuracy. ART also converges rapidly, requiring only 11 outer iterations to solve the problem, and its key strength is its self-tuning regularization. The most desirable feature of ART, compared to Sparse Majorization-Minimization, lies in the determinism of its regularization. The ART stop rule is highly effective and adapts automatically to changing noise levels, offering improved versatility. On the other hand, a noise-dependent μ parameter for SMM could be a partial solution, but prior information about the noise level would be needed.

7.1.1 SNR, Regularization, and Imaging

The importance of regularization and constraints, as discussed in Chapter 5, becomes even more evident with increased measurement noise. The model does not consider measurement time correlation in scenarios where multi-frequency measurements are taken at different times. However, higher noise levels, characterized by lower SNR, increase correlation among measurements at each frequency. Proximate phase corrections set similar rows. This aspect worsens conditioning due to the proximity of adjacent rows. Increased noise levels over damp fine-grained differences that enlarge resolution, especially for TSVD. In iterative approaches, the critical advantage is the synergy between regularization and physical constraints.

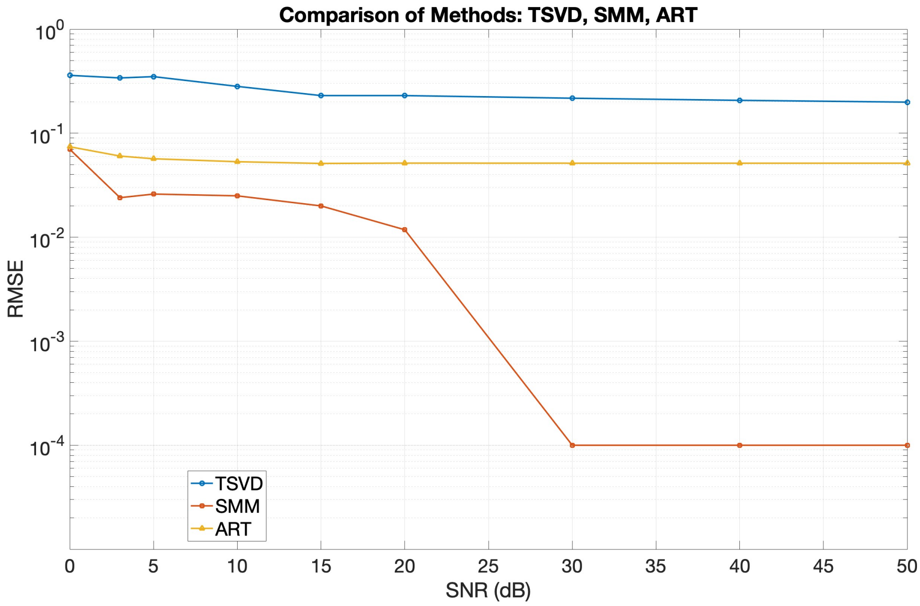

Figure 31: RMSE in log scale versus linear scale SNR - (comparison of implemented algorithms, $Q = 10 \times 10$, $f_c = 5.825$ GHz) - Profiles of the "4-points" albedo.

The final numerical experiment resumes the reconstruction accuracy of $RMSE$ versus the SNR obtained by TSVD and SMM when dealing with the "4-points" profile from Figure 30. The plot in Figure 31 shows the grid comparison from Figure 30 from a different perspective. The point detection is tested with 10 equally spaced values of SNR for the newly presented methods. The ART method exhibits exceptional robustness with the same reconstruction quality and mild difference. Impressively, the SMM exhibits excellent performance with a curve converging to the same ART performance where the noise configuration reaches significant values closer to the origin.

On the other hand, the TSVD is barely able to display the four distinct points, resulting in a higher offset from the previous curve as well as a steeper concavity as the noise ratio approaches the linear unity.

7.2 Effect of number of carriers compared to occupied bandwidth

This section explores the impact of frequency bandwidth and channel partitioning on imaging quality, focusing on two distinct scenarios. The first involves a single channel sampled with increasing resolution, while the second employs three 40 MHz channels in the 5-6 GHz range. Both cases use $Q = 10$ for side of RIS panel to image an "O"-shaped profile. Two reconstruction methods are compared in terms of RMSE evaluation metric: ART and TSVD.

ART stands out for its simplicity and flexibility, requiring significantly less computational effort. TSVD exhibits a clear advantage in delivering higher image quality when looking at RMSE. The analysis illustrated in Figure 32 shows that both methods benefit from increasing the number of samples. Although both frequency setups improve performance, the image quality is significantly enhanced by the 3-channel frequency bandwidth. Therefore, a multi-channel setup covering a broader range provides a significant improvement in reconstruction quality.

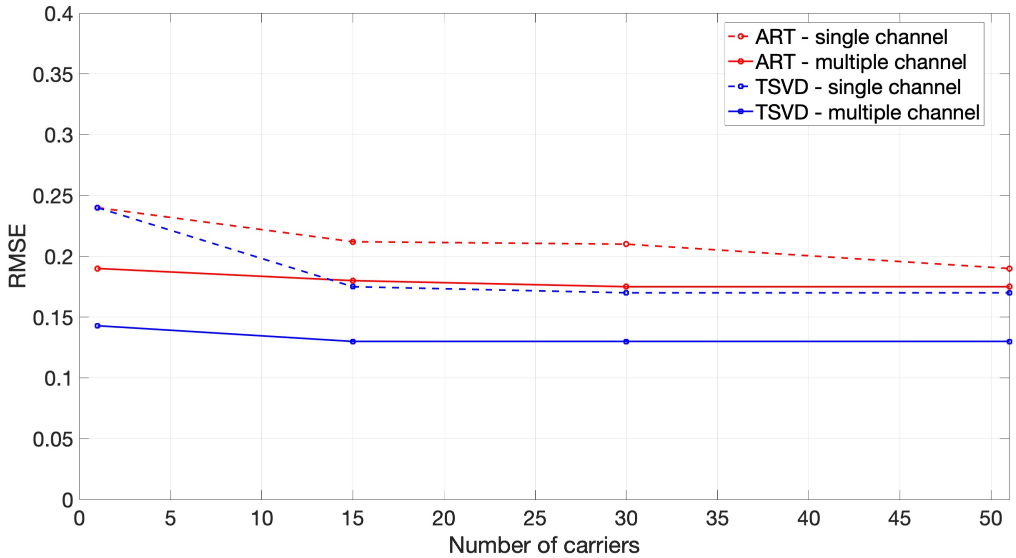

Figure 32: (SNR = 50 [dB], Q = 10 × 10, variable S) - Retrieved 'O-shaped' albedo ART and TSVD, RMSE performance versus number of carriers.

In the second scenario illustrated in Figure 33, Sparse Majorization-Minimization (SMM) is compared with ART, focusing on SSIM and the effectiveness of bandwidth expansion. SMM performs similarly to ART in single-channel configurations but outperforms ART as the number of carriers increases. In the multi-channel setup, SMM delivers exceptional performance, with the ability to reconstruct nearly the entire object, achieving an SSIM of 0.8 or higher when using at least 40 carriers.

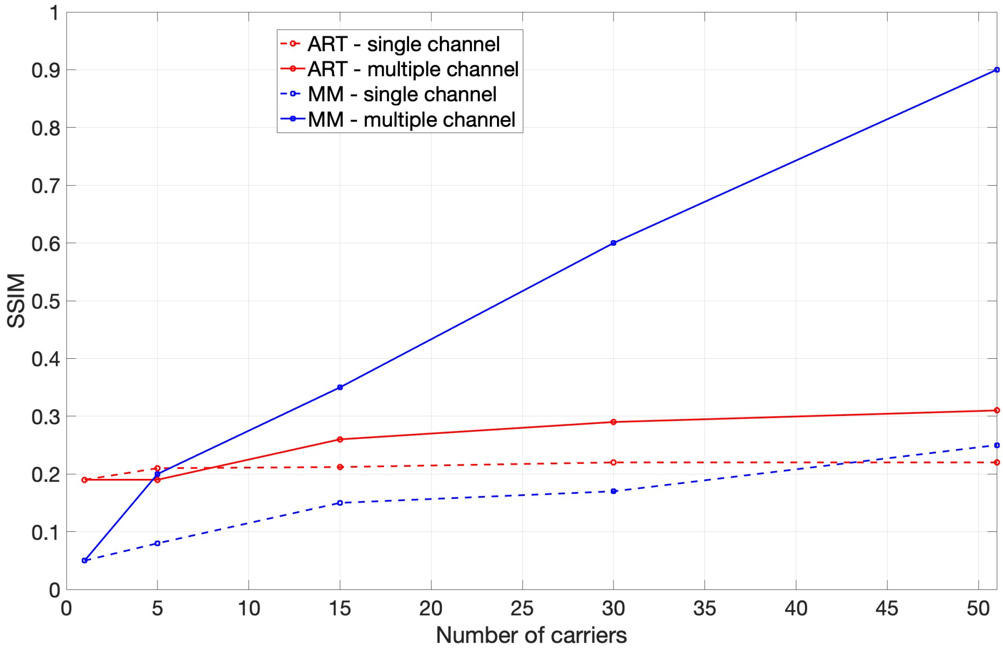

Figure 33: (SNR = 50 [dB], $Q = 10 \times 10$, variable S) - Retrieved 'O-shaped' albedo ART and SMM, SSIM performance versus number of carriers.

SMM shows significantly better performance with complexity close to ART. As detailed in Chapter 5, regularization in iterative techniques is attained in two ways: the fixed μ parameter based on noise level and a lower bound for pixel values. Both features can accelerate processing and sharpen edges but may potentially eliminate useful information by applying a low-pass filter. The heuristic nature of the SMM algorithm makes it less adaptable to various contexts than ART.

7.3 Low-noise retrieval

The following imaging quality assessment primarily compares SMM and TSVD without explicitly considering ART. The choice is motivated by significantly lower image reconstruction quality stressed in dedicated Chapter 5

7.3.1 Single channel, 30 sub-carriers, basic inversion

The imaging illustrative scenario deals with the retrieval of simple shapes [i.e., "E"-profile - Figure 35(a); "O"-profile - Figure 35(b)] when dealing with very low noise conditions ($SNR =$ 50 [dB]), $S = 30$ sub-carriers in a single narrowband channel, and a RIS of 10×10 cells.

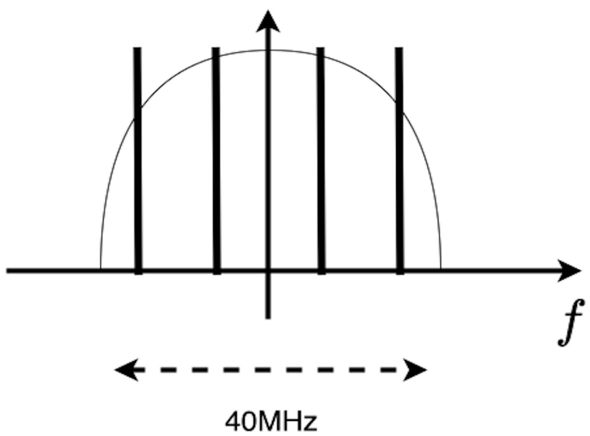

Figure 34: Frequency domain partitioning for the low-noise imaging scenario

This first comparison is illustrated in Figure 35 for narrowband, single-channel configuration with standard inversion techniques.

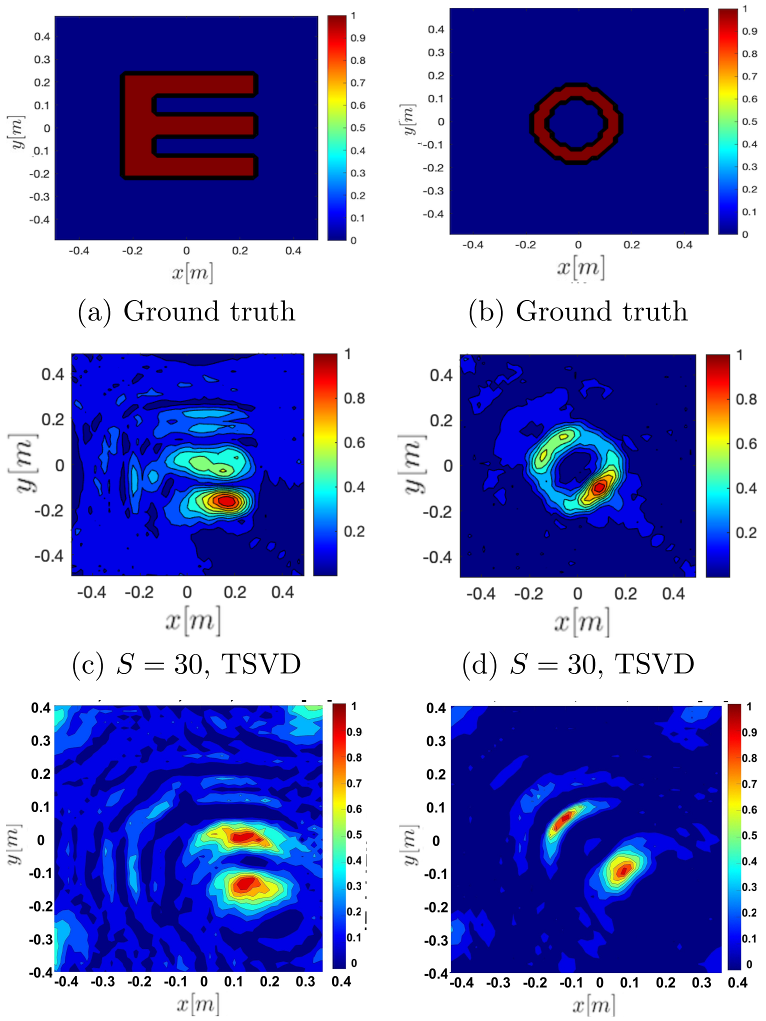

(a) Ground truth (b) Ground truth

(c) $S = 30$, TSVD (d) $S = 30$, TSVD

(e) $S = 30$, SMM (f) $S = 30$, SMM

Figure 35: Numerical Validation - ($SNR = 50$ [dB], $Q = 10 \times 10$, $f_c = 5.825$ GHz, O-shaped profile) - Retrieved albedo by (c)-(d) TSVD and (e)-(f) SMM when dealing with different S values.

Although we are working with minimum resolution and quite a rich profile, the TSVD albedo reconstruction[Figure 35(c), Figure 35(d)] shows relatively better accuracy than standard SMM. Such a result is methodologically expected owing to the nature of classic TSVD retrieval. This is actually confirmed by the corresponding accuracy indexes [e.g., $SSIM = 0.15$, $RMSE = 0.27$ - Figure 35(d)]. On the other hand, the straightforward implementation of the SMM can barely detect the objects. In fact, the retrieval shown under the same assumptions [E-Object - Figure 37(e); O-Object - Figure 37(f)] yields a very poor accuracy compared to the TSVD method (Figure 35). Such an outcome is caused by the sparse-promoting nature of the SMM solver and by RIS size.

7.3.2 Single channel, 30 sub-carriers, enhanced inversion

The enhanced version of SMM integrates physical information to carve the best performance out of the pattern. It is worth remarking that such performance can be improved by taking into account the boundaries of the albedo [”SMM Enhanced”- Figure 36(e), Figure 36(f)], yielding $SSIM = 0.21$ and $RMSE = 0.2$ on average, aligned with TSVD outcomes.

This is also confirmed when dealing with different profiles [i.e., ”I-shaped” profile - Figure 36(a), Figure 36(d)].

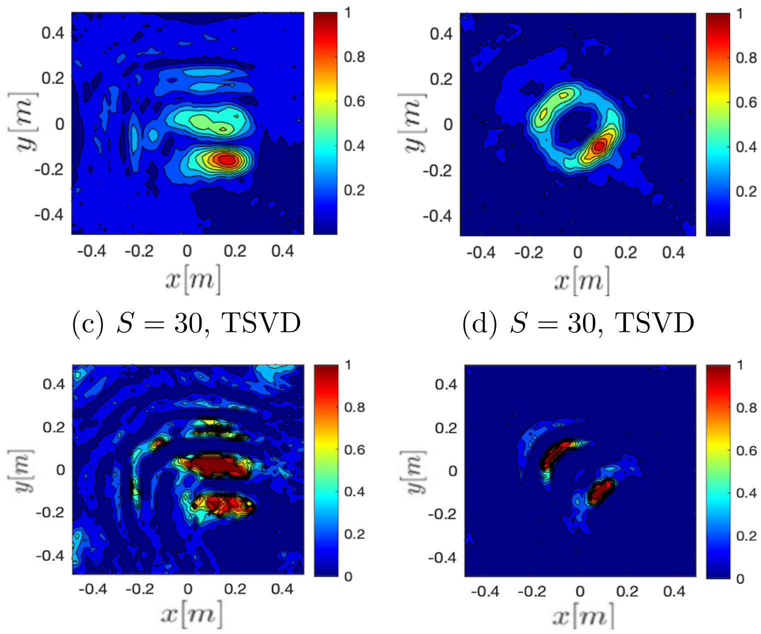

(c) $S = 30$, TSVD (d) $S = 30$, TSVD

(e) $S = 30$, SMM *enhanced* (f)$S = 30$, SMM *enhanced*

Figure 36: Numerical Validation - ($SNR = 50$ [dB], $Q = 10 \times 10$, $f_c = 5.825$ GHz, O-shaped profile) - Retrieved albedo by (a)-(b) TSVD and (c)-(d) SMM *enhanced* technique.

The iterative solution integrates a *stoprule* with the a-priori knowledge about the physical system. This approach leads to sharp imaging results improvement at a much lower computational effort than both TSVD or any previously considered system [8; 10].

7.3.3 Multi-channel, 51 sub-carriers, enhanced version

The final configuration aims to achieve the best possible performance for the research. The maximum bandwidth span improves diversity as specified in Chapter 6. The number of subcarriers is increased to 51. The wider span in frequency allows for a slight improvement from 30 to

51 subcarriers since the same "spectrum of configurations" is sampled finely without necessarily saturating. The RIS size is increased to a panel of size 13x13 up to a 17x17 configuration to maximize granularity. Given the hardware limitation discussed in previous chapters about RIS fabrication feasibility, this assessment is meant to check the upper bound of the results rather than to provide an effective practical method.

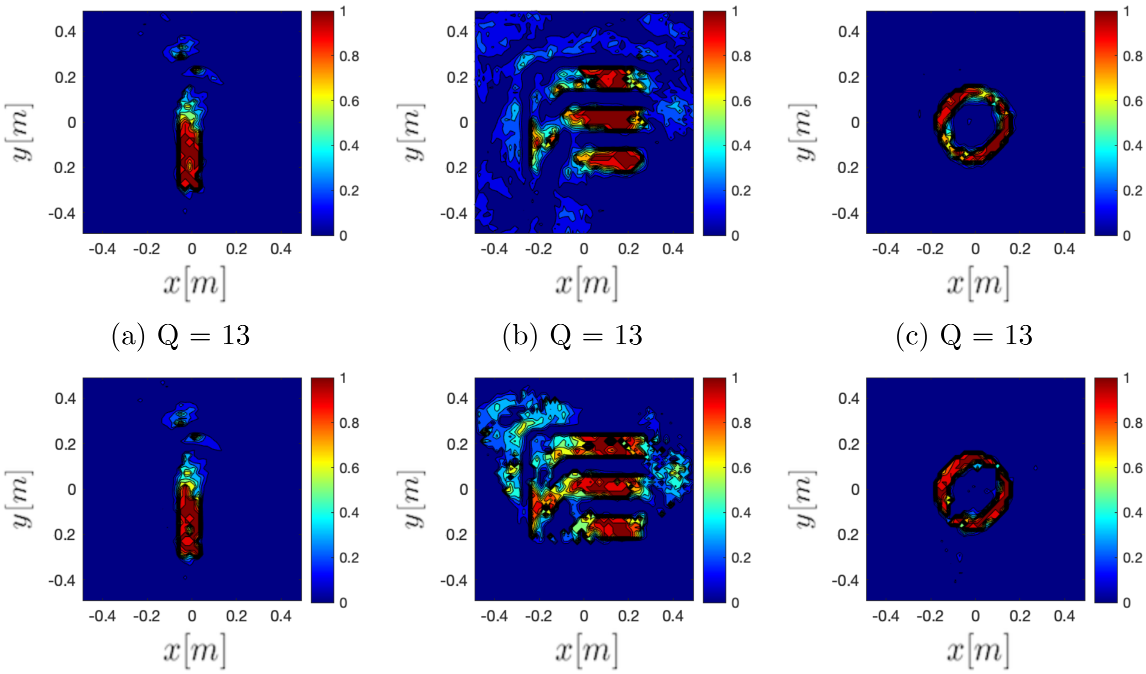

(a) Q = 13 (b) Q = 13 (c) Q = 13

(d) Q = 17 (e) Q = 17 (f) Q = 17

Figure 37: (SNR = 50 [dB], SMM, S = 51 spread over three channels, f_c = 5.825 GHz) - Retrieved albedo.'I'-shaped, 'O'-shaped , 'E'-shaped

To further assess and compare reconstruction quality, it is worthy to investigate by testing the three implemented algorithms against a variety of profiles to evaluate the cumulative distribution function computed empirically. The ECDF(Empirical Cumulative Distribution Function) indicates in stochastic theory the (empirical) probability that a function falls under a given value. In more practical terms, let us consider the two main metrics of interest, and let's build the curves of interest. First, the three methods are tested in a noiseless scenario with Q = 13 cells per side for the RIS panel. The choice is motivated by improving resolution and getting a clear grasp of the estimated cdf. For the same reason, the best spectrum configuration of S=51 samples over three channels is selected. The curve is built according to three steps. First, a technique is tested against a set of two-dimensional profiles, and the metrics over interest are tracked down. Second, the metrics are sorted in ascending order for the values . Finally, the ecdf is built with a staircase approach made of as many steps as the number of profiles investigated

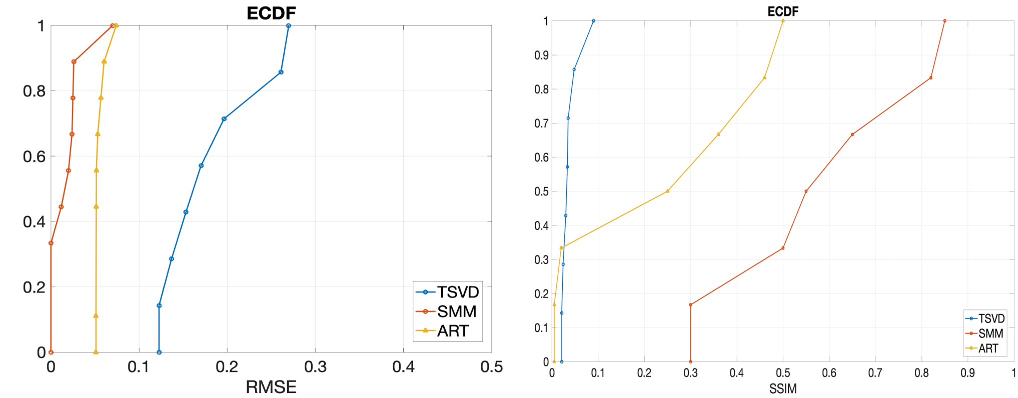

(a) RMSE (b) SSIM

Figure 38: ($SNR = 50$ [dB], Q $= 13 \times 13$, S=51 spread over three channels, $f_c = 5.825$ GHz) -Methods ECDF comparison for a s et of albedo under test

The Figure 38 shows for both metrics. The (Figure 38(a)) compares the ECDF in terms of RMSE performance, highlighting a step between iterative methods and TSVD. In a practical sense, this means that both ART and SMM are quite more effective in terms of imaging sharp profiles in noiseless environments. For RMSE below roughly 0.1 all tested profiles show acceptable results for both ART and SMM. Conversely, being interested in a fixed level of image corruption(vertical line), TSVD experiences higher variance or image high-frequency noise than ART and SMM. The same consideration from a different perspective is provided for SSIM (Figure 38(b)). In particular, the SMM shows exceptional results for values of SSIM as compared to TSVD. When selecting an SSIM value between 0.4 and 0.5, which generally indicates a moderate reconstruction quality, TSVD fails to provide a satisfactory result. Conversely, iterative methods can deliver very good quality at significantly lower costs. Sparse Majorization-

Minimization approach proves itself the best option in terms of RF noiseless imaging, being the only method capable of overcoming 0.7 SSIM with some specific study cases. Figure 38 is quite explanatory of how the iterative techniques benefit from frequency workarounds and physical knowledge about the profiles more than TSVD. Direct method is standard, simple and effective to a certain stage but cannot keep up the level as some small workaround are introduced within the system. Moreover, in many practical situation TSVD is definitely to avoid due to severe memory storage requirements and running time.

7.4 Benchmarking imaging performance against state-of-the-art techniques

A more comprehensive assessment, comparing the properties of the discussed approach with state-of-the-art techniques in terms of $SSIM$ and $RMSE$, is presented for an "E-shaped" profile under low noise conditions, as shown in Table I. More specifically, different algorithms as described in [8; 10] have been considered for comparison with the proposed approach.

TSVD refers to the standard reconstruction procedure in a narrow-band configuration, as described in Chapter 4.

The TSVD-enhanced from the second entry in table Table I refers to the improvement of imaging achieved by increasing the number of narrow-band channels at 5GHz.

The Algebraic Reconstruction Technique (ART) from computed tomography has been implemented as outlined in Chapter 5. For simplicity, the basic unconstrained approach has been tested alongside the other methods. As emphasized in Chapter 5, achieving optimal imaging requires a more effective inversion technique.

The *RIS-Opt* method, as detailed in [8], is structured as follows. To regularize the objective function, an infinite norm penalty is introduced. The problem is then addressed using the Augmented Lagrangian Multiplier Method (ADMM). This modified problem is solved iteratively by applying soft-thresholding to the singular value decomposition of the image patches. The method is highly efficient and, to the best of the author's knowledge, represents the state-of-the-art in RIS-aided RF imaging.

TABLE I: NUMERICAL VALIDATION- ($Q = 10 \times 10$, $S = 30$, $f_c = 5.825$ GHz, "E-SHAPED" PROFILE, $SNR = 50$ dB) - ERROR FIGURES.

Method	**RMSE**	**SSIM**
TSVD (this work)	0.20	0.16
TSVD-Enhanced (this work)	0.13	0.30
ART (this work)	0.17	0.04
Sparse MM (this work)	0.15	0.27
RIS-Opt (Optimization-based algorithm) [8]	0.03	0.52
RIS-BF (Beamforming)[8]	0.07	0.42
Commodity WiFi Imaging System [44]	0.28	0.31
Sparse MM-Enanched (this work)	0.08	0.70

The beamforming method *RIS-BF* images the target by constructively combining the phase shift from all RIS elements and subcarriers. As described in [8], the performance of beamforming is more sensitive to the quantization level of phase shifting value, which is a hardware constraint of the problem.

The further functional comparison refers to using a Commodity WIFI Imaging system based on a 3x3 physical MIMO. This technique images the target thanks to better space sampling through the transmitting and receiving planar arrays.

The presented results demonstrate the superiority of the proposed SMM modified approach when dealing with a benchmark target shape.

CHAPTER 8

CONCLUSION

The integration of Reflective Intelligent Surfaces (RIS) in Smart Electromagnetic Environments has gained significant attention in recent years. The use of programmable arrays of passive reflectors enhances energy efficiency (EE), spectral efficiency, and reduces hardware costs. However, the imaging and detection capabilities of RIS-aided RF systems are still in their early stages, with only a few studies available. Much of the mathematical and physical foundations remain to be rigorously explored.

Several concepts from Computed Tomography, Radar, scattering theory, and multi-dimensional signal processing can be applied to object imaging in these systems. From a theoretical perspective, both direct and iterative inversion techniques have been explored. The direct approach, particularly Truncated Singular Value Decomposition (TSVD), achieved good resolution but at a high computational cost. Among the wide range of iterative methods, the Algebraic Reconstruction Technique (ART) and Sparse Majorization-Minimization (Sparse MM) were discussed and tested in this context.

Chapter 7 compares these three methods and evaluates the best solutions. In noiseless imaging conditions, the challenge is driven by he intrinsically ill-posed nature of the inversion problem. Iterative methods, in general, demonstrate lower complexity. This is thanks to the use of stop rules and finely adjustable regularization. On their side, iterative approaches can integrate physical information about the discrete reflectivity profile being reconstructed. These features enhance both convergence and the final image quality. In noisy environments, particularly for point detection, the Sparse MM approach offers the best tradeoff between complexity and detection capability in challenging conditions. ART demonstrated strong potential, standing out as the least complex numerically. However, many results remain inadequate for the currently adopted forward model, possibly due to the average contrast between the object and the background. A final remarkable perspective of our results and those available in literature are presented and discussed.

8.1 Next steps

The field of Reflective Intelligent Surfaces (RIS) in Smart Electromagnetic Environments (SEME) remains largely unexplored. This area holds substantial promise across various domains, including biomedical applications, civil engineering, communication, and detection. The growing interest in RIS is driven by its potential to revolutionize the interaction with electromagnetic environments. One of the key advantages of RIS technology is the ability to enhance spectral efficiency. RIS can deliver more data within the channel and the capacity of communication systems, by optimizing the use of available bandwidth. RIS systems contribute to lower noise levels. The absence of active elements in these surfaces means that less noise is introduced into the environment, which improves the signal-to-noise ratio and overall system performance. RIS helps to mitigate multi-path effects, which are often a significant challenge in traditional communication systems. RIS reduces the interference caused by multiple signal paths by controlling the reflection of signals. This leads to more precise and reliable communication.

Another notable benefit is the improved energy efficiency(EE). RIS technology enables more efficient use of energy by reflecting signals rather than generating them, leading to reduced power consumption and operational costs. Overall, the integration of RIS in SEME looks promising to promote electromagnetic environment optimizations, opening new avenues for research and application in this exciting and evolving field.

It is essential to document the work and highlight some of the insights or potential misconceptions encountered during this research, as this can contribute to advancing the RIS-aided imaging field.

One suggestion for future research is to test **alternative iterative approaches** such as simultaneous iterative reconstruction techniques (SIRT). This generally results in higher image quality than ART, although it converges more slowly. SIRT is an iterative algorithm belonging to the same class as ART but with a significant difference. In SIRT, the value of the j-th cell is not updated immediately after the i-th equation. Solution updates occur only after all equations have been evaluated. Consequently, the update for each cell represents the average of all computed changes for that cell. As with standard techniques in ART, relaxation can help mitigate the effects of noise in reconstructions. In this method, a pixel is updated by $\mu \cdot \mathrm{f}_{ij}$, where μ is less than 1. At times, μ is defined as a function of the iteration number, progressively decreasing as the number of iterations increases. This adjustment generally enhances reconstruction quality but may also slow down convergence.

Bandwidth and Imaging Integrating 6G technology in WiFi applications could potentially advance RIS-aided WiFi imaging by leveraging these frequency factors to improve performance. Although widely available prototypes are not yet present, interesting experimental devices have been created using diode-like structures to modify the incident field phase. Conducting **hardware-based experimental analysis** could significantly enhance the current models. Such analysis is likely to reveal model inaccuracies or oversimplifications, thereby improving the overall quality and reliability of the imaging system.

Simple MIMO systems have already been implemented in modern IEEE WiFi protocols. However, an intriguing approach could involve exploiting a larger array of apertures to enhance resolution. The presented method could provide a significantly sharper solution, offering improved accuracy and detail in **3D imaging** by modulating the frequency over the bandwidth of interest. The last intuition I consider worth investigating is the model scalar nature itself. This strong but reasonable assumption comes from the need of a simple hardware(i.e. short or *infinitesimal* dipoles). However, working on the polarization (Circular or crossed polarization) of the impinging field could improve the granularity of the results at the slight cost of more costly hardware. The trade-off with the data-processing complexity is set as usual. Vectorial shape triplicates complexity for the model but an accurate implementation could carry out significant improvement.

APPENDICES

Appendix A

A.1 Uniform Linear Array

The WiFi-based imaging system uses antennas that are simple enough to have low-cost hardware and leverage RIS to increase physical aperture. Since the RIS is made of a set of elements reflecting the field, the entire surface can be studied as a phased planar array. Under FarField approximation with $\lambda << R$ the majority of propagating waves can be simply approximated with ideal plane waves impinging on a region of interest. Assuming a plane wave incident with θ angle on a linear array made of N ideal elements, the Array Factor(AF) can be introduced. The AF is a crucial parameter accounting for the 3D behavior of radiation patterns. The way an array is fed can change the inter-element phase shift. The *phased array* most straightforward configuration assumes uniform magnitude feeding with a progressive phase shift

$$\Delta\phi = k \cdot d \cdot cos(\theta) \tag{A.1}$$

There are two ways to determine the expected imaging resolution according to antenna arrays theory. The first one is based on Fast Fourier Transform(FFT) concepts applied to the newly introduced *spatial frequency* concept for each MIMO array element, defined for this 1D case as

$$\omega(m) = \frac{2\pi}{\lambda} m \cdot d \cdot cos(\theta) \tag{A.2}$$

Appendix A (continued)

The elements displaced along one dimension '*sample the space*' are spaced by d. Each sample is mapped to a spatial frequency component so that N spatial spectrum components are provided[12].

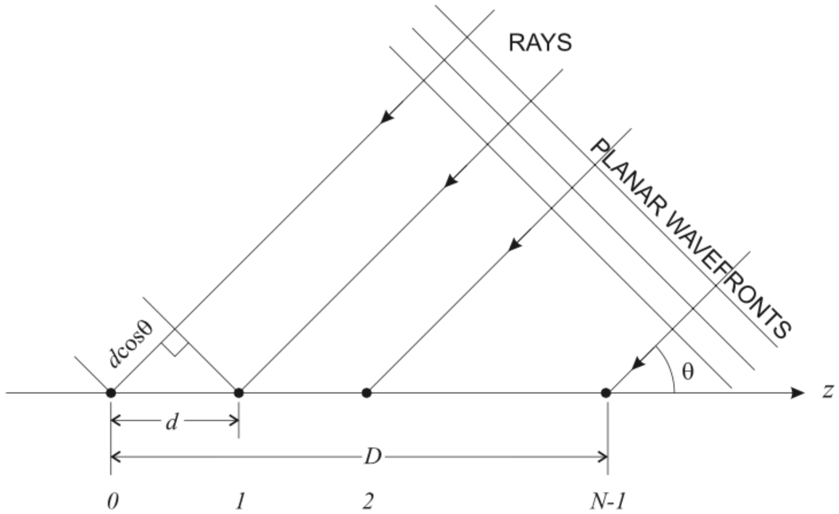

Figure 39: Linear array geometry with $d \leq \frac{\lambda}{2}$ and θ angle of incidence

Two adjacent components in this spatial frequency domain are separated by $\frac{2\pi}{N}$. This outcome is consistent with the intuition that a higher N number of elements per side provides fine-grained resolution. The more N samples, the more accurately the discrete spectrum is

Appendix A (continued)

sliced, and the finer the space scan [45]. To prove the dependency of angular resolution, or antenna beamwidth, from number of elements let us consider two adjacent frequencies

$$\omega_1 = \frac{2\pi}{\lambda} \cdot d \cdot sin(\theta) \qquad \omega_2 = \frac{2\pi}{\lambda} \cdot d \cdot sin(\theta + \Delta\theta) \tag{A.3}$$

Notice that the theta is now considered from the broadside. The mutual difference among components is at least $\frac{2\pi}{N}$ and then

$$\Delta\omega = \omega_1 - \omega_2 = \frac{2\pi d}{\lambda} \left(sin(\theta + \Delta\theta) - sin(\theta) \right) \geq \frac{2\pi}{N} \tag{A.4}$$

Assuming a θ evaluation close to broadside, the inequality becomes:

$$\frac{2\pi d}{\lambda} \sin(\Delta\theta) \geq \frac{2\pi}{N} \tag{A.5}$$

By simplifying further we can solve

$$\sin(\Delta\theta) \approx \Delta\theta \leq \frac{\lambda}{dN} \tag{A.6}$$

Appendix A (continued)

Since the RIS steers the beam towards the broadside direction, the beam width increases as either the wavelength increases or the number of elements decreases. The second way to describe same intuition is based on general resolution definition

$$\Delta\theta = \frac{\lambda}{D} \tag{A.7}$$

Again, the lower the frequency the worse the resolution. D indicates the diameter of the antenna, related to the physical size of the array. D pushes for better resolution as the beam width of the array narrows, assuming a unitary distance for simplicity. The aperture of an array of isotropic elements modifies the expression as follows

$$\Delta\theta = \frac{\lambda}{Nd} \tag{A.8}$$

The azimuth resolution of the overall system is obtained by multiplying the angular resolution by the range R, given in our case by the distance between the RIS panel and the target

$$\Delta\theta = \frac{\lambda}{Nd} \tag{A.9}$$

Appendix A (continued)

A.2 Uniform Rectangular Array(URA)

The Uniform Rectangular Arrays are 2D MIMO antennas displaced across a plane according to cross-range resolutions set by the problem specification, the expected shape of the figure in our case.

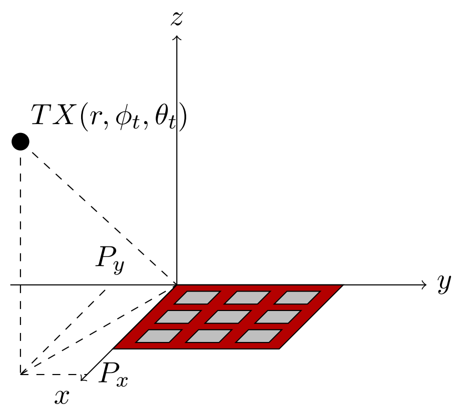

Figure 40: RIS 3D model with point P and dashed lines for azimuth and elevation angles: tx side

The grid shape is suited for matrix-like indexing where each element is referred to using rows and columns. The position vector of the $(m, n)_{th}$ element is given by

$$\mathbf{r}_{m,n} = x_{m,n}\hat{\mathbf{x}} + y_{m,n}\hat{\mathbf{y}} + z_{m,n}\hat{\mathbf{z}} \tag{A.10}$$

Appendix A (continued)

Thanks to the geometry choice, the position vector may be re-written as

$$\mathbf{r}_{m,n} = m \cdot d_x \hat{\mathbf{x}} + n \cdot d_y \hat{\mathbf{y}} \tag{A.11}$$

The array factor expression is then written through a double index summation

$$AF(\phi, \theta) = \sum_{n=0}^{N-1} \sum_{m=0}^{M-1} I_{m,n} e^{jk(md_x sin(\theta)cos(\phi) + nd_y sin(\theta)sin(\phi))} \tag{A.12}$$

Each index maps one of the planar dimensions, θ is the elevation angle,ϕ is the azimuth component and $I_{m,n}$ is the excitation amplitude of the single element. The adopted RIS model uses *perfect reflectors assumption* so that for all cells $I_{m,n}$=1. Given the received field coming from the transmitter located at point $[r_{tx}, \phi_{tx}, \theta_{tx}]$with respect to the RIS origin, which is also equal to the reference frame origin, the equivalent array factor may be expressed as

$$\mathrm{AF}(\phi_{tx}, \theta_{tx}) = \sum_{n=0}^{N-1} \sum_{m=0}^{M-1} e^{\Delta\tilde{\theta}_{m,n}} = \sum_{n=0}^{N-1} \sum_{m=0}^{M-1} e^{jk(md_x sin(\theta)cos(\phi) + nd_y sin(\theta)sin(\phi))} \tag{A.13}$$

Appendix A (continued)

At the same time, given a destination point P=$[r_P, \phi_P, \theta_P]$, the transmitted field pattern from the RIS is described as

$$\mathbf{f}_r(\phi_P, \theta_P) = \mathbf{f}_0(\phi_P, \theta_P) \cdot \mathrm{AF}(\phi_P, \theta_P) \tag{A.14}$$

where $\mathbf{f}_0(\phi_P, \theta_P) = \frac{I_0}{4\pi r}\hat{r}$ is the single-cell pattern. The total pattern is given according to the well-known **pattern multiplication rule** valid for arrays of identical radiators. Assuming decoupled elements, i.e., elements embedded into an array behave as if each of them was isolated, the pattern multiplication applies to generic excitation magnitudes, the progressive phase shift between the elements, and displacement. The AF, in general, depends on the number of elements, the mutual placement, and relative excitation magnitudes and phases. It should be noted that the RIS is not comprised of Q independent radiators with a specific electric field profile. Each element can only modulate the phase of the field, resembling a phase array structure. The phase component forming the AF is given by

$$\Delta\tilde{\theta} = -(md_x \cdot sin(\theta_P)cos(\phi_P) + nd_y \cdot sin(\theta_P)sin(\phi_P)) \tag{A.15}$$

The overall phase correction for the electrical field reflected by the RIS is going to be

$$\Delta\tilde{\theta} = \Delta\tilde{\theta}_{tx} - \Delta_{\theta_P} \tag{A.16}$$

Appendix A (continued)

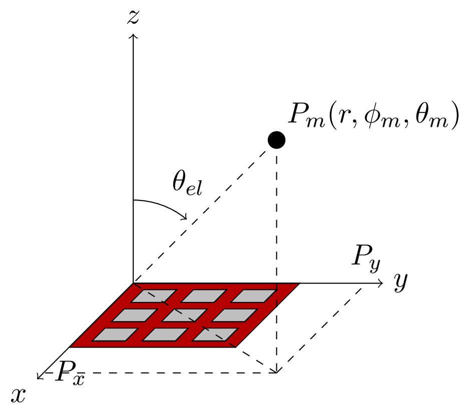

Figure 41: RIS 3D model with point P and dashed lines for azimuth and elevation angles:m_{th} point side

Each RIS q_{th} cell has then to compensate for the phase difference in order to align the fields of reflected and forward paths and let them sum coherently when impinging on the target.

A.3 SAR fundamentals

Low-cost and low-complexity RF imaging systems require techniques to enhance effective aperture and resolution. These systems typically use basic antennas with small apertures. Instead of relying on a physical array (Real Aperture Array), RF imaging using Synthetic Aperture Radar (SAR) improves resolution while maintaining low hardware complexity. The array is synthesized by moving the antenna along the azimuth direction to attain large antenna aperture without the size and weight burdens associated with physically large antennas. The strip-map approach, for example, is used to image a wider strip in the space[46] and is more likely the closest mode to RIS-aided imaging.

Appendix A (continued)

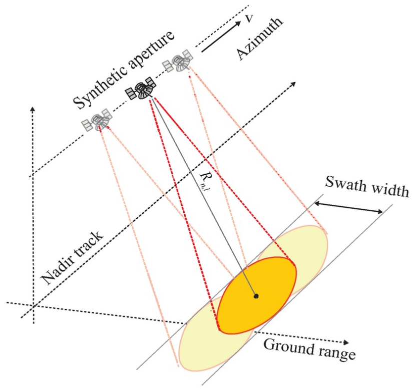

Figure 42: SAR imaging- Stripmap configuration

The variety in the multiple measurements is achieved by moving the single antenna along either the azimuth or angular direction. As well known, the spatial resolution is worsened by the low frequency, causing the transmitted beam to widen, reducing the effective aperture. In a smarter way, the super-resolution achieved by SAR array '*distributed*' over the time along the nadir track as shown in Figure 42, outperforms the original strongly limited RAR(Real Aperture Radar). A technique seamlessly integrated into already existing smart electromagnetic environment (SEME) might compensate for hardware complexity using man-made Reflective Intelligent Surface(RIS) acting as wide aperture antennas.

RIS can be modeled according to Planar Uniform Rectangular Arrays theory, where the inter-element coupling among adjacent cells can be neglected as long as the cell spacing complies with the Nyquist theorem for the spatial frequency limit. The frequency components are related to the wave number of the propagating EM field, varying according to the sub-carrier frequency.

Appendix A (continued)

This is an interesting analogy that has been proven effective with the proper shifts. The antennas are no longer synthesized, but they consist of a physical array of reflectors. The parallelism could lead to a more physical characterization of the imaging properties.

Appendix B

B.1 Algebraic Reconstruction Technique

The ART method falls under the category of series expansion methods. The unknown function to be reconstructed from the 1D projection measurements is assumed to be expressed as a linear combination of basis functions [37]:

$$f(x', y') \approx \sum_{j=1}^{N} b_j(x', y')a_j \tag{B.1}$$

where a_j represents the albedo profile and b_j denotes the local basis functions. This work has utilized 2D gates as basis functions for simplicity. However, in Computed Tomography (CT), the effectiveness and smoothness of various basis expansion functions have been demonstrated [47].

Typically, the relationship between the projections (measurements) and the unknowns (pixels of the object) is linear. Each m_{th} measurement can be expressed as

$$p_m = \sum_{j=1}^{N} l_{m,j}a_j \tag{B.2}$$

Appendix B (continued)

where $l_{m,j}$ is the m_{th} measurement of the j_{th} basis function. The implicit assumption is that the estimated pixel a_j, regardless of being "right", weights a specific local uniform function. The problem then reduces to estimating each x_j from the set of measurements to reconstruct the albedo according to Equation B.1. This method is particularly suitable for systems that tend to be sparse. The method processes one measurement at a time, updating only those elements intersected by the line integral of the ray through the profile. The main advantages of the method are its relatively low complexity and high flexibility. Convergence and reconstruction quality depend on estimation criteria, stopping rules, and a-priori information. One main problem that make this method criptic is the relaxation parameter choice. Given the wide set of the applications and the variety of the approaches, the only way to choose the parameter is experimental.

B.2 Sparse Majorization Minimization Algorithm

The rigorous derivation of the iterative solution is not part of the purposes of this work, and it is strongly advised to refer to a more focused discussion about the specific topic[30; 40]. We report in the following only the main passages through the final iterative solution after MM application. Starting from a *Lasso regularization*

$$J(\mathbf{y}) = \|H\mathbf{y} - \mathbf{P}\|_1 + \mu\|\mathbf{y}\|_1 \tag{B.3}$$

Appendix B (continued)

the objective containing the L_1 norm is turned into a quadratic problem according to a monotonically decreasing sequence of majorizer[40]

$$J(\mathbf{y}^k) = \frac{1}{2}\|H\mathbf{y} - \mathbf{P}\|_2^2 + \xi(\mathbf{y}) \tag{B.4}$$

Since we look for a majorizer in a polynomial shape, we can re-write

$$\xi(\mathbf{y}) = \frac{1}{2}\mathbf{y}^T\Lambda_k^{-1}\mathbf{y} + \frac{1}{\|\mathbf{y}_k\|_1} > \|\mathbf{y}\|_1 \tag{B.5}$$

where $\Lambda_k := \mathrm{diag}(|\mathbf{y}_k|)$. The majorizer of $\|\mathbf{y}\|_1$ takes the shape of a quadratic function of $\mathbf{y}$. Let's notice that both the last term $\|\mathbf{y}_k\|_1$ and Λ_k in is also not a function of $\mathbf{y}$ and can be considered constant as $\mathbf{y}_k$ is known from previous iteration. Now, the function to be reduced can be simplified removing the fixed and constant last term of the majorizer. A majorizer of the Lasso regularized cost function in (Equation B.3) can be obtained by adding $\frac{1}{2}\|\mathbf{P} - H\mathbf{y}\|_2^2$ to both sides:

$$\frac{1}{2}\|\mathbf{P} - H\mathbf{y}\|_2^2 + \lambda_1\mathbf{y}^T\Lambda^{-1}\mathbf{y} > \frac{1}{2}\|\mathbf{P} - H\mathbf{y}\|_2^2 + \lambda\|\mathbf{y}\|_1 \tag{B.6}$$

CITED LITERATURE

1. Tortoriello, C., Erricolo, D., and Oliveri, G.: Wave Manipulating RIS for Enhanced Tomographic Imaging: Concept and Recent Advances. In 2024 United States National Committee of URSI National Radio Science Meeting (USNC-URSI NRSM), pages 236–237, 2024.

2. Kak, A. C. and Slaney, M.: Principles of Computerized Tomographic Imaging. Society for Industrial and Applied Mathematics, 2001.

3. Devaney, A.: Geophysical diffraction tomography. Geoscience and Remote Sensing, IEEE Transactions on, pages 3–13, 1984.

4. Akiyama, I.: Acoustical Imaging. Springer London, Limited, 2009.

5. Viswanathan, N., Venkatesh, S., and Schurig, D.: Optimization of a sparse aperture configuration for millimeter-wave computational imaging. IEEE Trans. Antennas Propag., 69(2):1107–1117, February 2021.

6. Wang, J., Xiong, J., Chen, X., Jiang, H., Balan, R. K., and Fang, D.: Simultaneous target imaging and material identification with commodity RFID devices. In Proc. 23rd Annu. Int. Conf. Mobile Comput. Netw., pages 288–300, 2017.

7. Guo, Q., Wang, Z., Chang, T., and Cui, H.-L.: Millimeter-wave 3-D imaging testbed with MIMO array. IEEE Trans. Microw. Theory Techn., 68(3):1164–1174, March 2020.

8. He, Y., Zhang, D., and Chen, Y.: High-Resolution WiFi Imaging With Reconfigurable Intelligent Surfaces. IEEE Internet of Things Journal, 10(2):1775–1786, 2023.

9. Wu, Q. and Zhang, R.: Towards smart and reconfigurable environment: Intelligent reflecting surface aided wireless network. IEEE Communications Magazine, 58(1):106–112, 2020.

10. Wu, Q. and Zhang, R.: Beamforming optimization for wireless network aided by intelligent reflecting surface with discrete phase shifts. IEEE Transactions on Communications, 68(3):1838–1851, Mar. 2020.

CITED LITERATURE (continued)

11. You, L., Xiong, J., Ng, D. W. K., Yuen, C., Wang, W., and Gao, X.: Energy Efficiency and Spectral Efficiency Tradeoff in RIS-Aided Multiuser MIMO Uplink Transmission. IEEE Transactions on Signal Processing, 69:1407–1421, 2021.

12. Mahafza, B. R.: Radar Systems Analysis and Design Using MATLAB. Chapman and Hall/CRC, 3th ed. edition, 2013.

13. A., M.: Wave Propagation and Scattering in Random Media. New York, Academic Press, 1978.

14. Slaney, M., Kak, A. C., and Larsen, L. E.: Limitations of imaging with first-order diffraction tomography. IEEE Transactions on Microwave Theory and Techniques, 32:860–874, 1984.

15. Gao, G., Li, H.-C., Cloude, S. R., Yang, J., and Nunziata, F.: Foreword to the Special Issue on Compact Polarimetric SAR. IEEE Journal of Selected Topics in Applied Earth Observations and Remote Sensing, 12(10):3708–3711, 2019.

16. Dubois-Fernandez, P. C., Souyris, J.-C., Angelliaume, S., and Garestier, F.: The Compact Polarimetry Alternative for Spaceborne SAR at Low Frequency. IEEE Transactions on Geoscience and Remote Sensing, 46(10):3208–3222, 2008.

17. Torrealba-Meléndez, R., Olvera-Cervantes, J. L., and Corona-Chávez, A.: Resolution improvement of an UWB microwave imaging radar system using circular polarization. In 2014 International Conference on Electronics, Communications and Computers (CONIELECOMP), pages 189–193, 2014.

18. Erricolo, D.: Distributed RF Systems for Close-In Sensing and Imaging. Technical Report, Final Report, University of Illinois at Chicago, 2016. Accession Number: AD1006928, Pagination: 181.

19. Sayed, A. H.: Least-Squares Criterion, chapter 29, pages 475–491. John Wiley & Sons, Ltd, 2008.

20. Boyd, S. and Vandenberghe, L.: Convex optimization, chapter 11. Cambridge University Press, 2004.

21. Vachon, P. W.: Digital Processing of Synthetic Aperture Radar Data: Algorithms and Implementation. Geomatica, 59(3):353+, 2005. Accessed April 23, 2024.

CITED LITERATURE (continued)

22. Reichel, L.: Numerical methods for linear discrete ill-posed problems, 2018.

23. Hansen, P. C.: Truncated singular value decomposition solutions to discrete ill-posed problems with ill-determined numerical rank. SIAM Journal on Scientific and Statistical Computing, 11(3):503–518, 1990.

24. Golub, G. H. and O'Leary, P. C. H. D. P.: Tikhonov regularization and total least squares. SIAM Journal on Matrix Analysis and Applications, 21(1):185–194, 1999.

25. Hansen, T. B. and Yaghjian, A. D.: Low-frequency scattering from two-dimensional perfect conductors. IEEE Trans. Antennas Propag., 40(11):1389–1402, Nov. 1992.

26. Fenu, C., Reichel, L., and Rodriguez, G.: GCV for Tikhonov regularization via global Golub–Kahan decomposition. Numer. Linear Algebra Appl., 23:467–484, 2016.

27. Picco, V.: Dyadic Contrast Function And Quadratic Forward Model For Radio Frequency Tomography. Doctoral dissertation, University of Illinois at Chicago, Chicago, IL, May 2014.

28. Andersen, A. H. and Kak, A. C.: Simultaneous Algebraic Reconstruction Technique (SART): A Superior Implementation of the ART Algorithm. Ultrasonic Imaging, 6(1):81–94, 1984.

29. Piccolomini, E. L. and Zama, F.: The conjugate gradient regularization method in computed tomography problems. Applied Mathematics and Computation, 102(1):87–99, 1999.

30. Piccolomini, E., Coli, V., Morotti, E., and Zanni, L.: Reconstruction of 3D X-ray ct images from reduced sampling by a scaled gradient projection algorithm. Computational Optimization and Applications, 71, 09 2018.

31. Chinn, G. and Huang, S.-C.: A general class of preconditioners for statistical iterative reconstruction of emission computed tomography. IEEE Transactions on Medical Imaging, 16(1):1–10, 1997.

32. Gordon, R., Bender, R., and Herman, G. T.: Algebraic reconstruction techniques (ART) for three-dimensional electron microscopy and X-ray photography. Journal of Theoretical Biology, 29(3):471–481, 1970.

33. Gordon, R.: A tutorial on ART (Algebraic Reconstruction Techniques). Nuclear Science, IEEE Transactions on, 21:78–93, 06 1974.

34. Picco, V., Negishi, T., Nishikata, S., Spitzer, D., and Erricolo, D.: RF Tomography in Free Space: Experimental Validation of the Forward Model and an Inversion Algorithm Based on the Algebraic Reconstruction Technique. International Journal of Antennas and Propagation, 2013(1):528347, 2013.

35. Herman, G. T. and Meyer, L. B.: Algebraic reconstruction techniques can be made computationally efficient (positron emission tomography application). IEEE transactions on medical imaging, 12(3):600–609, 1993.

36. Hounsfield, G.: A Method and Apparatus for the Examination of the Body by Radiation Such as X or Gamma Radiation. Patent Specifications 1283915, The Patent Office, London, 1972.

37. Herman, G.: Image reconstruction from projections. Real-Time Imaging, 1(1):3–18, 1995.

38. Kaufman, L.: Implementing and accelerating the EM algorithm for positron emission tomography. IEEE Transactions on Medical Imaging, 6:37–51, 1987.

39. Lin, Z., Chen, M., and Ma, Y.: The augmented Lagrange multiplier method for exact recovery of corrupted low-rank matrices. arXiv preprint arXiv:1009.5055, Sep 2010.

40. Selesnick, I.: Total variation denoising (an MM algorithm). NYU Polytechnic School of Engineering Lecture Notes, 2012.

41. Zhang, Q., Zhang, Y., Huang, Y., Zhang, Y., Li, W., and Yang, J.: Sparse with fast mm superresolution algorithm for radar forward-looking imaging. IEEE Access, 7:105247–105257, 2019.

42. Wang, Z., Bovik, A., Sheikh, H., and Simoncelli, E.: Image quality assessment: from error visibility to structural similarity. IEEE Transactions on Image Processing, 13(4):600–612, 2004.

43. Kenue, S. and Greenleaf, J.: Limited angle multifrequency diffraction tomography. IEEE Transactions on Sonics and Ultrasonics, 29(4):213–216, 1982.

44. Wang, J., Xiong, J., Chen, X., Jiang, H., Balan, R. K., and Fang, D.: Tagscan: Simultaneous target imaging and material identification with commodity rfid devices.

In Proceedings of the 23rd Annual International Conference on Mobile Computing and Networking, pages 288–300, 2017.

45. Hum, S. V.: Antenna arrays.

46. Watts, C. M., Lancaster, P., Pedross-Engel, A., Smith, J. R., and Reynolds, M. S.: 2D and 3D millimeter-wave synthetic aperture radar imaging on a PR2 platform. In 2016 IEEE/RSJ International Conference on Intelligent Robots and Systems (IROS), pages 4304–4310, 2016.

47. Lewitt, R. M.: Alternatives to voxels for image representation in iterative reconstruction algorithms. Physics in Medicine & Biology, 37(3):705, mar 1992.

VITA

NAME	Carlo Tortoriello
EDUCATION	
	Master of Science in “Electrical and Computer Engineering”, University of Illinois Chicago, Nov 2024, USA
	Laurea Magistrale (MS degree) in “Electronics for industrial applications”, Expected Dec 2024, Polytechnic of Turin, Italy
	Bachelor of Science in “Electronic Engineering”, Jul 2022, Polytechnic of Turin, Italy
	Classic Lyceum Diploma, Jul 2019, Liceo Classico E.Perito, Eboli, Italy
LANGUAGE SKILLS	
Italian	Native speaker
English	Full working proficiency
	A.Y. 2023/24 One Year of study abroad in Chicago, Illinois
	A.Y. 2022/23. Lessons and exams attended exclusively in English
	2022 - IELTS examination (7.5/9)
	2013 - English Summer School at ”National University of Ireland, Maynooth”
	2012 - English Summer School at ISIS Heriot Watt
Spanish	2015 - DELE A2, Istituto Cervantes
SCHOLARSHIPS	
Spring 2024	UIC *tuition fee waiver* scholarship for TOP-UIC project, ECE group
Spring 2023	Italian scholarship for TOP-UIC students
TECHNICAL SKILLS	
Basic level	DSP, LabVIEW, OSA, Wavelength meter, Oscilloscope,VNA, Spectrum Analyzer, Electronic measurement systems, Arduino
Average level	OOP [C++, Python],Optical and RF characterization

VITA (continued)

Advanced level	AWR guided systems, CST studio for radiation problems, Numerical technique, Electromagnetics, Least squares algorithms

WORK EXPERIENCE AND PROJECTS

May 2024 - Aug 2024	Summer '24 Internship @ **NVIDIA** as Software Engineer: analysis and evaluation effect of mutual coupling in MIMO systems of wire antennas
Jan 2024	Student Speaker @ **National Radio Science Meeting 2024**, Boulder, CO: Wave Manipulating RIS for Enhanced Tomographic Imaging: Concept and Recent Advances
2022-2023	Other Experiences:
	High-frequency microstrip Low-Pass filter design in AWR tool: @f_{cut} =2.4 GHz, roll-off ρ=27 dB @f=3.5 GHz. The fabricated device has been validated using VNA measures.
	Laser @ 1550 nm and 980 nm characterization: temperature versus current curve, emitting mode wavelength versus current curve, current effect on Phase noise
	Passive optical devices characterization: 2-ports(isolator), 3-ports(circulator, Add&Drop).
	Optical bandwidth measurement: self-homodyne and heterodyne techniques using Optical Spectrum Analyzer(OSA).
	Active optical devices characterization(Erbium-Doped Fiber Amplifiers: counter-propagating and co-propagating configurations.
2021	University Calendar scheduler based on OOP: exams(room, time, midterm number) were scheduled according to major

PUBLICATIONS

Jan 2024	C. Tortoriello, D. Erricolo and G. Oliveri, "Wave Manipulating RIS for Enhanced Tomographic Imaging: Concept and Recent Advances," 2024 United States National Committee of URSI National Radio Science Meeting (USNC-URSI NRSM), Boulder, CO, USA, 2024, pp. 236-237.
Jul 2024	Sparse Majorization-Minimization for Opportunistic RIS-Aided WiFi Imaging": Transactions on Internet of Things (submitted)